

**3D SEISMIC INTERPRETATION, PETROPHYSICS AND
MACHINE LEARNING-BASED QUANTITATIVE
INTERPRETATION OF GAMBAT LATIF BLOCK LOWER
INDUS BASIN, PAKISTAN**



SAMAN FATIMA

01-262212-017

Department of Earth and Environmental Sciences

Bahria University, Islamabad

2023

**3D SEISMIC INTERPRETATION, PETROPHYSICS AND
MACHINE LEARNING-BASED QUANTITATIVE
INTERPRETATION OF GAMBAT LATIF BLOCK LOWER
INDUS BASIN, PAKISTAN**



SAMAN FATIMA

01-262212-017

A thesis submitted to Bahria University, Islamabad in partial fulfillment of the requirement
for the degree of Master of Science in Geophysics

Department of Earth and Environmental Sciences

Bahria University, Islamabad

2023

APPROVAL FOR EXAMINATION**Scholar's Name:** SAMAN FATIMA**Registration No.** 42720**Program of Study:** MS GEOPHYSICS**Thesis Title:** 3D Seismic Interpretation, Petrophysics and Machine Learning-based quantitative interpretation of Gambat Latif Block Lower Indus Basin, Pakistan.

It is to certify that the above scholar's thesis has been completed to my satisfaction and, to my belief, its standard is appropriate for submission for examination. I have also conducted a plagiarism test of this thesis using HEC prescribed software and found similarity index **11%** that is within the permissible limit set by the HEC for the MS degree thesis. I have also found the thesis in a format recognized by the BU for the MS thesis.

Principal Supervisor's Signature: _____**Date:** _____ 24-September-2023 _____**Name:** _____

AUTHOR'S DECLARATION

I, "**Saman Fatima**" hereby state that my MS thesis titled "**3D Seismic Interpretation, Petrophysics and Machine Learning-based quantitative interpretation of Gambat Latif Block Lower Indus Basin, Pakistan** " is my own work and has not been submitted previously by me for taking any degree from this university **Bahria University Islamabad** or anywhere else in the country/world. At any time if my statement is found to be incorrect even after my graduation, the University has the right to withdraw/cancel my MS degree.

Name of scholar: Saman Fatima


Date: 24-September-2023

PLAGIARISM UNDERTAKING

I solemnly declare that research work presented in the thesis titled “titled “**3D Seismic Interpretation, Petrophysics and Machine Learning-based quantitative interpretation of Gambat Latif Block Lower Indus Basin**” is solely my research work with no significant contribution from any other person. Small contribution / help wherever taken has been duly acknowledged and that complete thesis has been written by me.

I understand the zero-tolerance policy of the HEC and Bahria University towards plagiarism. Therefore, I as an Author of the above titled thesis declare that no portion of my thesis has been plagiarized and any material used as reference is properly referred to / cited.

I undertake that if I am found guilty of any formal plagiarism in the above titled thesis even after award of MS degree, the university reserves the right to withdraw / revoke my MS degree and that HEC and the University has the right to publish my name on the HEC / University website on which names of scholars are placed who submitted plagiarized thesis.

Scholar / Author's Sign: _____  _____

Name of the Scholar: Saman Fatima

DEDICATION

I dedicate my thesis to my parents for their endless affection, support, and encouragement throughout my pursuit of education. I truly hope this accomplishment will fulfill the dream they envisioned for me.

ACKNOWLEDGEMENTS

All praise and reverence are rightfully directed towards Allah, the Almighty (S.W.T.), and it holds the utmost importance for me to humbly submit before His divine presence. He is the sole bestower of all wisdom and knowledge. I want to convey my deep gratitude to Allah SWT, the Supreme Creator, for His blessings, benevolence, and the inspiration that guided me to successfully complete this thesis. It is through His grace only that I found the patience and determination to write this thesis, from its inception to its conclusion. My heartfelt blessings and salutations extend to the Holy Prophet Muhammad (S.A.W.W), the last prophet, and the one who illuminated our path from ignorance to enlightenment.

I would like to extend my heartfelt gratitude to my supervisor Dr Muhsan Ehsan my Co-supervisor and Dr Khalid Amin Khan for their invaluable guidance, unwavering support, and profound wisdom throughout the course of my thesis. Their dedication to my academic growth and their commitment to fostering my research skills have been instrumental in shaping this work. I am truly fortunate to have had Dr Mushan Ehsan and Dr Khalid Amin Khan as my mentors, and their expertise has left an indelible mark on my educational journey. Their encouragement, constructive feedback, and mentorship have been pivotal in the successful completion of this thesis.

In addition to this, I would like to express my profound gratitude to Dr. Said Akbar Khan, the Head of the Department of Earth and Environmental Sciences at Bahria University, Islamabad, for his exceptional support and guidance. I extend my heartfelt thanks to my teachers and fellow geophysicists for their virtuous and influential encouragement, assistance, and collaboration throughout the course of my research work.

I also want to express my gratitude to my parents for their continuous encouragement and belief in me. I am also quite thankful to all my friends that kept motivating me throughout my thesis.

ABSTRACT

The study's primary goal is to identify the thin sands packages of B and C Intervals of Lower Goru Formation of Gambat Latif block, by using machine learning along with reservoir characterization by performing seismic interpretation, seismic inversion, petrophysics and seismic attributes. The Gambat-Latif region is situated within the Lower Indus Basin of Pakistan, and its geological setting is characterized by extensional tectonic processes. Following the completion of seismic interpretation, seismic inversion, and petrophysical analysis, the findings indicate that the C Interval of the Lower Goru Formation within the Gambat Latif block exhibits a more substantial hydrocarbon potential when contrasted with the B-Interval. Seismic attributes were employed to detect the presence of slender sand units, and it was noted that the Spectral Decomposition attribute produced the most reliable results. This attribute effectively delineated specific zones within both the B and C sands, and the thinner sand beds within the Lower Goru B and C intervals. The thin sand beds within the Lower Goru B and C intervals in the Tajjal 02 well became more prominently evident as the frequency spectrum of the spectral decomposition attribute was increased. Moreover, machine learning methodologies were utilized to calculate and validate the shear sonic values, both computed from the Castagna equation and those computed using machine learning techniques. It was noted that the Machine Learning-based computation of Vs demonstrated greater reliability and yielded better results when contrasted with the Castagna equation method. Machine Learning was also employed for facies analysis, resulting in the categorization of facies into three distinct lithological packages: sand, shale, and tight sand. The last encompassed the utilization of machine learning techniques for geomechanical analysis, during which several geomechanical parameters, such as overburden pressure, pore pressure, and fracture gradient, were computed.

TABLE OF CONTENTS

CHAPTER	TITLE	PAGE
	APPROVAL OF EXAMINATION	iii
	AUTHOR'S DECLARATION	iv
	PLAGIARISM UNDERTAKING	v
	DEDICATION	vi
	ACKNOWLEDGMENTS	vii
	ABSTRACT	viii
	TABLE OF CONTENT	ix
	LIST OF TABLES	xiv
	LIST OF FIGURES	xv
	LIST OF ABBREVIATIONS	xvi
1	INTRODUCTION	1
	1.1 Overview	1
	1.2 Introduction to Study Area	3
	1.3 Exploration History	4
	1.4 Objectives	5
	1.5 Available Data	7
	1.6 Software Used	7
	1.7 Literature review	8
	1.8 Purpose of research	9
	1.9 Methodology of Research	10

2	REGIONAL GEOLOGY AND STRATIGRAPHY	11
2.1	Introduction	12
2.2	Basins of Pakistan	13
2.2.1	Upper Indus basin	14
2.2.2	Lower Indus basin	15
2.3	Regional Tectonic Setting	16
2.4	Structural Setting of Gambat-Latif Area	17
2.5	Stratigraphy of the Study area	19
2.6	Petroleum Play of the Study Area	19
2.6.1	Source Rock	20
2.6.2	Reservoirs Rock	20
2.6.3	Seal Rock	20
2.6.4	Trapping Mechanism	20
3	3D SEISMIC INTERPRETATION	21
3.1	Seismic Interpretation's Workflow	22
3.1.1	Loading of Seismic Data	23
3.1.2	Base Map	24
3.1.3	Synthetic Seismogram	25
3.1.4	Horizon and fault marking	27
3.1.5	Preparation of Contour Maps	29
3.1.6	Interpretation of C-interval maps	32
3.1.7	Interpretation of B-interval maps	34
4	PETROPHYSICAL ANALYSIS	35
4.1	Introduction	35
4.2	LAS files loading	36
4.3	Marking Zone of Interest	37

4.4	Calculation of Petrophysical Parameters	38
4.4.1	Calculation of volume of shale	39
4.4.2	Calculation of Volume of clean	39
4.4.3	Calculation of Density Porosity	40
4.4.4	Calculation of Average Neutron Density Porosity	40
4.4.5	Calculation of Effective Porosity	40
4.4.6	Resistivity of Water Calculation	41
4.4.7	Calculation of Archie Water Saturation (Sw)	41
4.4.8	Calculation of Hydrocarbon Saturation (Sh)	41
4.5	Petrophysical Interpretation of B Interval Tajjal 01	42
4.5.1	Petrophysical Interpretation of B Interval Tajjal 01	42
4.5.2	Petrophysical Interpretation of B Interval Tajjal 02	43
4.6	Petrophysical Interpretation of C Interval Tajjal 01	45
4.6.1	Petrophysical Interpretation of B Interval Tajjal 01	46
4.6.2	Petrophysical Interpretation of B Interval Tajjal 01	46
4.7	Results of Petrophysical Interpretation	47
5	SEISMIC INVERSION AND ATTRIBUTES	48
5.1	Introduction	48
5.1.1	Seismic inversion's purpose	49
5.2	Post Stack Inversion	50
5.3	Model Based Inversion	50
5.4	Methodology adopted for Model Based Inversion	51
5.4.1	Seismic and Well Data Loading	51
5.4.2	Loading of Horizons	52
5.4.3	Extraction of Statistical Wavelet	54
5.4.4	Seismic to Well Correlation	55

5.4.5	Initial Low-frequency Model	57
5.4.6	Inversion Analysis	59
5.4.7	Results of Model-Based Inversion	60
5.4.8	Slices	61
5.5	Seismic Attributes	62
5.5.1	Classification of Attributes	63
5.6	Attribute analysis of the study area	64
5.6.1	Spectral Decomposition	65
5.6.2	Instantaneous Phase	69
5.6.3	Trace envelope	70
6	COMPUTATION AND VALIDATION OF SHEER SONIC USING MACHINE LEARNING AND FACIES ANALYSIS	71
6.1	Introduction	72
6.2	Data Review	72
6.3	Rock Physics Computation	73
6.4	Calculation of shale volume	74
6.5	Porosity Computation	75
6.6	Multi regression	76
6.7	Comparison of Vs computed from Castagna, and Vs computed by Machine Learning	77
6.8	AVO Modeling	79
6.8.1	AVO modeling using shear sonic computed by Castagna Equation	81
6.8.2	AVO modeling using shear sonic computed by Machine Learning	82
6.8.3	Validation of shear sonic computed from multi regression	84
6.9	Facies Analysis	85
6.9.1	Cross plots between Vp and Vs	86

6.9.2	Cross plots between Vp and Density	86
6.9.3	Cross plots between Vs and Density	87
7	Machine Learning Based Geomechanics	88
7.1	Introduction	88
7.2	Description of first workflow	90
7.3	Description of second workflow	94
7.4	Description of third workflow	97
7.5	Results and Discussions	98
	CONCLUSIONS	102
	REFERENCES	104
	ANNEXURE A	116

LIST OF TABLES

TABLE NO.	TITLE	PAGE
1.1	Data provided by LMKR	5
4.1	Result of Petrophysical Analysis of reservoir zones.	42
4.2	Multi regression Equations	72

LIST OF FIGURES

FIGURE NO.	TITLE	PAGE
1.1	Satellite imagery of Study Area	4
1.2	Gambat Latif Cube	5
1.3	Workflow for methodology adopted during research	8
2.1	Study Area Location Map	10
2.2	Stratigraphy of Lower Indus basin	14
2.3	Nomenclature of Lower Goru by OMV and ENI.	15
3.1	Workflow adopted for seismic interpretation during research	18
3.2	Figure 3.2 Base map of the study area showing the distribution of inlines and crossline along with type of well.	20
3.3	Synthetic Seismogram of Tajjal-02	22
3.4	Synthetic Seismogram of Tajjal-01	
3.5	Seismic section of Inline 1419 with well location of Tajjal- 2 along with the C and B Intervals with fault F1	23
3.6	Seismic section of Inline 1393 with the C and B Intervals with faults F1 and F2.	24
3.7	Seismic section of Inline 1311 showing displacement of fault F1	24
3.8	Two-way travel time contour map of C-Interval	26
3.9	Depth contour map of C-Interval.	27

3.10	Time contour map of B-Interval.	28
3.11	Depth contour map of B-Interval.	29
4.1	Resistivity of water for Tajjal 01 by Pickett plot method.	36
4.2	Resistivity of water for Tajjal 02 by Pickett plot method	36
4.3	Petrophysical analysis of Tajjal-1 on B-Interval of Lower Goru Formation	38
4.4	Petrophysical analysis of Tajjal-2 on B-Interval of Lower Goru Formation.	39
4.5	Petrophysical analysis of Tajjal-1 C-Interval of Lower Goru Formation	40
4.6	Petrophysical analysis of Tajjal-2 C-Interval of Lower Goru Formation	41
5.1	Generalized workflow of seismic inversion	44
5.2	Statistical wavelet for inversion analysis of Tajjal-02	48
5.3	Correlation of seismic data with Tajjal-02 well	49
5.4	Low Frequency model with well location of Tajjal-02	50
5.5	Model based inversion analysis of Tajjal- 02.	51
5.6	Final Computed impedance model at Tajjal-02 Well location.	53
5.7	3D cube slice for C Interval showing variation for Impedance.	54
5.8	3D cube slice for B Interval showing variation for Impedance.	54
5.9	Amplitude and frequency spectra for seismic inline 1419	58
5.10	Spectral Decomposition attribute of seismic line 1419 at 9 Hz frequency	59
5.11	Spectral Decomposition attribute of seismic line 1419 at 14 Hz frequency	60

5.12	Spectral Decomposition attribute of seismic line 1419 at 21 Hz frequency	60
5.13	Spectral Decomposition attribute of seismic line 1419 at 29 Hz frequency	61
5.14	Circles highlighting fault that was difficult to interpret on normal seismic section.	61
5.15	Instantaneous phase attribute calculated for seismic line 1419.	62
5.16	Instantaneous Amplitude (Trace envelope) applied on seismic line 1419.	63
6.1	Workflow adopted for computation of shear sonic computed by Machine Learning and it's validation by mapping AVO anomaly	67
6.2	Initial Input Data set for C and B interval ranging from 3300-3800 m in Tajjal-03	68
6.3	Rock Physics Properties computed including various moduli for C and B interval ranging from 3310-3800 m in Tajjal-03	69
6.4	Multi Regression-ML applied on depth intervals ranging from 3310-3800 m for C and B intervals of Tajjal-03	71
6.5	Comparison of Vs (Vs provided), Vs' (Vs-Castagna), Vs-ML (Vs computed by ML) for C and B interval of Tajjal-03	73
6.6	AVO modeling using shear sonic computed by Castagna Equation for C and B intervals of Tajjal-03	75
6.7	AVO modeling using shear sonic computed by ML for C and B intervals of Tajjal-03	76
6.8	Cross plots between Vp and Vs of C and B intervals in depth interval ranging from 3310 to 3800 m of Tajjal-03	78

6.9	Cross plots between Vp and Density of C and B intervals in depth interval ranging from 3310 to 3800 m of Tajjal-03	79
6.10	Cross plots between Vs and Density of C and B intervals in depth intervals ranging from 3310 to 3800 m of Tajjal-03	80
7.1	First Workflow adopted for delineation of layer boundaries in Tajjal-03	83
7.2	Output generated by adapting the first workflow for delineation of layer boundaries in Tajjal-03	84
7.3	Second Workflow for calculating the block averages for shale volume in Tajjal-03	87
7.4	Output generated by adapting the second workflow calculating the block averages for shale volume in Tajjal-03	88
7.5	Third Workflow for computation of geomechanical parameters for Tajjal-03	90
7.6	Output generated by adapting the third workflow for computation of geomechanical parameters for Tajjal-03	90

LIST OF ABBREVIATIONS

a	Lithological coefficient
AVO	Amplitude variation with offset
AVA	Amplitude variation with angle
BHTP	Bottom hole treatment pressure
CMP	Common Midpoint
CDP	Common Depth Point
CWT	Continuous Wavelet Transform
DHI	Direct hydrocarbon indicator
DTS	Shear Sonic log
DRV1	First derivative
DRV2	Second derivative
DRV1_Diff	Difference of first derivative
DRV1_DF1t	Filter applied on difference of first derivative
DRV1_MF1t	First derivative of minimum filter
$D\phi$	Density porosity

DT	Sonic log
DGPC	Directorate General of Petroleum Concessions
ENI	Ente Nazionale Idrocarburi
GRmax	Gamma ray maximum value
GRmin	Gamma ray minimum value
g/cm ³	Gram by center meter cube
GHPL	Government Holdings Private Limited
Hz	Hertz
HI	Hydrocarbon Development Institute of Pakistan
IR	Infra-Red
KFB	Kirthar Fold Belt
LLS	Laterolog shallow
LLD	Laterolog deep
MSFL	Micro-spherically focused log
ms	Meter second
ML	Machine learning
NPFI	Neutron log
NE	North-east
NW	North-west

Obpi	Overburden pressure
OGDCL	Oil and Gas Development Company Limited
OM	Organic Matter
Pma	Density of matrix
PPL	Pakistan Petroleum Limited
PEF	Photoelectric effect
PHIA	Average Porosity
PHIE	Effective Porosity
ρ_b	Bulk density of the formation
ρ_f	Fluid's density
Rw	Resistivity of water
RHOB	Bulk density
SPK_MFIt	Spiking filter applied on moving average
SDFTB	Southern Deformed Fold and Thrust Belt
TOC	Total Organic Carbon
Vs	Shear sonic velocity
XRD	X-ray diffraction

CHAPTER 1

INTROUDCITON

1.1 Overview

The study's primary goal is to identify the thin sands packages of Lower Goru Formation by using machine learning along with reservoir characterization by performing seismic interpretation, petrophysics, seismic attributes. To achieve this objective many methods are in use now a days. Out of these all, seismic inversion, attribute analysis and petrophysics are of much importance throughout the world.

Seismic interpretation's primary goal is to precisely characterize the lithology and subterranean geological formations. Rocks that contain hydrocarbons can be distinguished from rocks that do not by using seismic data analysis (Ahmad et al., 2021).

One of the widely used methods for characterization of the reservoir is seismic inversion. Seismic inversion aids in combining seismic and well data for predicting the characteristics of reservoir and these include information regarding fluid content of reservoir, type of lithology etc. throughout the seismic survey region. The identification of hydrocarbon sites and reservoirs can then be aided by these characteristics of rocks (Francis, 2014). Seismic inversion's main objective is to convert seismic reflection data into a quantifiable rock property that describes the reservoir i.e., Acoustic impedance logs are computed at each CMP (Pendrel, 2001).

A seismic attribute is such a quantity which is derived or extracted from seismic data. By mathematical manipulation of original seismic data one can compute the seismic attributes. The seismic attributes can help in highlighting special physical, geological or other reservoir property feature., which then leads to a better geophysical or geological interpretation of the data used (Chopra and Marfurt, 2005). There are number of seismic attributes which are used some of these include, frequency, bandpass attributes , phase, amplitude, time, etc. (Masinde, 2017).

By making use of seismic attributes interpreters are able to extract more information from original seismic data. If one uses seismic attributes for the purpose of stratigraphy analysis, seismic attributes can assist in understanding the environment of deposition. The presence of hydrocarbons in some cases gives rise to an anomalous attribute response which is then analyzed to see whether this anomalous amplitude is associated with the presence of oil or not (González et al., 2021).

Petrophysics is the study of the characteristics of rocks and how they relate to the fluids they contain in both their static and flowing conditions. The characteristics of the pore system's fluid distribution and flow are highlighted by petrophysics. In order to evaluate and identify hydrocarbon reservoirs these properties and their relationships are used (Glover, 1998).

The chemical and physical characteristics of oil and gas deposits, as well as the surrounding rocks and soil, are studied and analysed by petrophysicists. They gather and analyse information on these reservoirs, such as pore pressure, electrical and acoustic characteristics of the rock, rock density, and radioactivity levels (Glover, 1998).

The availability of shear sonic log(DT) is essential for lithology and fluid discrimination within the reservoirs. However, within the Lower Indus Basin there are only limited wells that have the availability of shear sonic log. This is where Machine Learning plays its part. With fewer input data sets, machine learning has lately become a reliable and optimized method for forecasting the exact shear sonic log(DTS)(Ahmed et al., 2022).

The study of mechanical behavior of geological materials is known as geomechanics. These studies, engineering components or applied geomechanics, describe how mining activities affect the geological environment (Ostad et al., 2018).

Understanding the stability and integrity of the borehole while drilling is largely dependent on geo mechanics. The wellbore's presence and drilling fluids' pressure cause change in the rocks or the stress condition. Young modulus, bulk modulus, shear modulus and poisson's ratio are examples of elastic and inelastic geomechanical properties (fracture gradient and formation strength) (Ostad et al., 2018).

1.2 Introduction to Study Area

Gambat Latif area is located in Khairpur district of Sindh province. In terms of geomorphology, the research region is situated between the southern desert and Chhistan desert(north) and geologically the Tajjal gas field (Gambat Block) is located in the lower Indus Basin. Nearly 3648.73 square kilometers make up the Gambat Block (Toqeer et al., 2021). The coordinates of the block are $68^{\circ} 31' E$ and at $27^{\circ} 21' N$. The 3D Gambat Latif concession is located in the northern region of the Sindh Province and is commonly referred to as the Nara Desert. The Nara Desert serves as an intermediate area, situated between the Cholistan Desert to the north and the Thar Desert to the south.

The Tajjal gas field is a producing field of the Gambat Block. Geographically, the Tajjal Gas Field is situated in Pakistan's Sindh Province, approximately 120 kilometres (km) south-east of Sukkur. Tajjal Gas Field (Gambat Block) is situated geologically in the Lower Indus Basin, which is a recognised Geological Province in Pakistan (Khan et al., 2014).

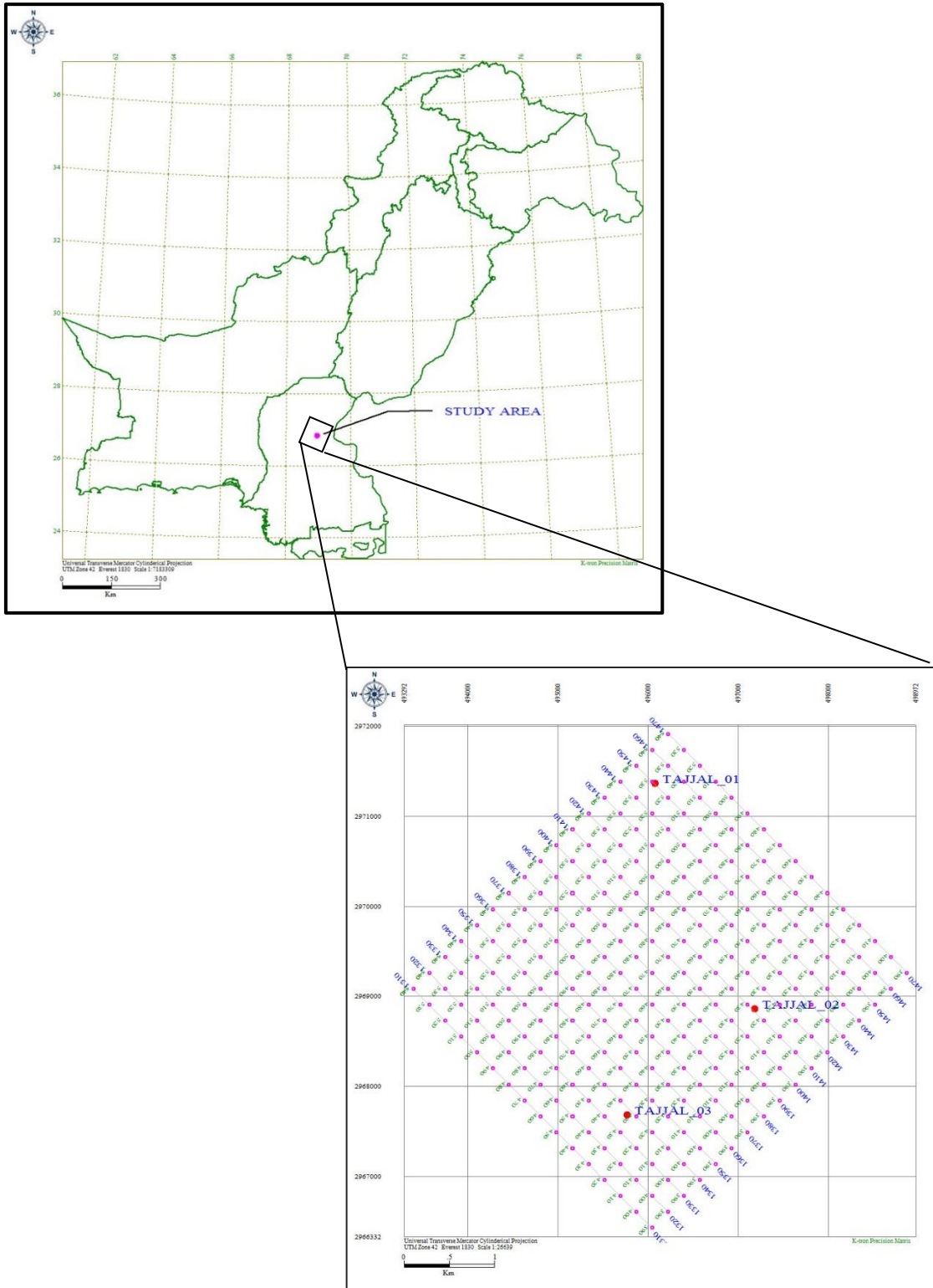


Figure 1.1 Study Area in context of Pakistan

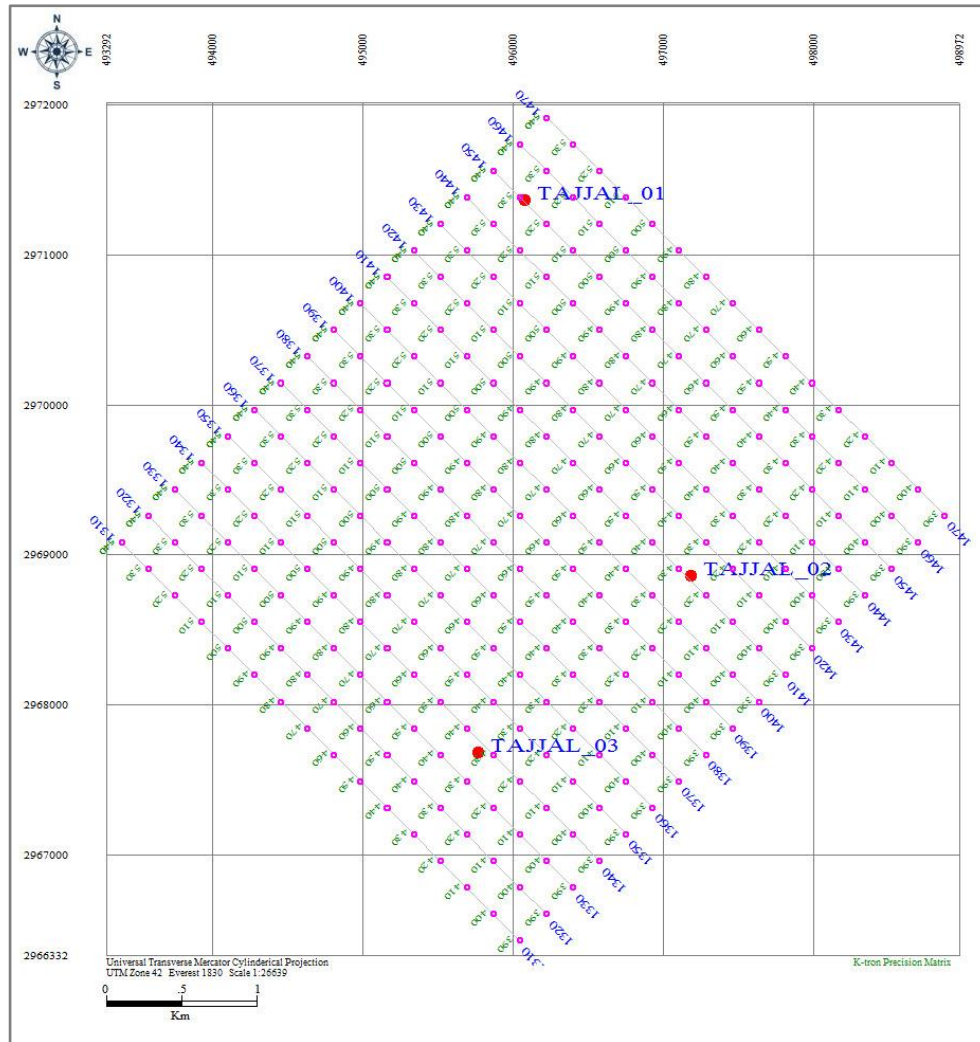


Figure 1.2 Gambat Latif Cube.

1.3 Exploration History

OMV announced the successful testing and discovery of gas in its Tajjal 1 exploration well which is located in Gambat Exploration Block in northern Sindh province, Pakistan. OMV collaborated with Pakistan petroleum limited(PPL), Eni and Government Holdings Private Limited(GHPL) in their joint venture and OMV announced start of Tajjal-1 extended well test that later on led to the discovery of Tajjal gas field, which is situated approximately 120 kilometers to the southeast of Sukkur in the Sindh province of Southern Pakistan (TAJJAL gas field - PPL).

OMV (Pakistan) is the main operator in Gambat exploration license, and it has a 35% stake in the consortium, together with Pakistan Petroleum (30%), Eni (30%) and Government Holdings (private) Ltd. (5%). Tajjal-2 and Tajjal-3, the two appraisal wells were discarded because they turned out to be dry. Despite being initially designed and completed as a producer in May 2011. The Tajjal-4 eventually started to produce an excessive amount of sand-filled water (TAJJAL gas field - PPL).

1.4 Objectives

- Mapping Identification of structural style and faults present in study area with the help of seismic data interpretation.
- The assessment of most optimized seismic attribute on seismic data to validate structural and stratigraphic interpretations, with a particular focus on identifying thin beds.
- To characterize Lower Goru Sand intervals in the reservoir through the application of Model-Based Inversion.
- Estimation of volume of shale, porosity, water resistivity and saturation of water and hydrocarbons with the help of petrophysical analysis.
- Computation of shear sonic by using Machine Learning and validating the results by AVO.
- Facies identification by Machine Learning.
- Identification of thin beds of Lower Goru Formation by Machine Learning.
- Calculation of various geomechanical properties such as vertical effective stress, pore pressure etc. by using Machine Learning.

1.5 Available Data

Two types of data were provided by LMKR after the approval of DGPC.

- 3-D data of Gambat Latif block covering an area of 12 squares kilometers in format of SEG-Y.
- Tajjal field well data in the format of Las files

Table 1.1 Data provided by LMKR.

Seismic Data	Well Data
3D Seismic cube of Gambat Latif block	well suits of Tajjal 1 and Tajjal 2 and Tajjal 3

1.6 Software Used

- IHS Kingdom software.
- Geographix Software
- Wavelet software.
- HRS software.

1.7 Literature review

One of the widely used methods for characterization of the reservoir is seismic inversion. Seismic inversion aids in combining the seismic and well data for predicting the characteristics of reservoir (Wang et al., 2017). Reservoir characterization of mixed facies and tight sands in Central Indus Basin Pakistan was performed by (Toqeer et al., 2021) . By making use of seismic data and well log data as an input reservoir modeling, model based seismic inversion and post stack seismic inversion was done along with generation of cross plots of effective porosity and acoustic impedance.

By making use of seismic attributes interpreters are able to extract more information from original seismic data. By using 2D seismic data as input and by performing seismic attribute analysis, Goru Clastic of Indus Basin Pakistan were evaluated by (Tayyab et al., 2017).

2D and 3D seismic data was used for analyzing the reservoir potential of Southern Indus Basin, Pakistan by performing model based and Stochastic inversion and by making cross plots of neutron and density logs (Asim et al., 2016).

By using 3D post stack seismic data as input dataset, spectral decomposition and coherence attribute were used by (Tayyab et al., 2017) in order to find fluvial sand reservoirs Southwest Pakistan's Indus Basin.

Reservoir quality and petrophysical analysis of Lower Goru Formation was performed by (Qadri et al., 2019) by using well log data of number of wells including Mehrab-1, Kadanwari-4, Gajwaro-1, Kadanwari-3 and Nara-1.

Artificial neural network and seismic inversion analysis were used by (Qiang et al., 2020) to predict the reservoir quality of Sawan Gas field, Pakistan. During this research cross plots of porosity and acoustic impedance were created and support vector machine was used.

1.8 Purpose of research

Although previous studies have made use of seismic interpretation, petrophysical analysis seismic attributes and inversion in order to evaluate the hydrocarbon potential of various areas of Southern Indus Basin. However, there is no work on making use of machine learning to identify the thin packages of sand in Lower Goru Formation of Gambat Latif block.

Based on the above literature review it was revealed that there is no work on making use of machine learning to identify the thin packages of sand in Lower Goru Formation of Gambat Latif block. Along with that no research has been previously done for calculation of geomechanical parameters of wells in Gambat Latif block.

So, my research will focus on thin bed detection by seismic attributes. Cluster based facies identifications by making use of Machine Learning and neural network, computation, and validation of shear sonic using machine learning and facies analysis, geomechanical parameters calculation, and creation of cross plots such as V_p , V_s , density etc.

1.9 Methodology

The following methodology would be adopted to fulfill the objectives mentioned.

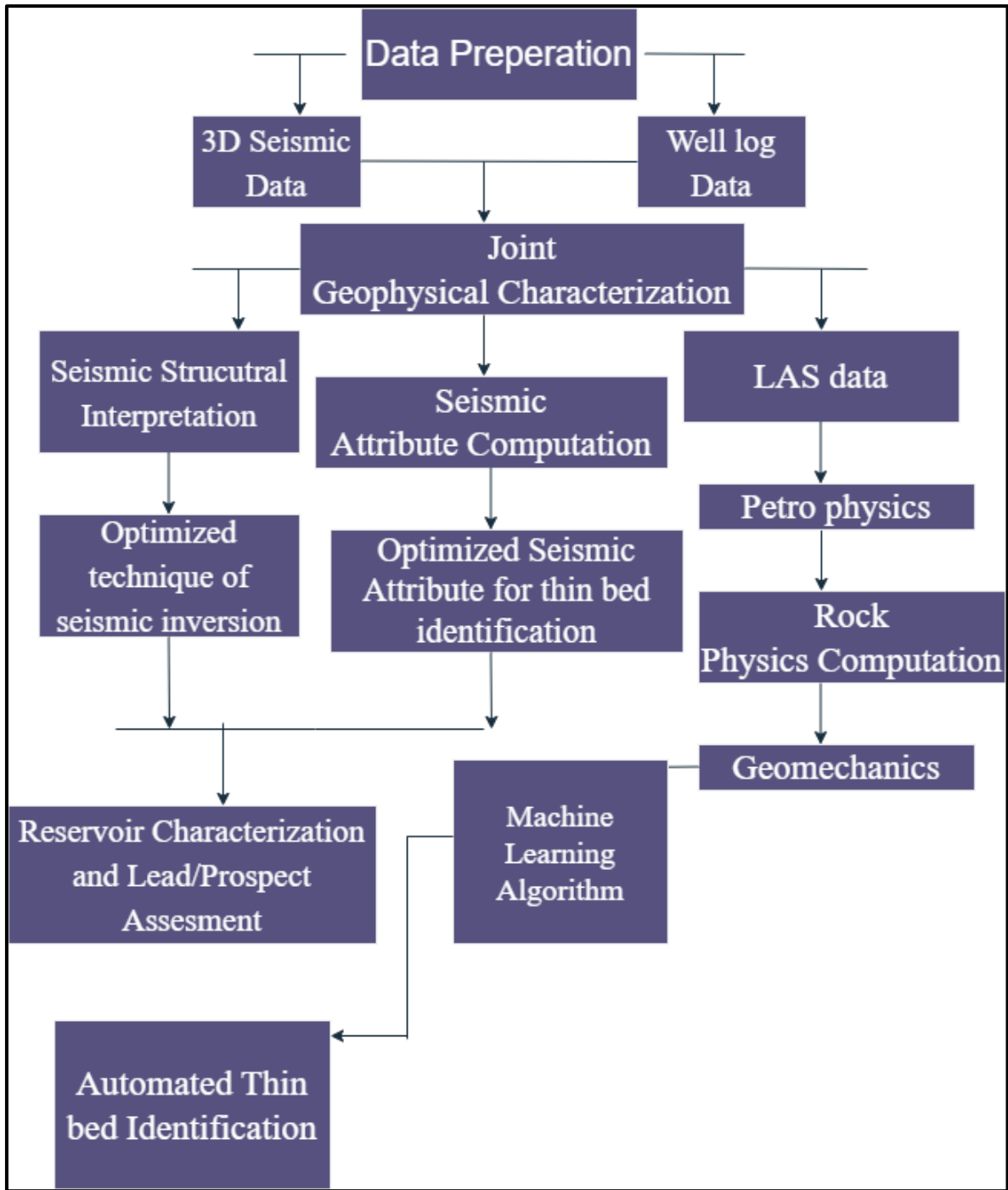


Figure 1.3 Workflow for methodology adopted during research.

CHAPTER 2

REGIONAL GEOLOGY AND STRATIGRAPHY

2.1 Introduction

Geology deals with the study of the dynamics and physical history of the earth, the rocks that make up its surface, physical, chemical, and biological changes the earth has gone through or is currently undergoing at the moment. Gambat Latif area is located in Khairpur district of Sindh province. In terms of geomorphology, the research region is situated between the southern desert and Chhistan desert(north) and geologically the Tajjal gas field (Gambat Block) is located in the Lower Indus Basin. Nearly 3648.73 square kilometers make up the Gambat Block. Within the Gambat Block, the Tajjal gas field is a producing field with coordinates $26^{\circ} 52' 50''$ N and $68^{\circ} 55' 60''$ E. Pannu Aqil Sub Basin, Kirthar Sub Basin, Indian Shield, and Kirthar Fold Belt form the northern, southern, eastern, and western boundaries of the region (Khan et al., 2016).

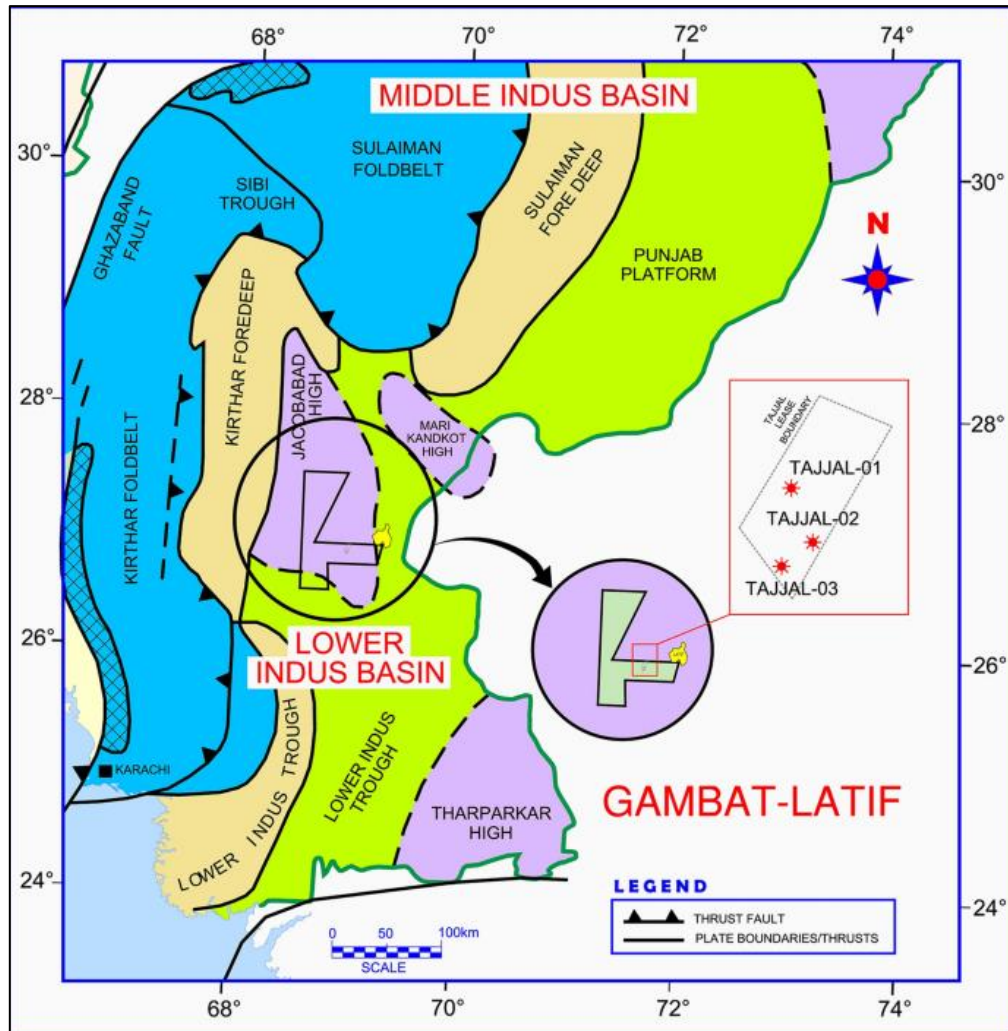


Figure 2.1 Study Area Location Map (Toqeer et al., 2021).

2.2 Basins of Pakistan

With an extent of over 83,000 square kilometers and including both onshore and offshore features, Pakistan is home to two significant sedimentary basins: Indus and Balochistan (Kazmi and Jan, 1997).

The Indus Basin extends north-northeast into Afghanistan and east-southeast into India. However, the Balochistan basin is located west of the Indus basin and extends into Afghanistan to north and Iran to the west. The Murray Ridge and the left-lateral Belo Ornach Chaman transform faults zone, which has a north-south trend, separates these two basins

(Ahmad et al., 1994). According to the sedimentation history of the sedimentation and type of the Indus Basin is segmented in three sections including the Upper, Central, and the Southern Indus basins (Ahmad et al., 1994).

2.2.1 Upper Indus basin

In northern Pakistan Upper Indus Basin is located. Sargodha Highs separate the Upper Indus Basin from Lower Indus Basin. MBT lies in the north of the Upper Indus Basin whereas strike slip faults Jhelum and Kalabaugh are located in the east and west (Ahmed et al., 1994). Upper Indus Basin is further divided into Potwar and Kohat Provinces.

2.2.2 Lower Indus Basin

The Lower Indus Basin is classified into the Central Indus Basin and the Southern Indus Basin. The study area Gambat Latif is located in the Lower Indus Basin (Ahmed et al., 1994).

2.3 Regional tectonic setting

The stratigraphic and structural characteristics of Indus Basin are all associated with the Indian's plate northwards drift from the Paleozoic to the recent (Wandrey et al., 2004). During the Permian-Middle Jurassic, the Indian Plate was located in the Southern Hemisphere alongside some continents including Antarctica, Africa, and Australia (Powell, 1979). The rifting started and during the Jurassic the Antarctica and Australian plates detached from the Indian plate (Ahmed et al., 2018).

Structures that have developed in response to different tectonics are quite significant and also important for the hydrocarbon's accumulation. In hydrocarbon exploration, identifying the structural traps is very critical yet an important task. This is because a large

number of hydrocarbon resources in the world have been discovered on sites/locations where there is closure of the structural traps (Ahmed et al., 1994).

On the western edge of the Indian Plate, the Southern Sindh Monocline is located, and during its tectonic history, the Indian Plate has undergone several episodes of extension, rifting from the Gondwanaland till it's eventual welding to Asia (Ahmed et al., 2018).

Many structures within the Southern Sindh Monocline's subsurface are distinguished by numerous tectonic occurrences of the Indian plate's rifting when it rifted from the Gondwanaland, until its collision with Asia, along with the rifting from other plates at various geological periods (Ahmed et al., 2018).

The structures in the examined area provided evidence for three major structural episodes, which are classified as:

- The structures linked to the rifting of the Indian plate from Gondwanaland throughout the Late Jurassic to the Early Cretaceous.
- The reactivation and modification of previously formed structures during the Middle Cretaceous when Madagascar rifted separation from Indian Plate.
- When Indian Plate collided with Asia in the Early Eocene, the structures were reactivated and inverted (Ahmed et al., 2018)

2.4 Structural Setting of Gambat-Latif Area

A large number of structural styles and structures are associated with the extensional tectonic setting, and it is thus very challenging to understand how these structures have evolved. In numerous extensional basins around the world, researchers have looked at the evolution of structures discovered in extensional tectonic settings (Ahmed et al., 2018).

The research area is situated on the eastern and southeastern sides of the regional Jacobabad-Khairpur high, which runs north to south. This high plays a significant role in creating structural traps in the study area, particularly in the Kadanwari, Sawan, and Tajjial gas fields. The Jacobabad-Khairpur high underwent dome uplifting in the early Cretaceous

period, and subsequently, deep-seated faults developed in the Late Cretaceous (Khan et al., 2016).

The structural configuration of the study area is primarily influenced by three significant tectonic events. First, there was an uplift and erosion during the late Cretaceous period (Khan et al., 2016). The second event involved late Paleocene right-lateral wrenching, and the third event was the Late Tertiary to Holocene uplift and inversion of Khairpur (Khan et al., 2016). Geologically the Tadjal gas field (Gambat Block) is located in the Lower Indus Basin (Southern Indus Basin) and as the study region is situated in the Lower Indus Basin and falls into an extensional tectonic regime there is presence of extensive Horst and Graben geometry which is considered a probable hydrocarbon bearing zones (Khan et al., 2016).

2.5 Stratigraphy of the study area

In the Southern Indus basin, the oldest rocks are of Triassic age and the stratigraphy of the Southern Indus basin ranges from Wulgai Formation of Triassic age to the Siwaliks of Pleistocene age (Dar et al., 2021).

There is an unconformity among the Jurassic carbonates and the lower most Cretaceous clastic sediments (Goru Formation) (Kadri, 1995). In the western and the northern parts of the Southern Indus Basin, the Sembar Formation is made up of silt, shale, and marl. Between 1955 and 1984, about 55 exploratory wells were drilled in the Southern Indus Basin. Onshore drilling in the Southern Indus Basin is not hindered by the post Eocene over pressured strata. However, with contemporary drilling techniques these issues can be easily overcome because in the offshore pressures are mostly determined by depth and only weakly by stratigraphy (Qadri, 1986).

AGE	STRATIGRAPHY		LITHOLOGY	
RECENT / PLIOCENE	ALLUVIUM / SIWALIKS			
E O C E N E	KIRTHAR FM.	DRAZINDA MB.		
		PIRKOH MB.		
		SIRKI MB.		
		HABIB RAHI MB.		
	LAKI FM.	GHAZIJ MB.		
		SUI MAIN LST. MB.		
PALEOCENE	DUNGHAN FM.			
	RANIKOT FM.			
	PARH FM.			
UPPER CRETACEOUS	GORU FM.	UPPER GORU MB.		
LOWER CRETACEOUS		LOWER GORU MB.	SHALE INTERVAL	
			"D" INTERVAL	
			"C" INTERVAL	
			"B" INTERVAL	
			"A" INTERVAL	
	SEMBAR			
JURASSIC	CHILTAN			

Figure 2.2 Stratigraphy of Lower Indus basin (Abbasi et al., 2021).

Different Nomenclatures are used by different industries to divide the Lower Goru Formation into different intervals. However, during my research I used the division by OMV which is as follows:

Chrono-stratigraphy	Formation	OMV stratigraphy	ENI stratigraphy		
Cretaceous	Lower Goru	D Interval	H Sand		
			C Interval	G Sand	
			F Sand		
		B Interval	E Sand		
			D Sand		
	Early	Albian	A Interval	C Sand	
				Aptian	B Sand
		Barremian			Sembar
		Hauterivian			Sembar
		Valanginian		Sembar	
Berriasian	Hiatus				

Figure 2.3 Nomenclature of Lower Goru by OMV and ENI.

2.6 Petroleum play

The various geological or geochemical elements and processes that make up petroleum geology are referred collectively as the petroleum system. Oil and gas fields wouldn't develop if any of these petroleum system's elements are missing (Magoon et al., 1991). To estimate the size of a petroleum system, the following methodology is often employed:

- First, the discovered petroleum deposits are genetically categorized in accordance with stratigraphic features and geochemical characteristics.
- Secondly, petroleum-source correlation approaches are used to determine the source that gave rise to the specific petroleum occurrences (Magoon et al., 1991).

- Lastly the geographic extent of active source pod that gives rise to all of genetically related petroleum occurrences (Magoon et al., 1991).

2.6.1 Source Rock

Discoveries in the Lower Goru play are situated within the platform region of the Middle and Lower Indus Basin, spanning from the vicinity of the Mari High down to the Badin area. The reservoir sands in the Middle Indus Platform area were primarily charged by hydrocarbons migrating from the underlying Lower Cretaceous regionally established organic-rich shales, notably the Sembar Formation. Additionally, organic-rich shales within the Lower Goru Member, as observed in analogues such as the nearby Sawan, Miano, and Kadanwari gas fields, also contributed to the hydrocarbon charge. These shales are characterized by the presence of terrestrial organic material, exhibiting a total organic carbon (TOC) content ranging from 0.5% to 1.7%. They predominantly contain Type III kerogen and have been actively engaged in gas generation processes since the late Cretaceous to early Tertiary periods. A number of petroleum discoveries in the Southern Indus Basin have been confirmed to have originated from the Lower Cretaceous Sembar Formation (Aaadil et al., 2014). Shale makes up the majority of the Sembar Formation, but it also contains limestone and other minor lithologies such as siltstone and sandstone (Aaadil et al., 2014).

At the Sembar pass, the formation's type locality, the formation has a total thickness of 133 meters, but at the Moghal Kot outcrop portion it has a thickness of 262 meters (Bender and Raza, 1995). In the south-east region of Southern's Indus Basin the Sembar Formation thins out (Ahmed et al., 2013).

2.6.2 Reservoir Rock

In the Lower Indus Basin and Middle Indus Basin of Pakistan, the Early Cretaceous Lower Goru Formation exists as a conventional reservoir. The generation of reservoir heterogeneity within the Lower Goru Formation is primarily attributed to factors such as

depositional environments, diagenetic alterations, the presence of shale intercalations, and the distribution patterns of shale layers. The Lower Goru Formation is lithostratigraphically separated into two parts: the upper parts are primarily made of sandstone, siltstone, and thin interlayers of shale and limestone, while the bottom parts are mostly made of sandstone along with limestone and shale interlayers (Ahmed et al., 2018).

The Lower Goru Formation's sandstone is further split into sand intervals A, B, C, and D based on the reservoir quality (Dar et al., 2021). Different nomenclatures are used by different companies to divide the Lower Goru Formation into different intervals. However, during my research I used the Nomenclature given by OMV.

2.6.3 Seal Rock

The primary seal rock for the Sembar-Goru petroleum play in the Southern Indus basin is shale from the Upper Goru Formation. The Sembar, Goru Shale, and Kirthar formations act as shale layers and have been verified as successful sealants in numerous wells, such as those in the Bhiit, Zamzama, Hallel, and Mehar fields (Dar et al., 2021). Within the producing fields the thin shale beds having variable thickness act as effective seals (Dar et al., 2021). The Paleocene and Eocene formations in the Northern Sulaiman ranges contain substantial shale layers, which have the potential to act as effective sealing horizons beneath formations such as the upper Ranikot and Ghazij (Dar et al., 2021).

2.6.4 Trapping mechanism

The Kirthar Fold Belt and a significant portion of the Lower Indus Basin have been characterized as structurally intricate. This complexity is primarily a result of extensive folding and the presence of positive flower structures, which can be traced back to the reversal or inversion of a prior system of normal faults (Dar et al., 2021). The Indus Basin's major production is from structural traps. Tilted fault blocks, Anticlines and thrust faulted

anticlines are the various varieties of structural traps present in the study region. In the Lower Indus Basin tilted fault traps are produced due to extensional tectonics (Dar et al., 2021).

CHAPTER 3

SEISMIC DATA INTERPRETATION

Seismic interpretation's primary goal is to precisely characterize the lithology and subterranean geological formations. Rocks that contain hydrocarbons can be distinguished from rocks that do not by using seismic data analysis (Ahmad et al., 2021).

Seismic interpretation becomes quite challenging in areas of complex tectonics. Therefore, in such cases in order to carry out accurate interpretation it is necessary to make correct observations in both subsurface as well as surface data (Zamora et al., 2022).

The seismic record consists of two essential elements. The initial aspect involves the timing of the arrival of any reflection (or refraction) from a geological boundary, while the second is the shape of the reflection (Bouvier et al., 1991). The lithology and fluid content of the seismic reflector being studied are frequently deduced from the seismic data (Bouvier et al., 1991).

Seismic interpretation is divided into structural interpretation and stratigraphic interpretation. The goal of structural seismic interpretation is to create structural maps of the subsurface using the observed three-dimensional configuration of the arrival times. A model of cyclic episodes of deposition relates to the pattern of reflection observed through seismic sequence stratigraphic interpretation (Bouvier et al., 1991).

Digital representations of seismic data, recorded by each channel of the recording instrument, are expressed as time series. Processing algorithms are formulated and

utilized for either individual single-channel time series or multichannel time series (Yilmaz, 2001). The Fourier transform forms the fundamental basis for a substantial portion of the digital signal processing methods used in the examination of seismic data. Beyond the sections that address one- and two-dimensional Fourier transforms and their real-world applications, the core principles of signal processing also include a dedicated section that explores a diverse compilation of seismic data recorded from various regions worldwide (Yilmaz, 2001). Through reference to field data examples, interpreters analyze the type of seismic signals, including primary reflections from layer boundaries and various forms of noise, both random and coherent (Yilmaz, 2001).

3.1 Seismic Interpretation's Workflow

In order to perform Seismic Interpretation, the following workflow is adopted.

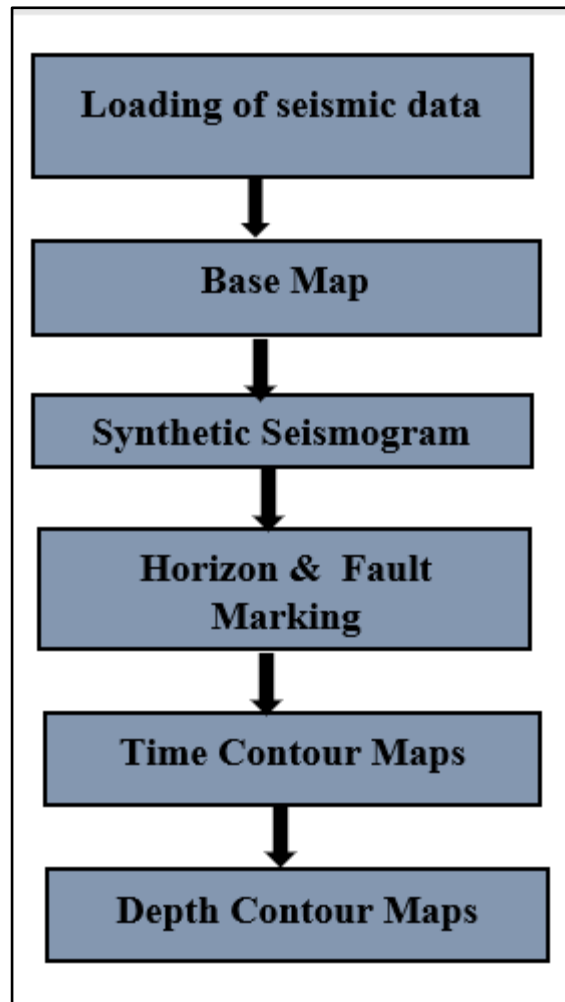


Figure 3.1 Workflow adopted for seismic interpretation adopted during research.

3.1.1 Loading of Seismic Data

3D seismic data cube in SEG Y format of Gambat Latif area was provided by DGPC. The data was loaded into IHS Kingdom software by using the SEG Y headers for cross line and inline loading.

3.1.2 Base Map

After the completion of the seismic data loading, the base map of the provided cube is generated. The base map displays how the overall grid is oriented. There are two types of lines in a 3D cube: inlines and cross lines. The cross line lies between the numbers 390 and 540, as illustrated in Figure 3.2, while the inline runs from 1310 to 1470. The Tajjal 01 is located on inline 1459 and cross line 520, Tajjal 02 is located on inline 1407 and crossline 420.

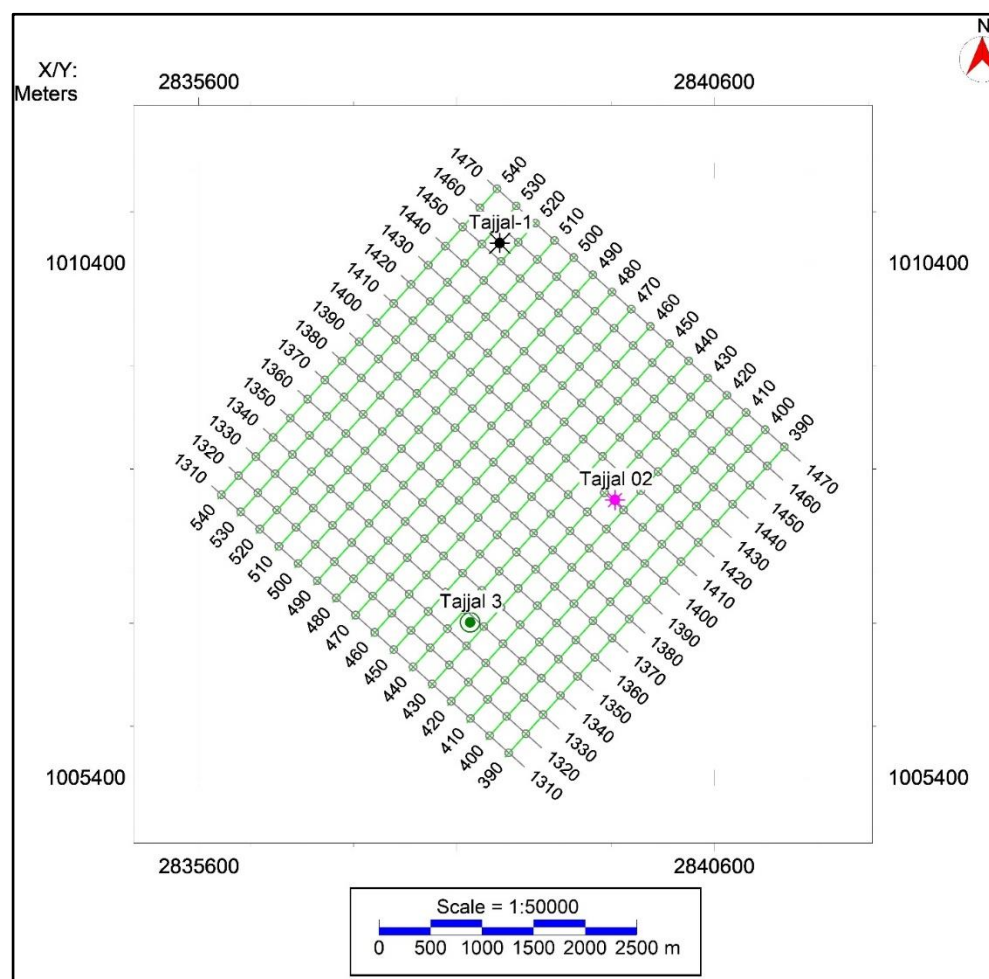


Figure 3.2 Base map of the study area showing the distribution of inlines and crossline along with type of well.

3.1.3 Synthetic Seismogram

Synthetic seismogram serves as a "tie" in hydrocarbon exploration between seismic reflection data collected at the same location and changes in rock characteristics observed in a borehole (Helmberger et al., 1989). The wavelet derived from seismic data is convolved with the reflectivity derived from digitized acoustic and density logs to generate the synthetic seismogram. Interpretations of data can be improved by comparing the marker beds or other correlation points noted on the well logs with the notable reflections on the seismic section (Helmberger et al., 1989).

Synthetic seismogram's ability to match depends on a variety of parameters and these are as follows:

- How well seismic data is processed?
- Quality of the well logs
- Ability to extract a representative wavelet from seismic data (Helmberger et al., 1989).

Synthetic seismogram is essential to make a correlation between seismic data and the geological data which is in form of well logs. In order to make a synthetic seismogram following elements are needed:

- Sonic log
- Time Depth Charts
- Density log
- Reflection coefficient (RC)
- Acoustic Impedance(Z)
- Wavelet

Once the synthetic seismogram is created its signature and the original seismic data's signatures are compared. From the adjacent seismic trace in the vicinity of the wells, a seismic trace was taken for each well. This extracted trace represented the original seismic data to be used in the synthetic matching. After that the signature of the synthetic seismogram and seismic data were compared. Shift and stretch were then used to make alterations and

once the nature of seismic data and synthetic seismogram matched the well to seismic tie was completed (Kelly et al., 1976).

A seismogram is necessary for a well-to-seismic tie. Therefore, density log and sonic log from the Tajjal 02 and Tajjal 01 along with gamma ray log is also used as a references log.

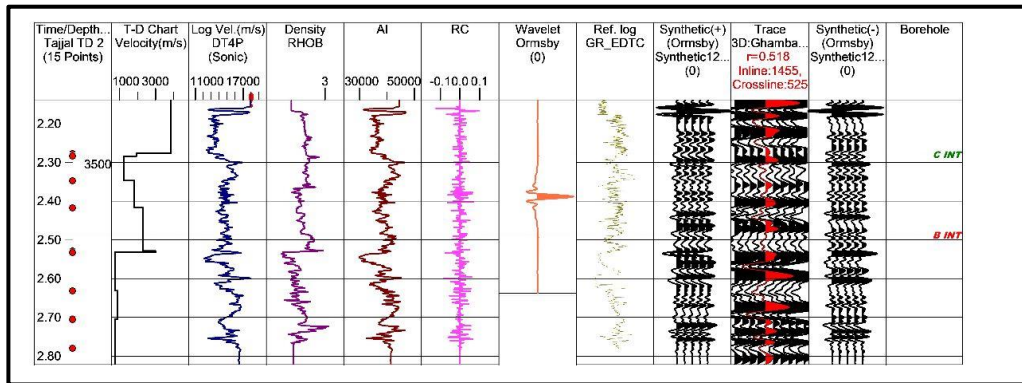


Figure 3.3 Synthetic Seismogram of Tajjal-02.

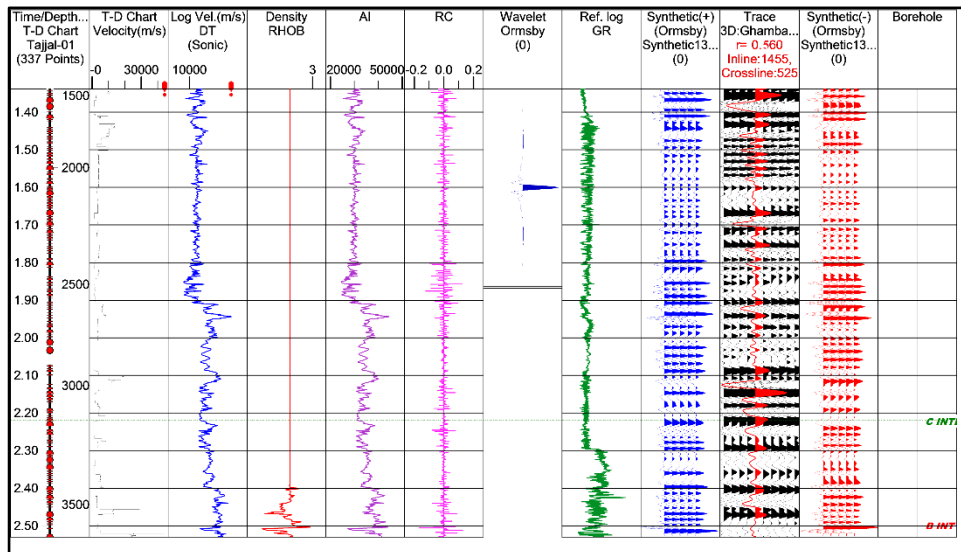


Figure 3.4 Synthetic Seismogram of Tajjal-02.

3.1.4 Horizon and fault marking

Interpreting and marking various horizons on seismic data is the first and most fundamental step in seismic interpretation. Understanding the structure and stratigraphy of the research area is necessary for accurate interpretation. Two horizons are interpreted, namely C-Interval and B-Interval. These are the sand intervals of Lower Goru Formation.

Faults are interpreted from seismic data whenever there is a specific break or discontinuity in the bedding. Two faults were marked named Fault 1 and Fault 2. Both are normal faults.

Identifying the pattern of the faults becomes quite easy when one knows about the stress regimes that exist in the study area. Usually, the reverse faults are associated with compressional tectonics regimes and normal faults are dominant in the extensional tectonics (Freeman et al., 1991). The study area Gambat-Latif area lies in the extensional tectonic regime and thus there is presence of normal faults.

The research area's fault extension is defined by fault correlation, which also delineates dip directions and specifies the throw which is actually vertical component of the separation and heave which is the horizontal component of slip. The fault correlation aids in defining the fault's network. On seismic data the faults are interpreted when there appears a certain breakage on the seismic section (Freeman et al., 1991).

- **Interpreted sections conclusion:**

On the seismic section two horizons C-interval and B-interval were marked both lie within 2 to 5 seconds. Along with two horizons, two faults were also marked on the seismic section. Both of these faults are normal faults named F1 and F2. Both these faults cut the B-interval and C- interval. The trend of both faults is from NE to SW, and both are dipping towards NW. The nature of faults shows that this area is situated in extensional tectonic regime since these are normal faults and displacement along fault 1 is also observed shown in Figure 3.6. Figure 3.4, 3.5 and 3.6 show interpreted horizons on different inlines.

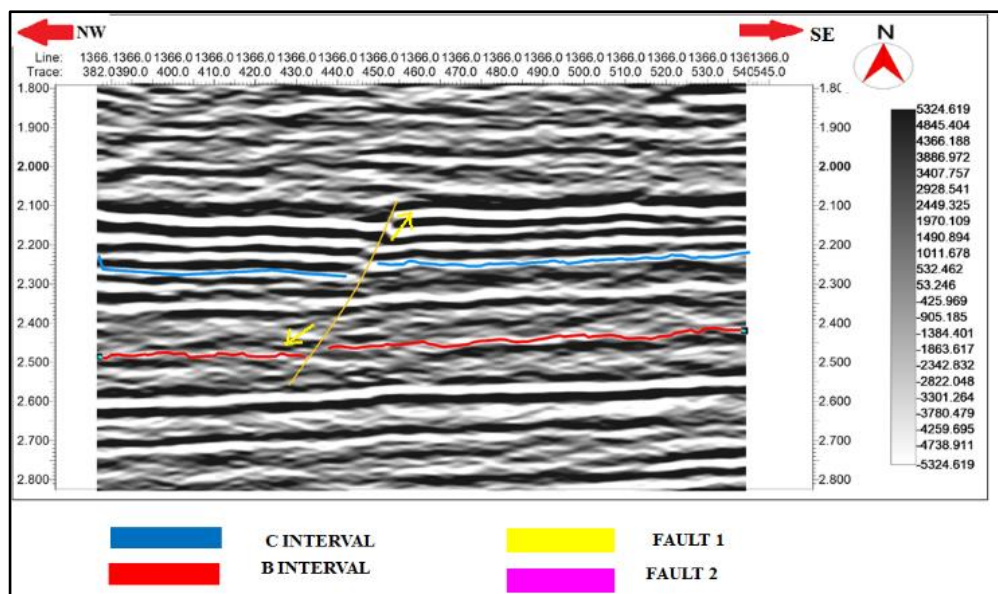


Figure 3.5 Seismic section of Inline 1419 with well location of Tadjal- 02 along with the C and B Intervals with fault F1.

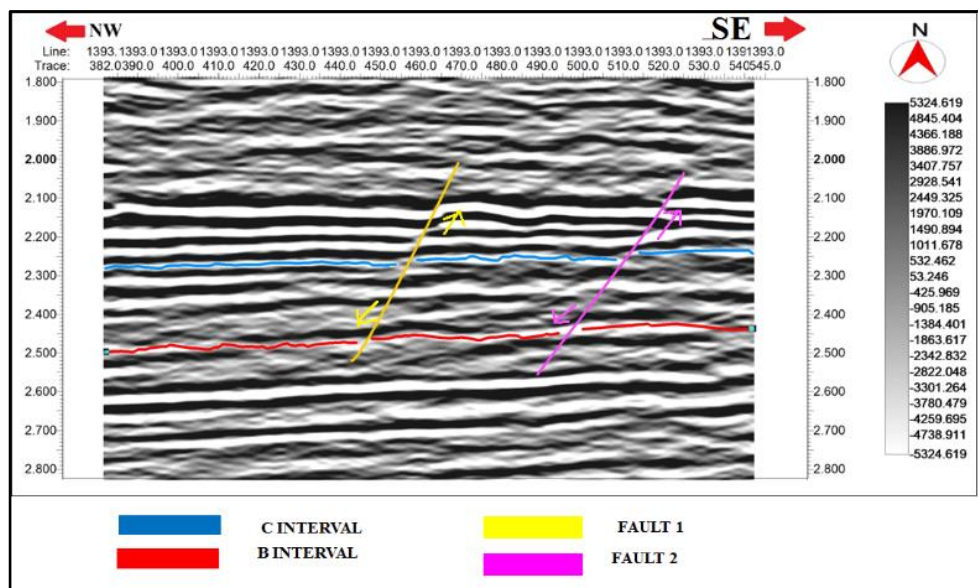


Figure 3.6 Seismic section of Inline 1393 with the C and B Intervals with faults F1 and F2.

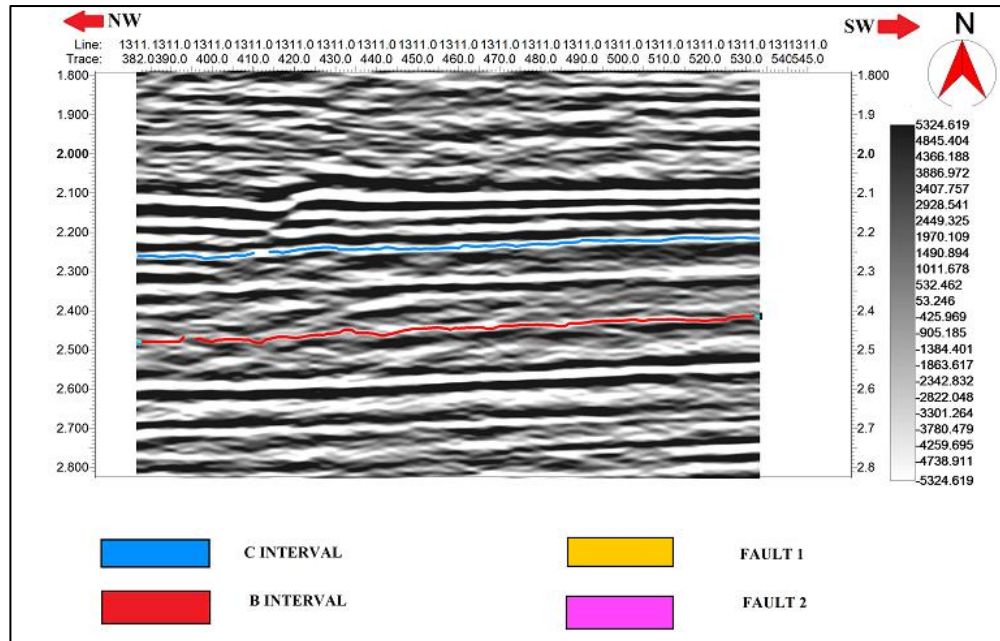


Figure 3.7 Seismic section of Inline 1311 showing displacement of fault F1.

3.1.5 Preparation of Contour Maps

The creation of contour maps is the last stage of interpretation. Lines that connect points of the same depth, height, or time are called contours.

TWT contour maps are initially created in the seismic interpretation, followed by depth contour maps. Seismic maps are another name for contour maps. The seismic map is typically the end result of seismic exploration, the one on which the success of the entire exploration's operation depends. A map may be used to highlight specific areas during meetings with the management, but the map itself is crucial for deciding where and if to drill for oil (Caputo & Postpischl, 2010).

Time and depth contour maps are the last stage of seismic interpretation. First, the time contour maps are created because the data is readily available in time and then using the velocity function to transform the time sections into depth section, depth contour maps are

created. Lower Goru's C and B interval's time and depth contour maps are created and explained.

3.1.6 Interpretation of C-interval maps

On the basis of seismic data seen in the time and depth maps of the C-interval horizon, two faults designated as F1 and F2, are interpreted in the C-interval horizon. Both of the mentioned faults are normal faults. From the time contour map of the C- interval, the strata on the western side are shallower than those on the eastern side.

The trend of both faults is from NE to SW, and both are dipping towards NW. The nature of faults shows that this area is situated in extensional tectonic regime since these are normal faults.

The time contour map of C interval is shown in Figure 3.7. The time ranges for this interval ranges from 2.208 to 2.288 seconds. Time contour values are on the higher side on eastern side of C interval map depicting that the horizon becomes relatively deeper in this area whereas the time contour vales are on smaller side on the western side which shows that in this part the horizon becomes shallow. The contour interval in the map is 0.0025 seconds. The horizon is trending from northwest to southeast. The strata exhibit a decreasing time range from east to west. Chances of hydrocarbon accumulation is in western side as hydrocarbons are present at shallow time.

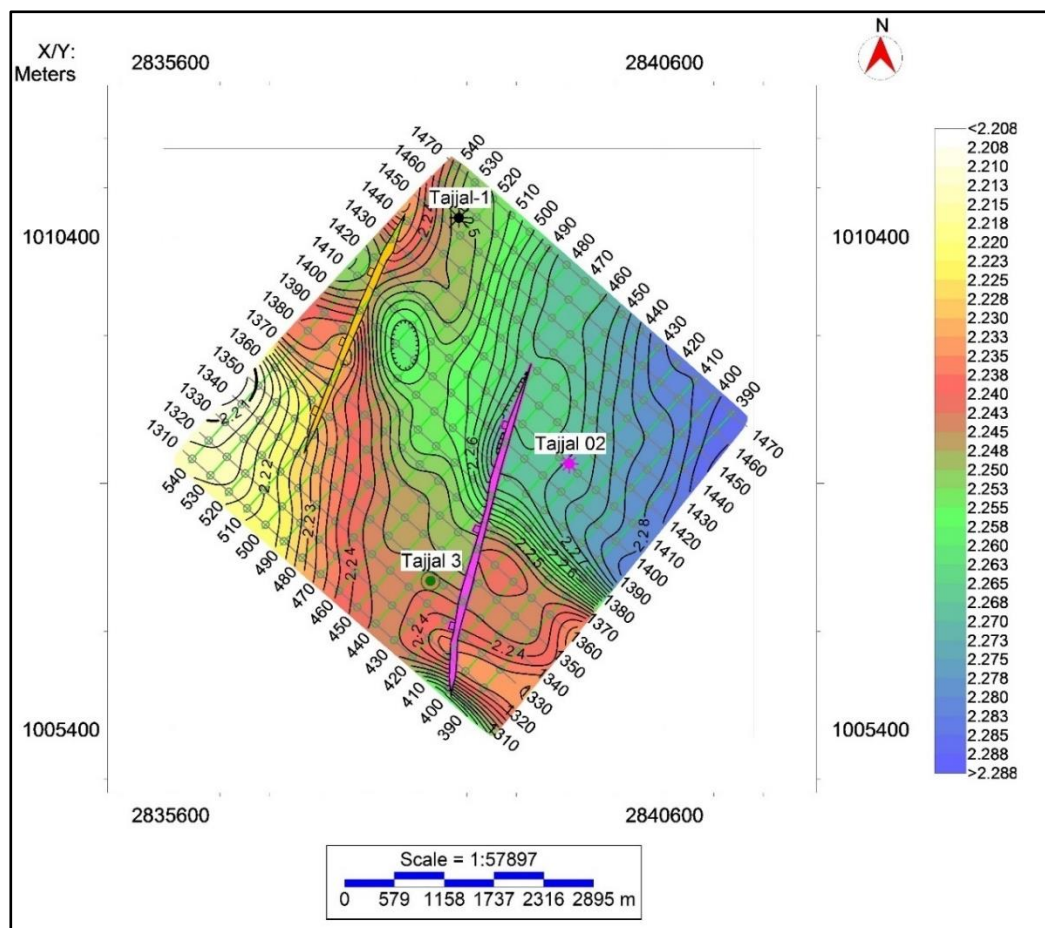


Figure 3.8 Two-way travel time contour map of C-Interval

As shown in Figure 3.8 depth contour map of C interval ranges from 3124 to 3234 m. The contour interval in this map is 10 m. The unit of the depth contour map is meters. The depth contour map of C-interval shows the same trend as C-interval time contour maps i.e., on the eastern side greater values lie, and the values become higher till 3234 m whereas on the western side contour values become smaller and decrease to 3124 m. The color bar depicts how the map's contour varies. The strata exhibit a decreasing depth range from east to west. Chances of hydrocarbon accumulation is in western side as hydrocarbons are present at shallow depth.

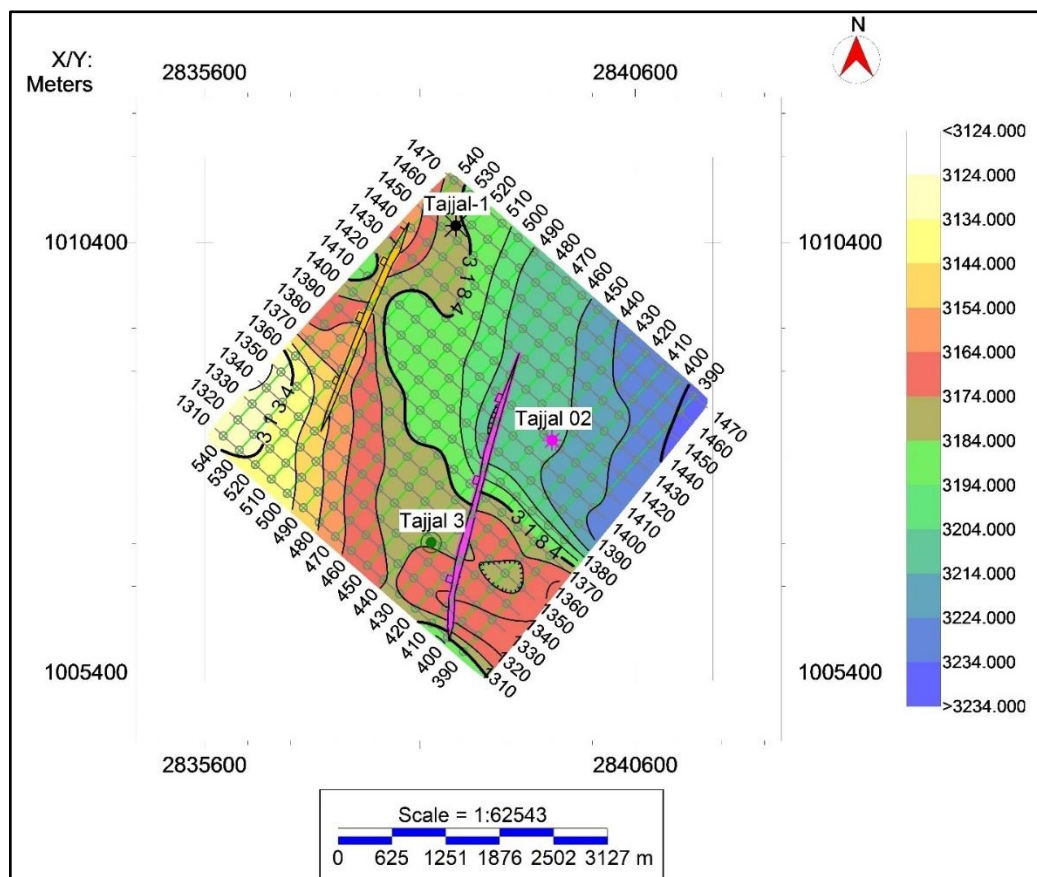


Figure 3.9 Depth contour map of C-Interval.

3.1.7 Interpretation of B-interval maps

The time contour map of B-interval map ranges from 2.271 to 2.514 seconds. The contour interval is 0.0025 seconds. Time contour values are highest at the eastern side of B-interval map depicting that the horizon becomes deeper in the eastern side whereas the time contour values are decreasing towards the west showing that at the western side the horizon becomes shallower. From east to west strata is relatively getting shallower i.e., showing less time which might be indicative of hydrocarbons.

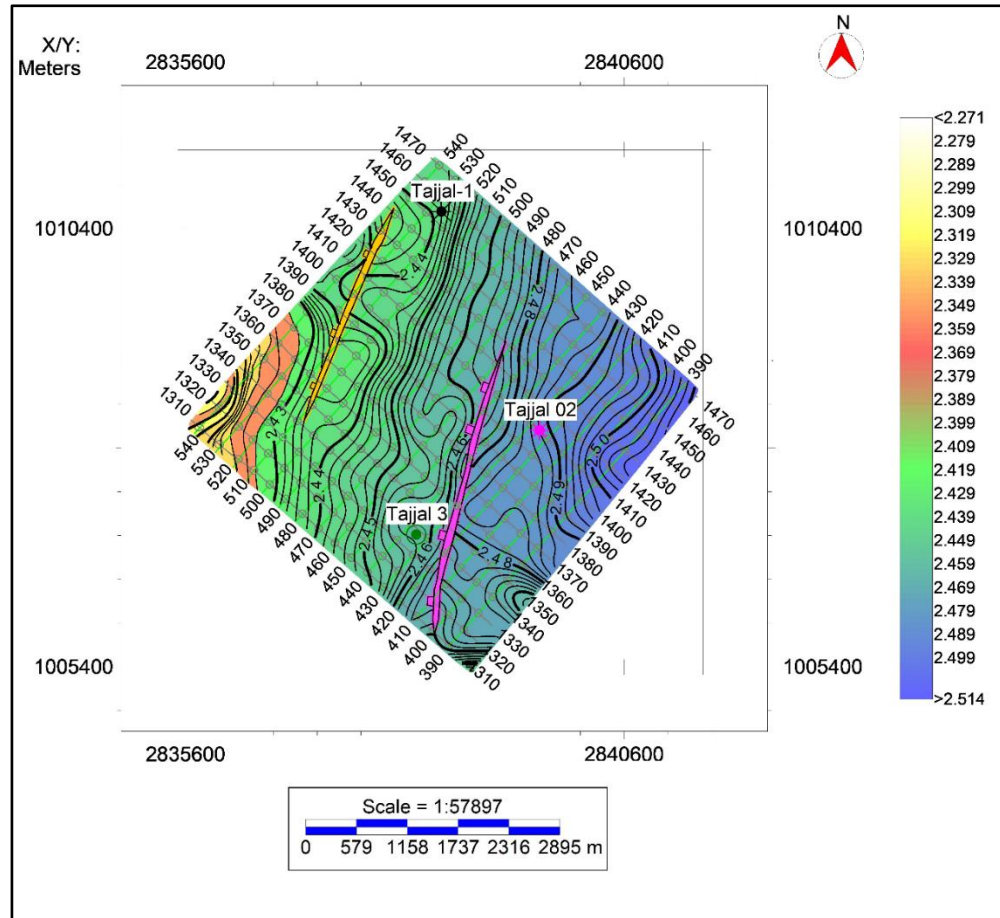


Figure 3.10 Time contour map of B-Interval.

As shown in Figure 3.10 the depth contour map of B-interval ranges from 3362.5 to 3762.5 m. The contour interval in this map is 10 m. The unit of depth contour maps is meters. The depth contour map of B-interval shows the trend that on the eastern greater values lie, and the values become higher till 3762.5 m whereas on the western side, contour values become smaller and decrease to 3362.5 m. The color bar depicts how the map's contours vary.

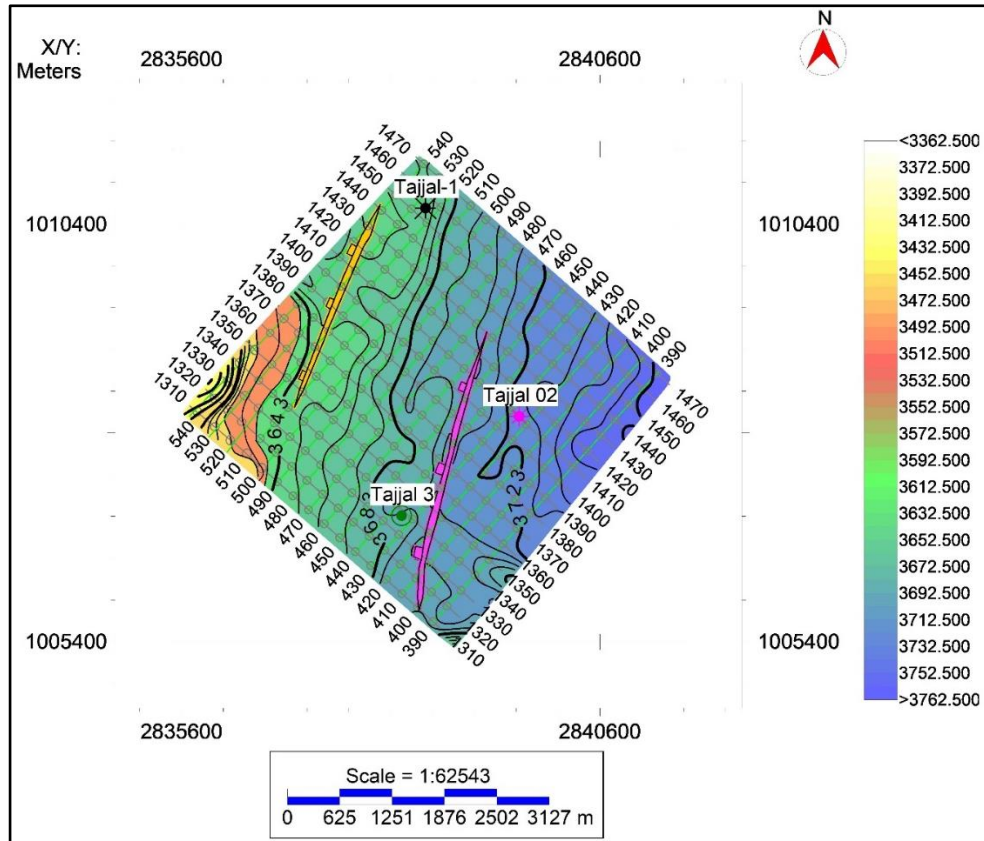


Figure 3.11 Depth contour map of B-Interval.

CHAPTER 4

PETROPHYSICAL ANALYSIS

4.1 Introduction

Rock principles' study and their interaction with fluids (such as water, gas, or oil) is called petrology (Rider, 2002). Measurements of well log are transformed into the reservoir parameters (such as porosity, permeability, saturation, mineral component volume, and V_{cl}) by making use of petrophysical interpretation (Bisht et al., 2013).

The chemical and physical characteristics of oil and gas deposits, as well as the surrounding rocks and soil, are studied and analyzed by Petro physicists. Petro physicists gather and study information on these reservoirs, such as the rock's density, pore pressure, electrical and acoustic characteristics, and radioactivity level. The information they gather can be used to calculate the amount of oil and/or gas present, how permeable the rocks are, and whether it can be extracted (Bisht et al., 2013).

Steps adopted to perform petrophysical analysis:

- LAS files loading.
- Marking Zone of Interest
- Calculation of V_{sh} and V_{clean}
- Porosity Estimation
- Calculation of R_w
- Water Saturation

➤ Hydrocarbon Saturation

The initial step in log interpretation is the demarcation of the zone of interest. The well logs are used to estimate petrophysical characteristics such as porosity, shale volume (V_{sh}), fluid saturation (oil and water), resistivity of water (R_w), etc.

4.2 LAS files loading

Las files of Tajjal 01 and Tajjal 02 were imported in the Geographix software using the Prizm utility. Well suites of these two wells were imported in the Prizm consisting of sonic(DT), PEF log curves, MSFL, LLS, LLD, caliper, neutron porosity (PHIN), bulk density (RHOB) and spontaneous potential (SP) curves. Porosity and resistivity tracks were adjusted in accordance with the correlation scales determined by the data at hand. The GR scales range from 0-150 API, the SP ranges from -100 to 50 mv, the caliper ranges from 6 to 16 inches. MSFL, LLS and LLD range from 0.2-2000 Ohm-m. Bulk densities range from 2.0 to 3 gm/cc and neutron porosity scale ranges from 0.45 to -0.15 v/v. In contrast to PEF log which has a scale of 1-10b/e, sonic DT log has a scale of 140-40 micro sec/feet.

4.3 Marking Zone of Interest

Given below is the list of criteria that are to be kept in mind while marking the zone of interest:

- 1) Caliper log should be stable.
- 2) The Gamma log should display low values for low clay content. Less gamma ray value indicates the presence of clean lithology, which is a reservoir's defining feature (Ali et al., 2019).
- 3) LLD > LLS > MSFL. The resistivity log suite is significant because it gives a picture of the subsurface based on electrical resistivity. The resistivity logs MSFL, LLS and LLD are three crucial ones. A zone of hydrocarbon exists if

there is a substantial difference between the MSFL and LLD curves. If there isn't a difference between them, water might be present there (Glover, 1998).

- 4) There should be a crossover between Neutron and Density logs. Neutron and density curve values must decrease to reach crossover. Both neutron and density logs can be used to determine the reservoir's porosity. Neutron and density log values must fall for crossover to occur, which is a definite sign of a hydrocarbon zone (Abdulaziz et al., 2019).

4.4 Calculation of Petrophysical Parameters

The following petrophysical parameters were calculated throughout the study.

4.4.1 Calculation of volume of shale

Shale volume is determined by natural gamma ray log. By subtracting the gamma ray maximum (GRmax) from the gamma ray minimum (GRmin) values from the GR log, the volume of shale is determined (Rider, 1986).

However, in the study area there is presence of hot sands (sands having high radioactivity) that is why the conventional formula for calculating the volume of shale was not used, the volume of shale was calculated by using neutron and density logs.

The Lower Goru Formation's sand intervals in the Sawan gas field and surrounding areas are extremely diverse and are regarded as hot sands since they reflect a high value of gamma ray and sonic logs, thus making it difficult to determine the reservoir zones with precision using traditional petrophysical studies (Mabrouk et al., 2011). The sand intervals of this formation are made-up of Quartz, feldspar, chloride, glauconite, volcanic rock fragments, and trace amounts of calcite (Mabrouk et al., 2011). When radioactive materials other than shale are present, the shale volume calculated using the naturally occurring gamma rays usually overestimates the shale volume (Mabrouk et al., 2011).

The formula used to calculate the volume of shale during this study is as follows:

$$V_{Shl} = \frac{(\rho_B - \rho_M + \phi N \times (\rho_M - \rho_F))}{(\rho_{shl} - \rho_M + HI_{shl} \times (\rho_M - \rho_F))} \quad (4.1)$$

Where:

V_{Shl} : Volume of shale

ρ_B : Bulk density log value

ρ_M : Density of the matrix(non-shale rock)

ϕN : Neutron porosity log value

ρ_F : Density of the fluid(typically water)

ρ_{shl} : Density of pure shale

HI_{shl} : Hydrogen index of the shale

4.4.2 Calculation of Volume of clean

The volume of clean can be calculated by using the formula given by (Rider, 1986).

The formula is as follows:

$$V_{Clean} = 1 - V_{Shl} \quad (4.2)$$

4.4.3 Calculation of Density Porosity

Using the values from the density log, density porosity is computed, and the resulting formula is as follows.

$$\Phi = \frac{(\rho_{ma} - \rho_b)}{(\rho_{ma} - \rho_f)} \quad (4.3)$$

Where,

ρ_{ma} = Density of matrix for limestone/sandstone=2.71/2.65 g/cm³

ρ_b = Bulk density of the formation

ρ_f = Fluid's density

Φ = Density porosity of rock

4.4.4 Calculation of Average Neutron Density Porosity

The rock's porosity values are estimated using neutron log, also known as neutron porosity. A formation hydrogen index (HI) is estimated by neutron log. Since hydrogen is mostly present in reservoir rocks, neutron porosity logs primarily respond to the fraction of the pores. Average neutron density porosity is the weighted average of density and neutron porosity (Ward, 1984). The resulting formula is as follows:

$$\varphi_{avg} = \frac{(D\varphi + N\varphi)}{2} \quad (4.3)$$

where: φ_{avg} = Average porosity,

$D\varphi$ = Density porosity,

$N\varphi$ = Neutron porosity

4.4.5 Calculation of Effective Porosity

Effective porosity is the percentage of a porous material's total empty space that can transmit a fluid. The proportion of total void volume to total bulk volume is known as total porosity. Porosity ratios are typically stated as a percent after being multiplied by 100 (Abdulaziz et al., 2019).

In a porous medium that is saturated with fluid, only the interconnected pores will allow fluid to pass through. Effective porosity, also known as interconnected porosity, is defined by interconnected pores (Koponen et al., 1997). The formula for effective porosity is as follows:

$$\varphi_{eff} = \varphi_{avg} \times (1 - V_{Shl}) \quad (4.4)$$

where:

φ_{avg} = Average porosity,

φ_{eff} = Effective porosity,

V_{Shl} = Volume of shale

4.4.6 Resistivity of Water Calculation

The Pickett plot method is used to calculate the resistivity of water. The X and Y axis of the Pickett plot shows deep resistivity and porosity log, respectively which is built on the logarithmic of the Archie's equation. On a straight line which has a negative slope of the volume of m, saturation point(S_w) will be plotted. Zones of water define the lowest line on the plot.

Because $S_w=1$, it is possible to determine the water resistivity from a location on the line. Once the water line is formed, further parallel lines with various S_w can be drawn while assuming a constant n. Other data can afterwards be plotted and assessed in relation to S_w . The Pickett plot was used to calculate the resistivity of water in both the wells. Figure 4.1 and Figure 4.2 are shown below. The resistivity of water in Tajjal 01 is 0.0265 and resistivity of water in Tajjal 02 is 0.027.

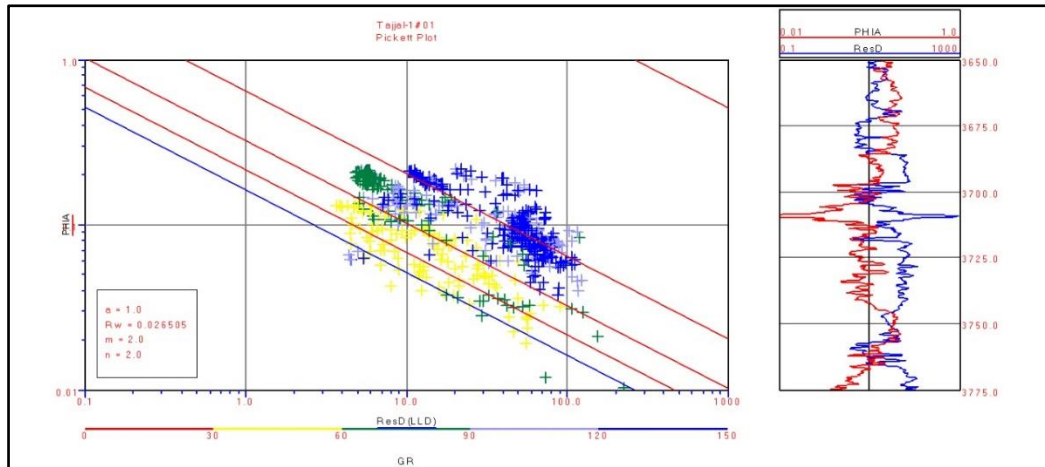


Figure 4.1 Resistivity of water for TAJJAL 01 by Pickett plot method.

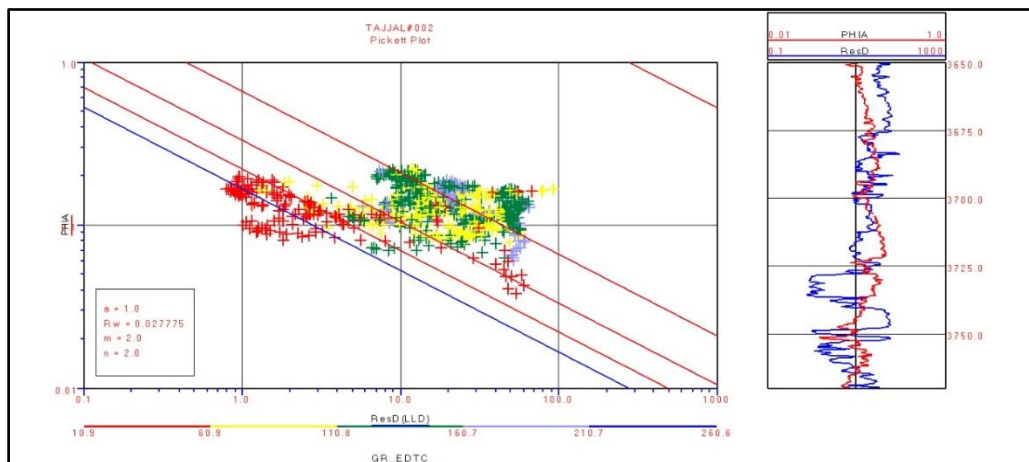


Figure 4.2 Resistivity of water for TAJJAL 02 by Pickett plot method.

4.4.7 Calculation of Archie Water Saturation (S_w)

The amount of water in a formation is referred to as water saturation (Ahmed, 2009). Archie presents the mathematical method that is used to calculate the water saturation and resistivity logs are used for this purpose. Using Archie's equation, the reservoir zone's water saturation was calculated. By making use of the formula mentioned below:

$$S_w = \left\{ \left(\frac{a \cdot R_w}{R_t \cdot \phi A} \right)^m \right\}^{\frac{1}{n}} \quad (4.5)$$

Where,

- S_w = water saturation,
- ϕA = average porosity,
- a = lithological coefficient (taken as 1),
- m = cementation factor (taken as 2),
- n = saturation exponent (taken as 2).
- R_t = True Resistivity
- R_w = Water Resistivity

4.4.8 Calculation of Hydrocarbon Saturation (Sh)

Water saturation is the percentage of pore spaces that have water in it (S_w). Hydrocarbon saturation (Sh) is the remaining fraction containing oil or gas. The formula used to calculate hydrocarbons saturation is as follows:

$$Sh = 1 - S_w \quad (4.6)$$

4.5 Petrophysical Interpretation of B interval

Petrophysical analysis of B and C intervals of Lower Goru Formation was carried out in the zone of interest.

Petrophysical interpretation of Lower Goru Formation (B interval) of Tajjal 01 and Tajjal 02 wells were carried out in the reservoir zones of interest. The procedure begun by loading the LAS files of both wells using the Prizm module of Geographix software.

Zones of interest were marked based on the criteria mentioned in 4.2. It was noticed that by keeping the criteria in mind two zones were marked in B interval of Tajjal 01 well and 1 zone was marked in B interval of Tajjal 02 well.

4.5.1 Petrophysical Interpretation of B Interval Tajjal 01

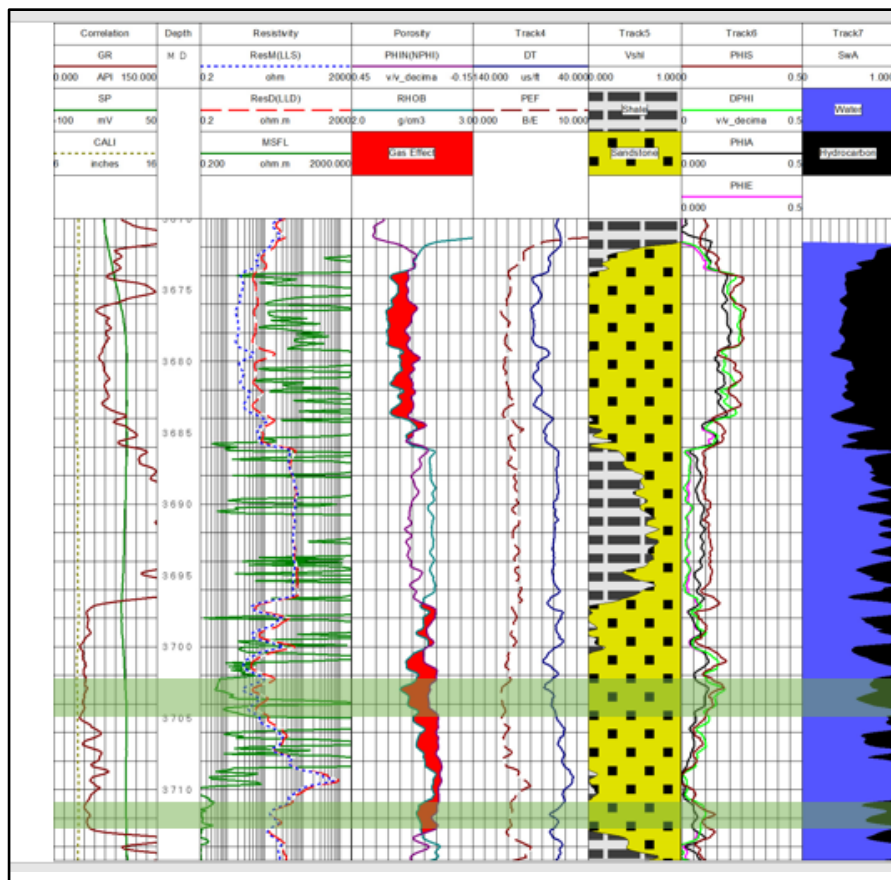


Figure 4.3 Petrophysical analysis of Tajjal-1 on B-Interval of Lower Goru Formation.

Two zones of interest were marked in the Lower Goru B- Interval of Tajjal 01 well. The first zone was observed at the depth of 3702-3705 m, and the second zone was observed at the depth of 3711 to 3713 m.

Within both these zones the gamma ray value was on the lower side, separation between MSFL and LLD was observed. There was presence of gas effect i.e., neutron and density crossover was observed. And lastly the hydrocarbon saturation was also good.

4.5.2 Petrophysical Interpretation of B Interval Tajjal 02

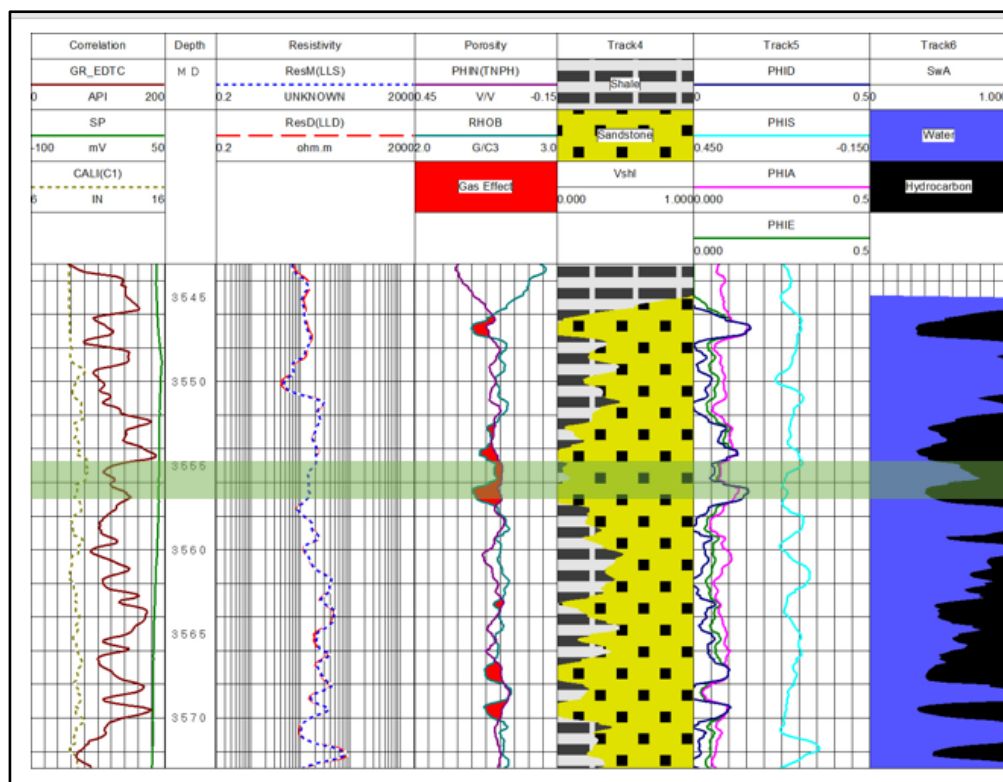


Figure 4.4 Petrophysical analysis of Tajjal-2 on B-Interval of Lower Goru Formation.

1 zone was observed in the B Interval of Tajjal 02 well. This zone lies at the depths of 3555-3557 m. Since MSFL log is not available in this well the criteria to mark the zone of interest based on the separation between MSFL and LLD was ruled out. Within the area of study there is presence of radioactive sands which results in very high gamma ray values. This phenomenon is also observed in the case of this zone of interest. It was thus marked as zone of interest based on the presence of gas effect and high values of hydrocarbon's saturation.

Every wireline logging device is impacted in some way whenever shale is present in a formation. The gamma ray device will result in an excessively large shale volume due to the presence of radioactive minerals other than shale. This is especially true for dolomite and radioactive sands (Kamel et al., 2023).

4.6 Petrophysical interpretation of C interval

Petrophysical interpretation of Lower Goru Formation(C interval) of Tajjal 01 and Tajjal 02 wells were carried out in the reservoir zones of interest. The procedure begun by loading the LAS files of both wells using the Prizm module of Geographix software.

1 zone was marked in C interval of Tajjal 01 well and 3 zones were marked in C interval of Tajjal 02 well.

4.6.1 Petrophysical Interpretation of C Interval Tajjal 01

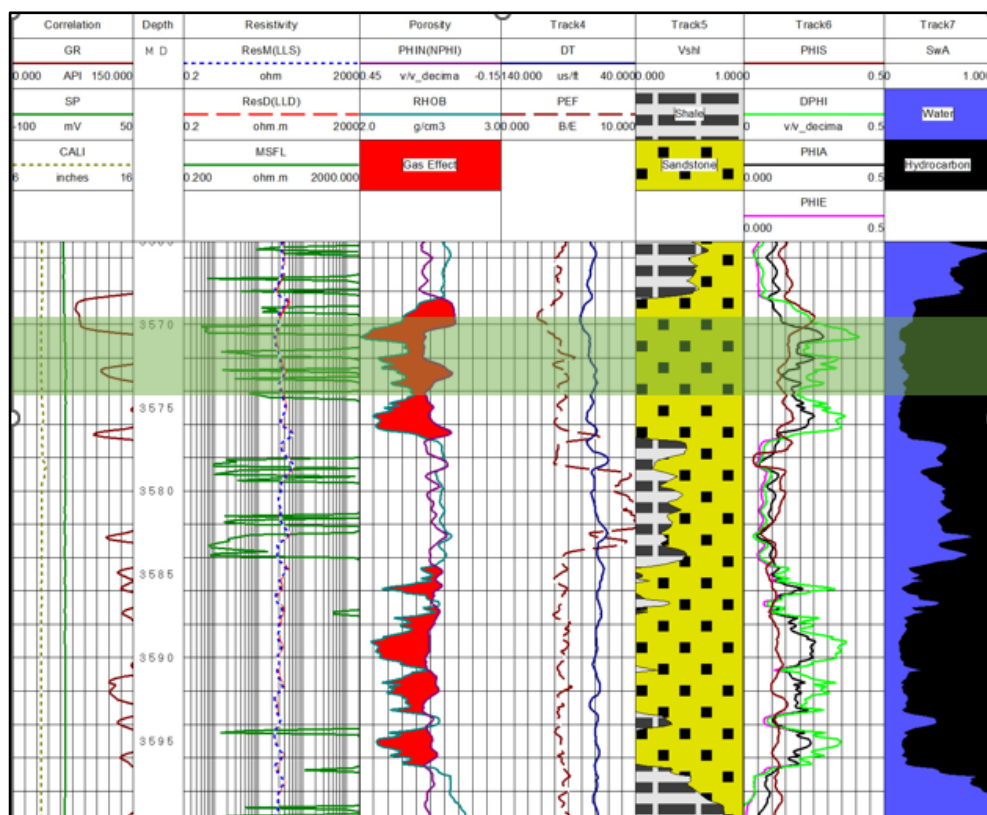


Figure 4.5 Petrophysical analysis of Tajjal-1 C-Interval of Lower Goru Formation.

A single zone of interest was marked in the Lower Goru C- Interval of Tajjal 01 well. The zone lies at the depth of 3570-3574 m.

Within this zone the separation between MSFL and LLD was observed. There was presence of gas effect i.e., neutron and density crossover was observed. And lastly the hydrocarbon saturation was also good. The gamma ray values were on the higher sides due to presence of radioactive sands (Mabrouk et al., 2011).

4.6.2 Petrophysical Interpretation of C Interval Tajjal 02

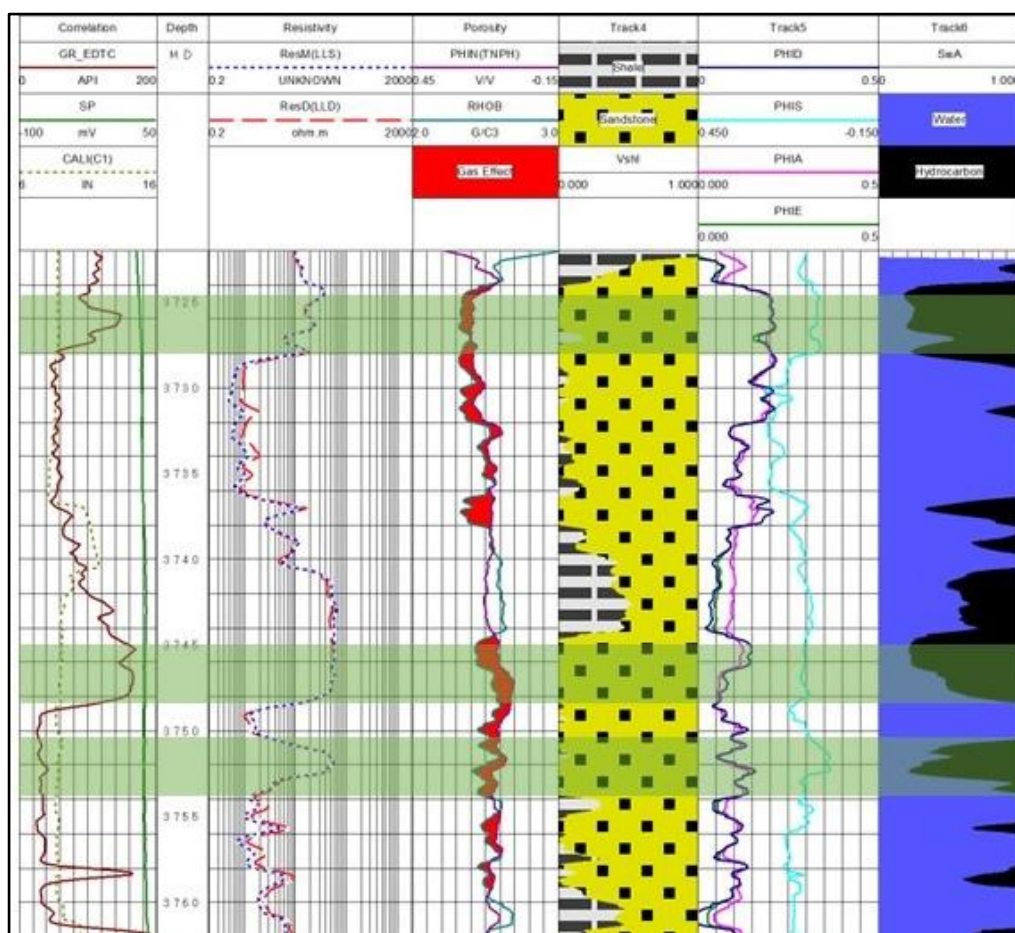


Figure 4.6 Petrophysical analysis of Tajjal-2 C-Interval of Lower Goru Formation.

Three zones of interest were marked in the Lower Goru C-Interval of Tajjal 02 well. The first zone was observed at the depth of 3725-3728 m, the second zone was observed at depth of 3745-3748 m, and the third zone was observed at the depth of 3750 to 3754 m.

Within the third zone the gamma ray value was on the lower side. Since MSFL log is not available in this well the criteria to mark the zone of interest based on the separation between MSFL and LLD was ruled out. However, within all the three zones there was presence of gas effect i.e., neutron and density crossover was observed. And lastly the hydrocarbon saturation was also good.

4.7 Results of Petrophysical Interpretation

Table 4.1 Result of petrophysical analysis of reservoir zones

Well Name	Hydrocarbon Zone	Depth(m)	Vshl %	PHIA %	PHIE %	SwA %	Sh %
Tajjal 1 C Interval	Zone 1	3570-3574	0	28	28	14	86
Tajjal 1 B Interval	Zone 1	3702-3705	0	11	11	61	39
	Zone 2	3711-3713	9	10	9.1	69	31
Tajjal 2 C Interval	Zone 1	3725-3728	1.9	21	17	22	78
	Zone 2	3745-3748	0	10	10	25	75
	Zone 3	3750-3754	0.20	14	13.9	29	71
Tajjal 2 B Interval	Zone 1	3555-3557	0.13	10	9.8	41	59

CHAPTER 5

SEISMIC INVERSION AND ATTRIBUTES

5.1 Introduction

Seismic inversion, which is a subsurface geological modelling approach uses well data as a control and seismic data as an input. The seismic inversion is carried out by converting the data in amplitude form to the impedance form (Kianoush et al., 2023).

Seismic inversion enhances interpretation by helping to identify the significant subsurface geological and petrophysical boundaries (Talib et al., 2022). Seismic inversion is one of the known methods for extracting valuable information from seismic data, interest in it has been growing steadily over the past few years. Seismic inversion also enhances the resolution of conventional seismic. Deterministic and probabilistic are the methods of inversion and the approaches are either pre or post stack (Veeken and Silva, 2004).

The procedure of turning seismic reflection data into seismic impedance is called seismic inversion. Acoustic impedance is a layer property since it is related to the layers rather than interface and it is the product of density and velocity (Onajite, 2014).

As acoustic impedance changes with lithology, porosity, fluid content, pressure, depth, temperature etc. Thus, it can be used as an indicator of lithology to precisely map flow unit, an indicator of porosity, an indicator of hydrocarbons and a tool for quantitative analysis. Thus, the result of inversion has a substantial impact on interpretation and ultimately decision making in the industry (Jain, 2013).

Earth's properties are reconstructed by seismic inversion, and it is readily employed in the industries of oil and gas. For the prediction of porosity and lithology it combines well data and seismic data. These characteristics of rock may be applied for the identification of hydrocarbons and reservoirs (Kianoush et al., 2023).

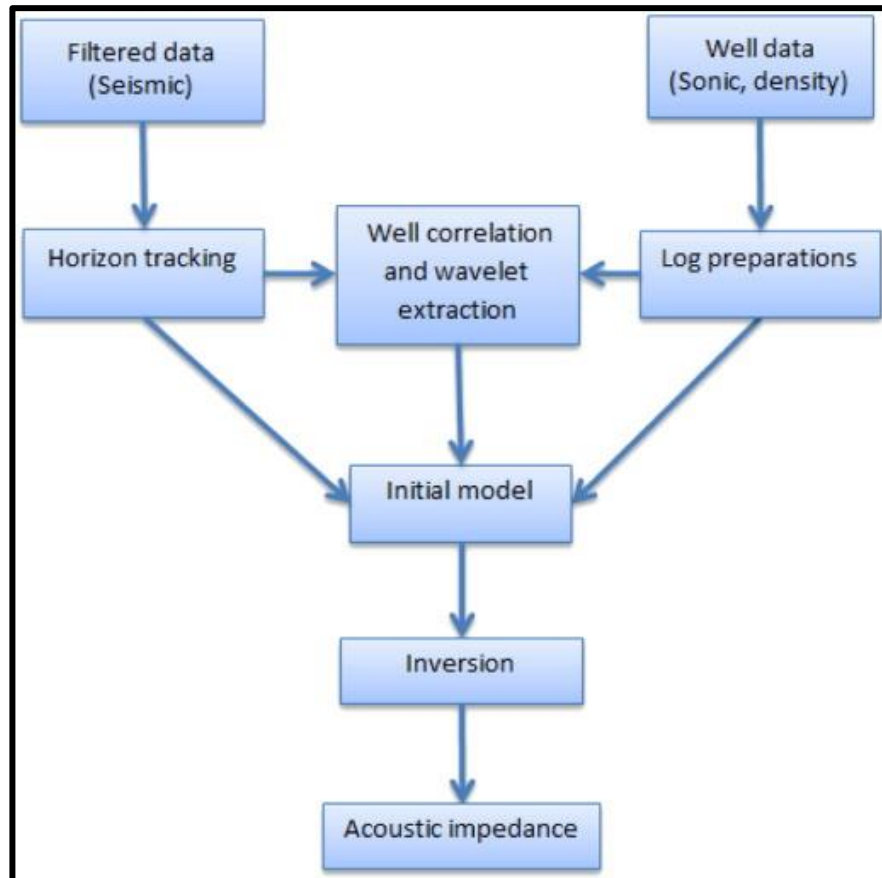


Figure 5.1 Generalized workflow of seismic inversion (Veeken and Silva, 2004).

Pre-stack seismic data and post-stack seismic data are the two types of seismic data that the seismic inversion method deals with. Both pre-stack seismic and post-stack seismic data are used in seismic inversion methods (Kumar et al., 2016). Post-stack seismic data only produces P impedance, whereas pre-stack seismic data also generates P and S acoustic impedance as well as their derivatives, such as V_p/V_s , Λ -rho, and μ -rho, which can

be used to estimate fluid and lithology parameters from the subsurface (Barclay, 2008). However, post stack inversion is performed in this research.

5.1.1 Seismic inversion's purpose

The main objective of seismic inversion is to convert seismic reflection data into quantitative rock properties that describe the reservoir. Acoustic impedance logs are calculated at each CMP in their most basic form (Barclay, 2008). Results using inversion improve resolution and support more precise interpretation as compared to working with seismic amplitude. This then makes it easier to estimate the reservoir characteristics like porosity and net pay (Pendrel, 2001).

Other advantages of seismic inversion include:

- Wavelets impacts within the seismic bandwidth are eliminated by using seismic inversion (Kianoush et al., 2023).
- Overburden is separated from reservoir properties.
- Impedance domains interpretation is typically simpler than seismic domain interpretation (Kianoush et al., 2023).

5.2 Post Stack Inversion

Post stack inversion procedures as the name implies pertain to a variety of methods used for transforming the stacked seismic data into quantifiable rock physics parameters. Porosity, saturation, shale content, and other reservoir properties are estimated using post-stack seismic inversion (Abosalama, 2022).

Acoustic impedance is often the product of post stack inversion's product is the Acoustic Impedance however, both acoustic and shear impedance can be produced by pre stack inversion. With its simple assumptions seismic post-stack inversion is a reliable

approach. It uses two distinct approaches: band-limited and broad band inversion (Karim et al., 2016).

5.3 Model Based Inversion

In the geophysical community, model-based seismic inversion is very common because it provides quick and accurate estimations of acoustic impedance. In a model-based inversion, the wavelet is convolved with the simplistic initial acoustic impedance model to produce a synthetic response that is compared to the actual seismic trace (Kianoush et al., 2023).

To create a synthetic seismic trace, using this method, the seismic trace (initial model) is convolved with a wavelet. Next, until the difference between the initial trace and invented trace is decreased to a limit value, the image is subjected to numerous iterations (Russell, 1988).

The output is free of noise component that is nearly always present with the seismic data because the model-based inversion does not use raw seismic data. Since the seismic data is band limited and direct inversion methods cannot provide the precision and accuracy needed by the exploration sector, model-based inversion is effective for thin reservoirs (Russell, 1988). High frequency and low frequency components both are present in the model based seismic inversion thus providing detailed information on stereographic and physical properties (Russell, 1988).

$$J = \text{weight } a \times (S - W * R) + \text{weight } b \times (M - H * R) \quad (5.1)$$

The seismic trace is denoted by S in the equation, the wavelet recovered from seismic data is denoted by W , the reflectivity series is denoted R , the initial model is denoted by M and H is integration operator (Russell, 1988).

Given the initial half of the equation is obviously modelled with seismic trace while the other part is modelled using an estimated initial model (Russell, 1988). Seismic trace was

modeled in the first quarter of equation and the estimated impedance was modelled in the second portion.

5.4 Methodology adopted for Model Based Inversion

The model-based algorithm of post stack inversion is performed by using Hampson and Russell software. The methodology adopted to perform the model Based seismic inversion consists of the following steps:

1. Seismic and Well Data Loading
2. Loading of horizons
3. Extraction of Statistical Wavelet
4. Seismic to Well correlation
5. Initial Low Frequency Model
6. Inversion Analysis
7. Results of Model Based Inversion
8. Slices

5.4.1 Seismic and Well Data Loading

The loading of seismic and well data into Hampson and Russell software is the first step in post-stack inversion. The 3D cube of Gambat Latif block is loaded into the software along with interpreted well data in Las format, following data loading the location of well is matched with seismic data for confirming the exact location of well in the seismic cube.

5.4.2 Loading of Horizons

The next step involves loading of horizons in the seismic section. The interpreted horizons are exported in time amplitude format from Kingdom Software. After that these

horizons are imported in HRS software. The horizons of B and C intervals of Lower Goru Formation were imported.

5.4.3 Extraction of statistical wavelet

One of the most important steps in quantitative interpretation is wavelet estimation. The outcomes of seismic inversion depend on the quality of the wavelet, which in turn determines the quality of the seismic correlation. The seismic wavelet is an essential link between seismic data and subsurface stratigraphy and rock characteristics (Cui et al., 2014).

Figure 5.2 shows the statistical wavelet that was used in inversion analysis from a window spanning 2200-2700 ms, wavelength 200 ms, and taper length 0.25 ms and the average phase of statistical wavelet is shown as dotted line in Figure 5.2.

Wave phase is crucial for seismic interpretation and inversion technique; for the best results the wave phase should be zero. The results of inversion are significantly impacted by input phase shift. If the phase shift is more than the error, resultant impedance will be higher (Jain, 2013).

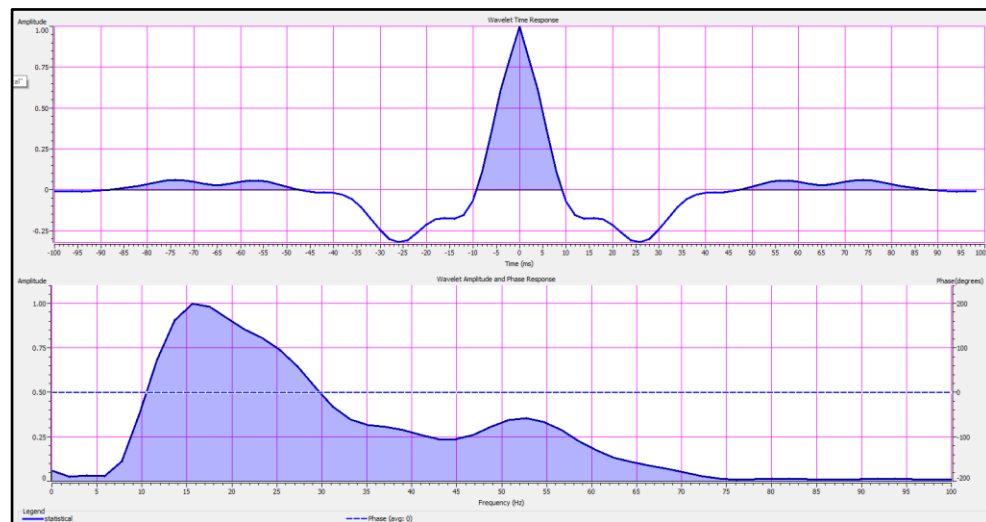


Figure 5.2 Statistical wavelet used in inversion analysis for Tajjal-02.

5.4.4 Seismic to Well Correlation

Tajjal-02 well is used for the purpose of correlation of well and seismic data with synthetic traces which were generated with the extracted wavelet. The well correlation is very crucial for seismic interpretation since it is the tie between the seismic and well data. The maximum coefficient of correlation for the Tajjal 02 is shown in Figure 5.3, which turned out to be 66%.

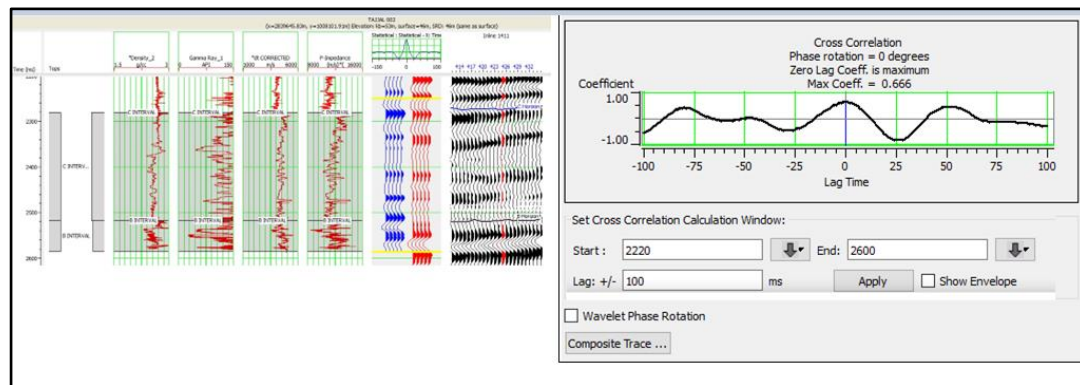


Figure 5.3 Correlation of seismic data with Tajjal-02 well.

5.4.5 Initial Low Frequency Model

The initial low frequency model is estimated using acoustic impedance. The acoustic impedance is divided into 2 types namely relative and absolute acoustic impedance (Sams and Carter, 2017). It is not necessary to create a low frequency model to calculate the relative acoustic impedance. Because of the relative qualities of the strata, it is favorable for qualitative interpretation of seismic sections (Li et al., 2013). Integration of low frequency model during seismic inversion improves the qualitative and quantitative interpretations levels of seismic inversion results. Well data Information is required to build low frequency

model. The qualitative and quantitative interpretation gets enhanced by integrating low frequency model during the seismic inversion (Kumar et al., 2016).

Increased resolution, conversion from an interface to a layer property, conversion to physical rock properties (impedances), removal of the wavelet, and reduced tuning are some of the well-known advantages of seismic inversion. All of these improve the seismic data's interpretability both quantitatively and qualitatively (Latimer et al., 2000).

The production of the absolute impedances requires the integration of an accurate low frequency model with band limited seismic data. For each property for which inversion is to be performed, low frequency models must be built (Sams and Carter, 2017). The properties vary depending on the inverted seismic data, but they are frequently some types of elastic property or a combination of elastic properties (Sams and Carter, 2017).

To aid in the construction of low-frequency models, the following key sources of low frequency data can be used: seismic velocity data and well-log data. There may be measurements for all the necessary elastic characteristics in well log data, which cover the entire frequency range from zero to well above the highest seismic frequencies (P-sonic, S-sonic, and density). A low frequency model is typically created by simply interpolating well data within a structural and stratigraphic framework (Sams and Carter, 2017). The Initial low frequency model must be added to the Model-based Inversion process.

By using density and sonic log in the vicinity of the well, the initial low frequency model is generated. The estimated initial model of low frequency with Tajjal-02 is displayed in Figure 5.4.

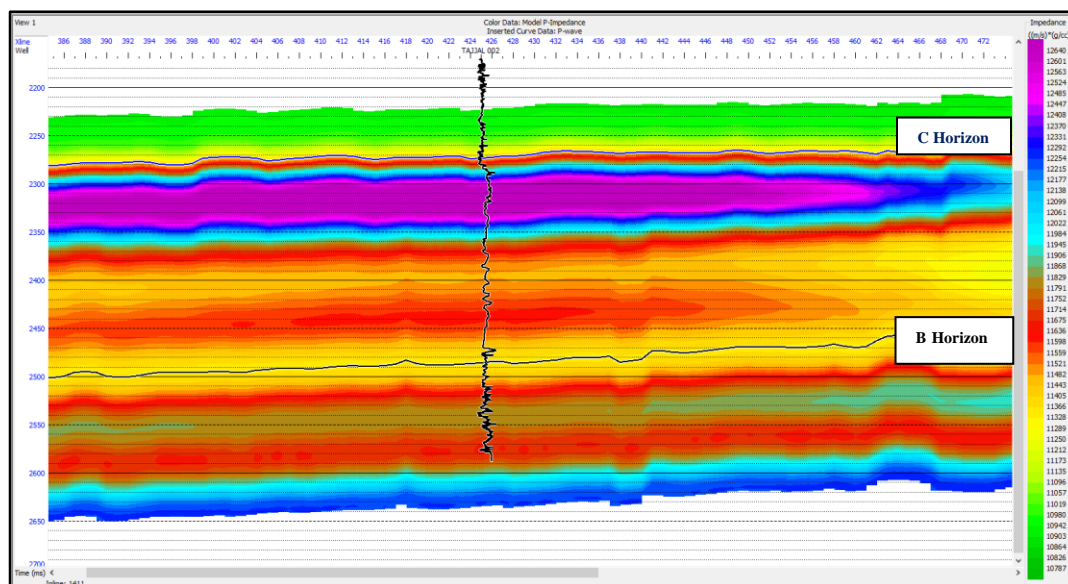


Figure 5.4 Low Frequency model with well location of Tajjal-02

5.4.6 Inversion Analysis

At the Tajjal 02 well site, the given seismic cube information was analyzed for model base inversion. The wavelet that was extracted from the time window was between 2200 to 2600 ms. The wavelet that was extracted seismically was adjusted by comparing the synthetic trace with the inverted trace at the well location. A good impedance model will be generated as a result of high correlation percentage. As seen in Figure 5.5 the black color represents the traces and synthetic traces are shown by red color. Tajjal-01 is having correlation coefficient of 99.76% with root mean square error between the seismic trace and synthetic is 7%.

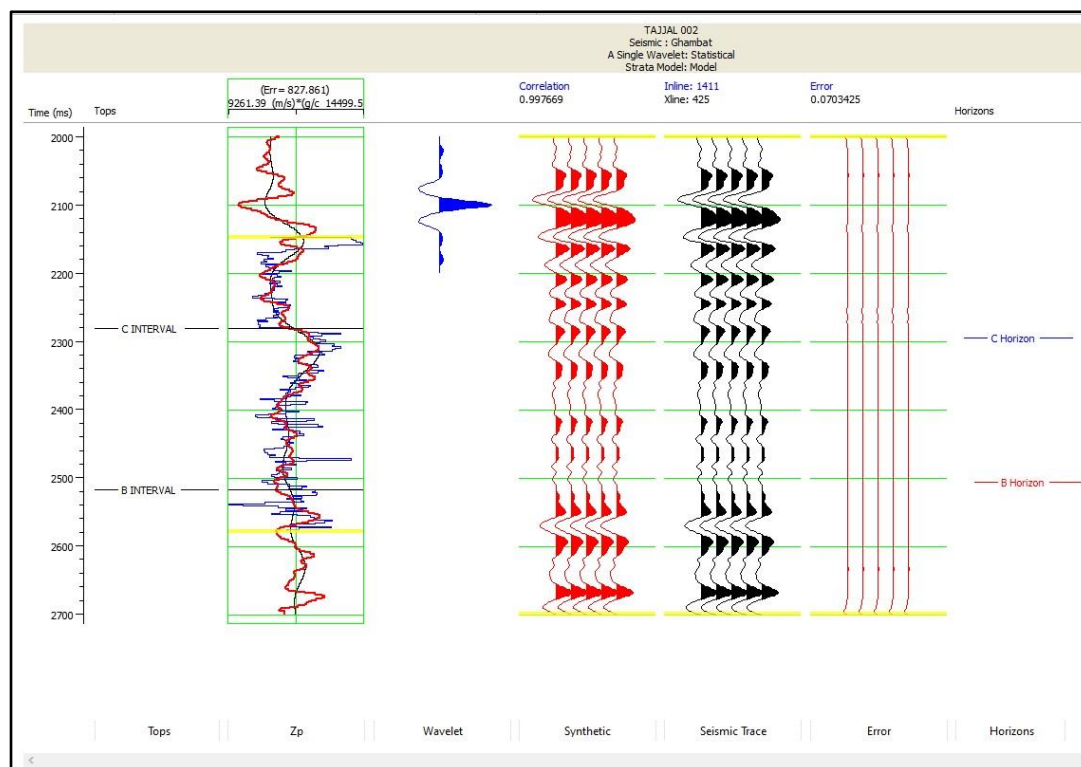


Figure 5.5 Model based inversion analysis of Tajjal- 02.

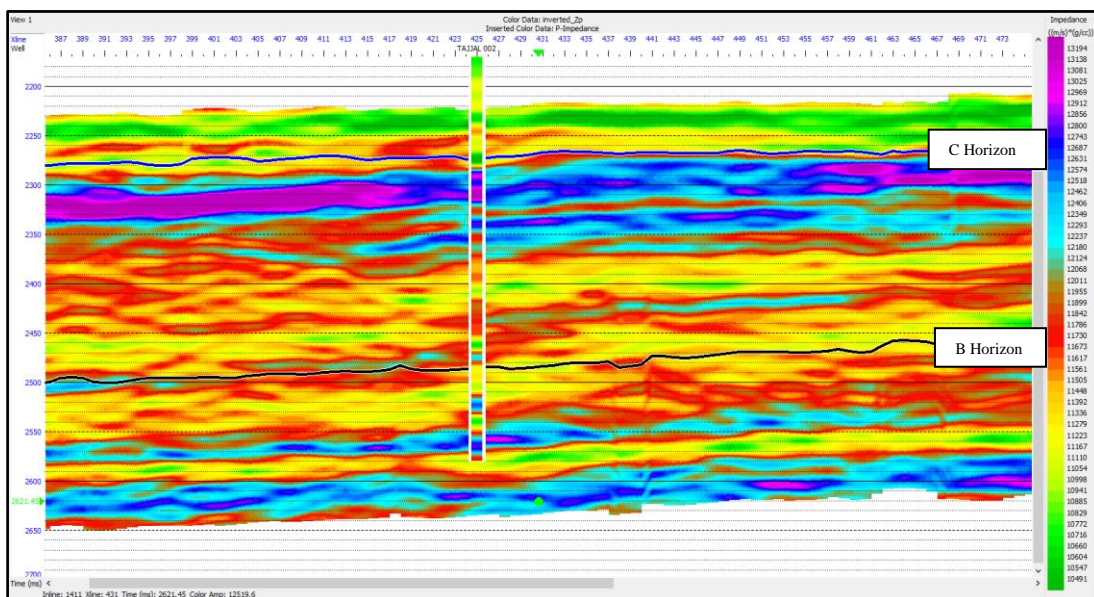
5.4.7 Results of Model Based Inversion

Physical properties of rock and fluids from seismic data are extracted by seismic inversion (Krebs et al., 2009). The mapping, interpretation, and quantification of hydrocarbon bearing zones have become less challenging by using seismic post stack inversion (Ali et al., 2018). The post stack inversion with zero offset converts seismic data (amplitude) into volume of acoustic impedance contrast by using geological data, seismic, well logs etc. (Downton et al., 2005).

Model-based inversion produces an acoustic impedance model that matches the entire frequency range of impedance by taking low frequency model and seismic data as inputs. The model-based inversion is more realistic and accurate, but an accurate initial model and computation is required for model-based inversion (Narayan et al., 2023). As can be seen in Figure 5.6 the impedance range lies between 10491 to 13194 $\text{g/cm}^3\text{-m/s}$. And the B and C intervals of Lower Goru Formation are marked by the impedance of approximately 11673

and $12687 \text{ g/cm}^3\text{-m/s}$ respectively. Considerably lower impedance values are encountered along both the horizons. The low impedance at both the B and C intervals indicates that these are reservoir zones and might be having gas situation.

Figure 5.6 Final Computed impedance model at Tajjal-02 Well location.



5.4.8 Slices

Slices were extracted for both the B and C intervals of Lower Goru Formation. Slices of both show the overall variation of P impedance. The C intervals impedance slice values lie between the impedances ranges of 11782 to $12196 \text{ g/cm}^3\text{-m/s}$ Along the Sand channel (C sand), a substantially lower impedance anomaly appears at the Tajjal 01 and Tajjal 02 locations which could be an indicator of hydrocarbons (gas) accumulation. It can be seen in the Figure 5.7, that relatively higher impedance values are observed on the extreme west, relatively lower values exist in the central portion and at the well location of Tajjal 01 and Tajjal 02 the low values of impedance give clue about hydrocarbons accumulation. Low impedance values range between 11782 to $11937 \text{ g/cm}^3\text{-m/s}$. Very low impedance values at the southernmost corner.

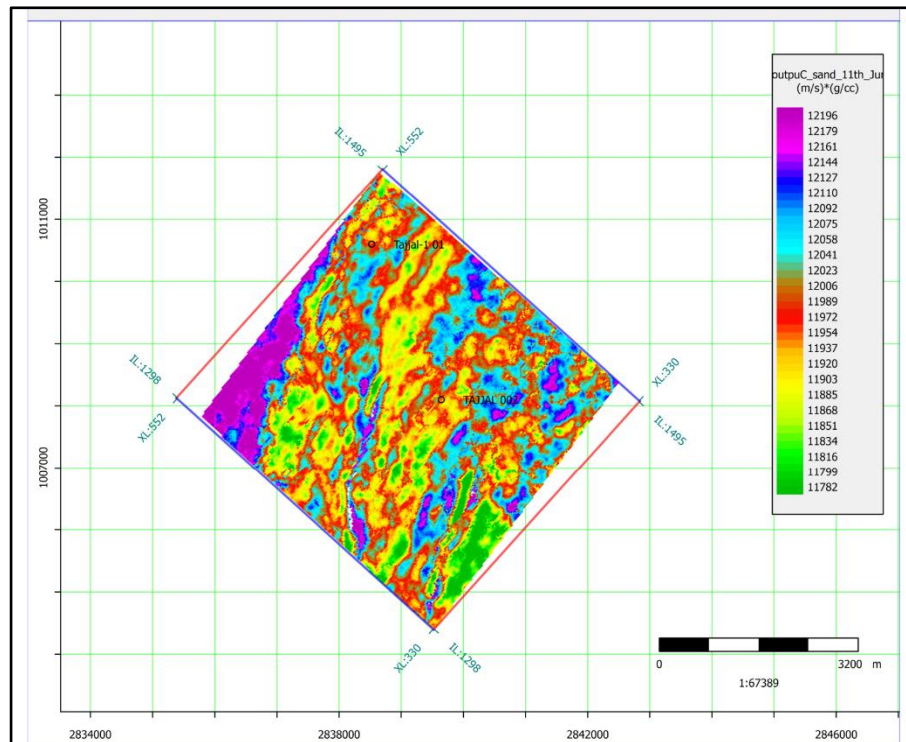


Figure 5.7 3D cube slice for C Interval showing variation for impedance.

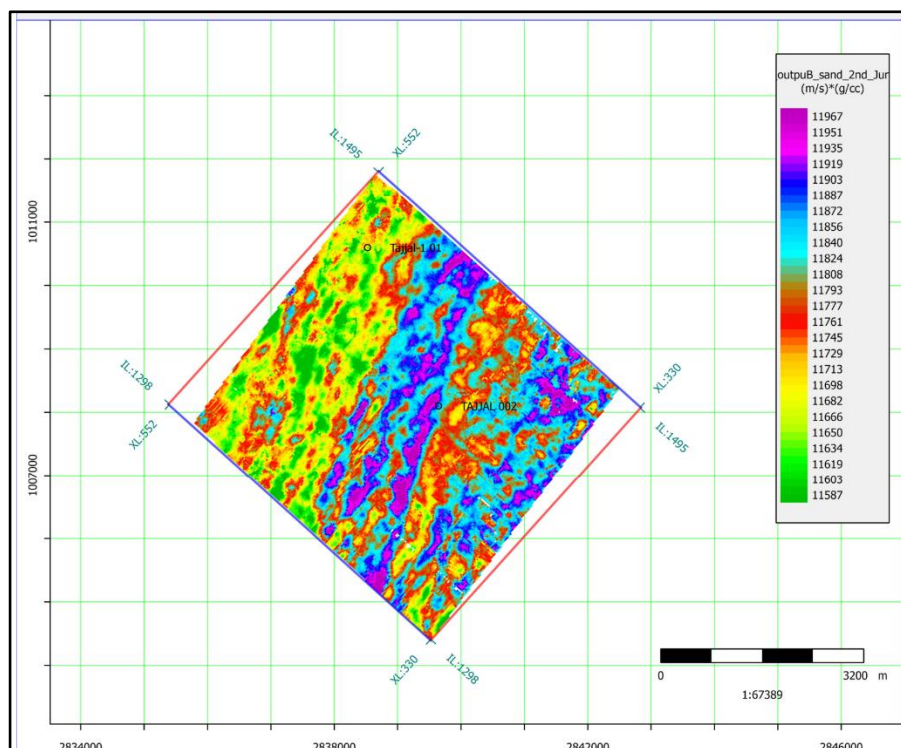


Figure 5.8 3D cube slice for B Interval showing variation for impedance.

The impedance slice of the B interval reveals variations in impedance, ranging from 11586 to 11968 $\text{g/cm}^3\text{-m/s}$. Lower impedance values are notably present in the north-western section, with some areas in the northeast and southeast showing higher impedance values. Low impedance value ranges from 11586 to 11714 $\text{g/cm}^3\text{-m/s}$. Along the B sand channel, a significantly lower impedance anomaly is observed at Tajjal 01. In contrast, the remaining areas in the cube exhibit higher impedance values.

5.5 Seismic Attributes

Seismic attributes have become the most widely used and reliable interpretation tools since their development in the early 1970s. Previously, they were only considered a tool for management display. However, now they are readily used for interpretation and this viewpoint has shifted (Taner et al., 1994).

Seismic attributes are described as the observation that aid in hydrocarbon exploration directly or indirectly and are extracted from seismic data. Attributes that can measure only one characteristic are known as “Primitive” attributes, or they can be merged using statistical, neural network, or known mathematical manipulation resulting in “Hybrid” attributes (Taner, 2001). Numerous attributes have developed from a range of computational methods after the advent of Complex Trace attributes in the 1970s (Chambers et al., 2002).

The most often used approach for transforming post stack seismic traces into a set of instantaneous seismic attributes that can be applied to create a range of geological interpretations is known as the Complex trace analysis. The fundamental data of a seismic trace is time, amplitude, frequency, and attenuation. Since attributes quantify specific data characteristics they are thus representative of the total information (Khan and Akhter, 2015).

Complex Seismic Trace Attributes have gained significant popularity since they were introduced in the early 1970s. At first, they were used as an appropriate format for visualization, but as they were combined with other measurements which were derived seismically, they became a reliable analytical means for lithology prediction and for characterizing the reservoir (Taner, 2001).

Seismic attribute analysis and interpretation provide us with qualitative information about the geometrical and physical properties of the earth. The amplitude content of seismic data is the most important part in determining parameters such as velocities, absorption, reflection coefficients, acoustic impedance (Taner, 2001).

5.5.1 Classification of Attributes

The classification of attributes is as follows:

One can compute attributes either from pre stack data or post stack data i.e., before migration or after migration.

- **Pre-Stack Attributes**

In the case of Pre-Stack Attributes CDP or image gather traces are used as input data. This input dataset will have information related to offset along with direction (azimuth information). These computations create massive volumes of data thus making them impractical for preliminary research. Although they contain a significant amount of information that is directly related to orientation of fracture and fluid content (Taner et al., 2001).

- **Post-Stack Attributes**

Removal of offset and azimuth information is done by an averaging process called stacking. The input data for post-stack attributes is CDP stacked or migrated. The post stack attributes are more convenient for monitoring enormous volumes of data in early reconnaissance studies. However, in-depth studies should be done by using pre stack attributes (Taner et al., 2001).

The seismic attributes can be further categorized based on their computational properties.

- **Instantaneous Attributes**

The computation of instantaneous attributes occurs on a sample-by-sample basis and these attributes indicate instantaneous variations of several parameters (White, 1992). From complex traces, the instantaneous values of attributes such as envelope, its derivatives, frequency, and phase can be calculated. The interpretative significance of the fundamental instantaneous attributes has been analyzed by (Robert and Nogami, 1984).

- **Wavelet Attributes**

These consist of such instantaneous attributes which are computed at trace envelope's peak. These attributes exhibit an absolute link with the Fourier transform of the wavelet in proximity to the envelope's peak. These attributes can be subdivided based on their relationship with geology (Taner et al., 2001).

- **Physical Attributes**

The physical attributes related to the physical quantities and physical qualities. The trace envelope's magnitude exhibits a direct relationship with the contrast in the acoustic impedance. Frequencies, on the other hand, are associated with bed thickness, wave

scattering and absorption. The average and instantaneous velocities are directly associated with the properties of rock. These attributes are thus primarily used for reservoir characterization as well as lithological classification (Taner et al., 2001).

- **Geometrical Attributes**

Geometrical attributes are used for describing the relationship among attributes in terms of temporal and spatial relationships. Since geometrical attributes specify the event characteristics and their spatial relationships thus they can be used for stratigraphic interpretation (Taner et al., 2001).

However, during this research attributes are applied for thin bed identification. For this purpose, number of attributes were applied but three attributes gave reliable results and are discussed as follows:

5.6 Attribute analysis of the study area

For thin bed identification three attributes namely spectral decomposition, instantaneous phase and trace envelope were applied.

5.6.1 Spectral Decomposition

Through the use of mathematical techniques like the Discrete Fourier Transform(DFT), continuous Wavelet Transform (CWT) and others, spectral decomposition transforms seismic data into frequency domain (Othman et al., 2016). For seismic interpretation, spectral decomposition has proven to be a reliable method and it is also applied to map temporal bed thickness. Spectral decomposition can also help in delineating hydrocarbon distribution and for indicating stratigraphic traps (Castagna et al., 2003).

When seismic data showed variations in response at different frequencies i.e., at higher frequency, shorter wavelength, thin channels were detected, this technique was developed. Since seismic data is spectrally whitened during processing, this spectral

component contains geological information with varied channel thickness and infills thus generating different responses at different frequencies (Koson et al., 2014). Spectral decomposition can be used to map and image the thickness of bed, deviation of channels, geological discontinuities along with considering DHI (Othman et al., 2016).

The spectral decomposition attribute was applied on seismic line 1419. It was found that the frequency band width present in this data lies between 5 to 70 Hz. It can also be demonstrated from Figure 5.8 that amplitude stability lies within the range of 0.6 to 1.

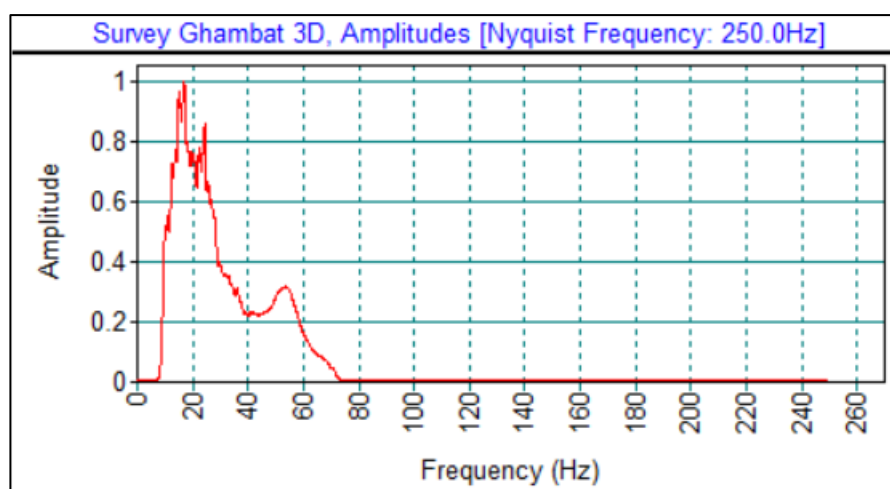


Figure 5.9 Amplitude and frequency spectra for seismic inline 1419.

This attribute is most effective in resolving thin bed sand layers. Lower frequencies are better in resolving thicker beds, while thin beds are better resolved by higher frequencies. Since the study area has thin sand packages, this attribute is most suitable to resolve the thin sand packages of Lower Goru Formation. This attribute was applied to seismic line 1491. The seismic section of line 1491 was displayed at different frequencies to study the response at each specific frequency. It was observed that thinner sand beds of Lower Goru B and C sand in the Tajjal 02 well became visible as the frequencies increased step by step. The circle is highlighting the fault which was relatively difficult to interpret on normal seismic section shown in Figure 5.14.

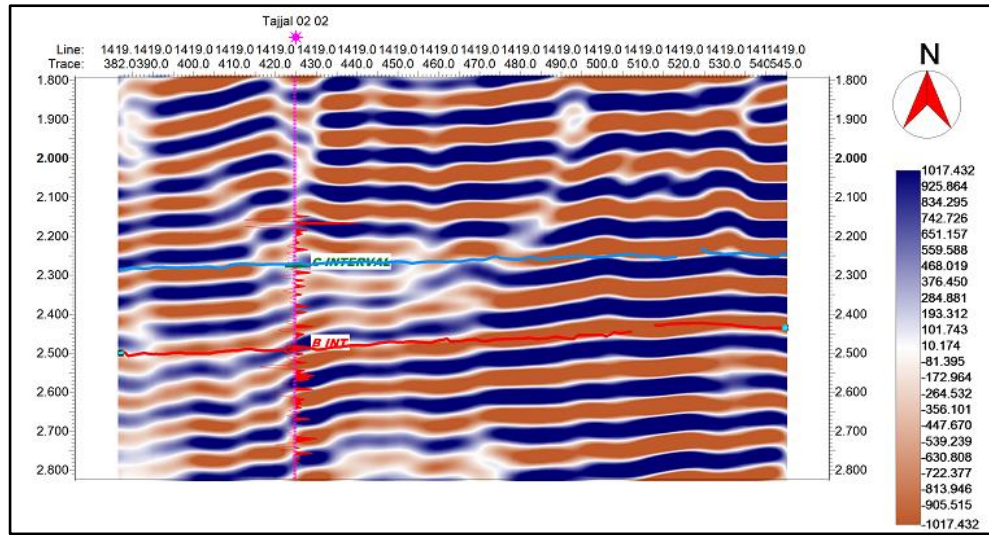


Figure 5.10 Spectral Decomposition attribute of seismic line 1419 at 9 Hz frequency

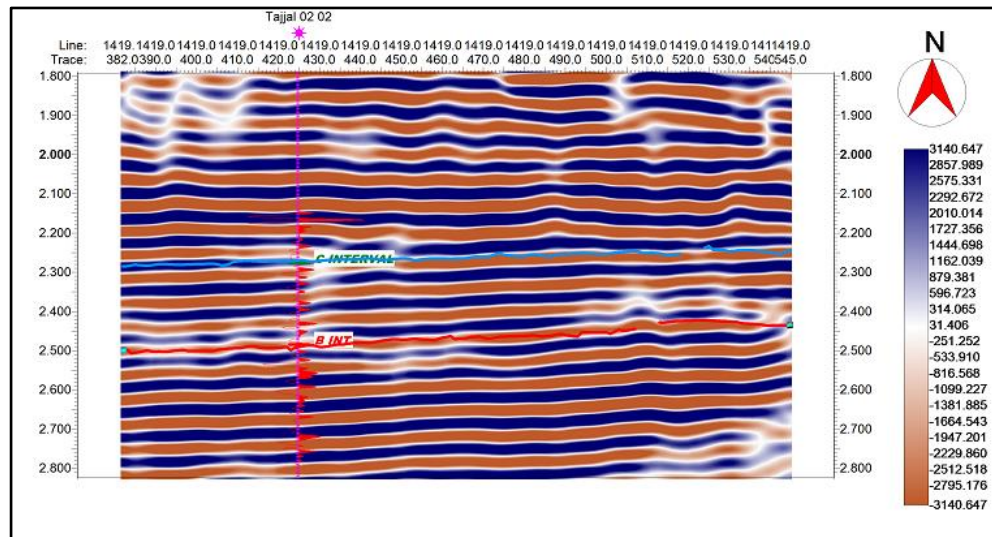


Figure 5.11 Spectral Decomposition attribute of seismic line 1419 at 14 Hz frequency

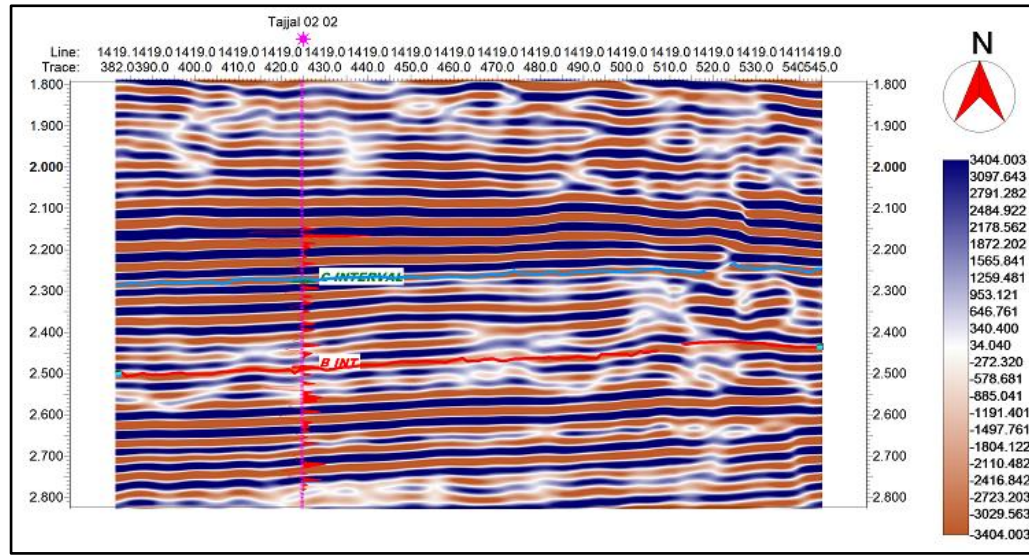


Figure 5.12. Spectral Decomposition attribute of seismic line 1419 at 21 Hz frequency

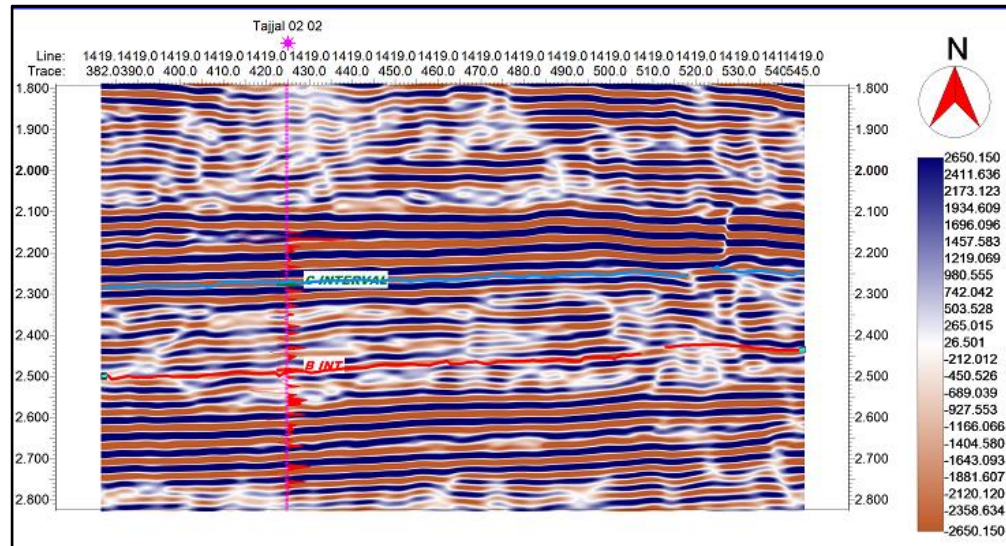


Figure 5.13 Spectral Decomposition attribute of seismic line 1419 at 29 Hz frequency

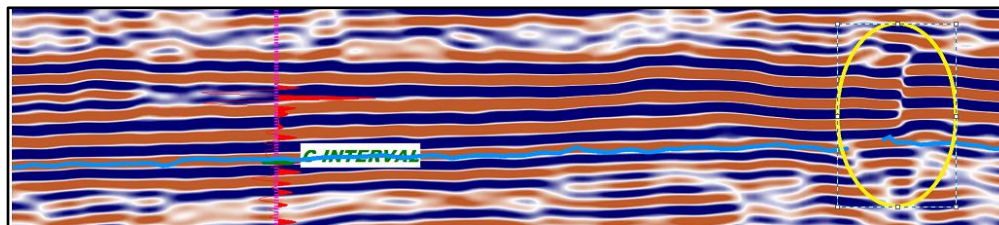


Fig 5.14 Circles highlighting fault that was difficult to interpret on normal seismic section.

- **Results and discussions**

By using the spectral decomposition attribute the seismic data is resolved into individual frequency components which lie within the seismic bandwidth, allowing the same underlying geology to be seen at different frequencies (Naseer et al., 2017). The spectral decomposition attribute which is useful for resolving the thin beds was applied on seismic line 1419 at different frequencies. The procedure begun by applying this attribute with 9 Hz frequency. At this frequency the thin beds were not identified. After that the frequency was slightly increased and the attribute was applied at 14 Hz frequency, at this frequency the beds were not completely resolved but they were better indicated by 14 Hz as compared to 9 Hz. After that the frequency was increased to 21 Hz, at this frequency the spectral decomposition attribute resolved the thin beds quite accurately and a fault also begun to appear which was not resolved at previous frequencies. This fault was also marked while performing seismic interpretation shown in Figure 5.4.

Lastly, the attribute was applied at 29 Hz, at this frequency the thin beds were completely resolved, and the presence of fault was also confirmed which was relatively difficult to mark on normal seismic section Thicker beds or features are tuned and have greater amplitude at lower frequencies whereas thin beds are tuned and have higher amplitude at higher frequencies (Naseer et al., 2017). After applying spectral decomposition attribute on various frequencies, it was observed that thinner sand beds of Lower Goru B and C sand in the Tajjal 02 well became visible as the frequencies increased step by step. The beds were best resolved by frequency of 29 Hz.

5.6.2 Instantaneous Phase

Wave fronts are defined as lines of constant phase, hence the phase attribute, which is also a physical property, can be utilized as a discriminator for classification of geometrical shapes. Instantaneous phase, which refers to the phase component of wave propagation and lacks amplitude information, is the best marker for lateral continuity because it represents all the events (Taner et al., 2001).

The instantaneous phase is a reliable indicator of lateral continuity, it can also aid in computing the phase velocity. Since there is no information of amplitude in the instantaneous phase thus all the events are represented. The stratigraphic elements can be seen in detail using the instantaneous phase (Taner et al., 2001).

The instantaneous phase provides information about seismic trace without amplitude contrast because it lacks information about amplitudes (Barnes, 2007). The instantaneous phase attribute is also very useful for identifying bed geometries in reservoir weak zones. This attribute along with other attributes can be utilized as hydrocarbon indicator because hydrocarbons are linked to phase transition events (Chen and Sidney, 1997).

The instantaneous phase values are related to the apparent position of cosinusoids i.e., the peak of the seismic trace represents 0° , the trough has maximum phase, downward zero crossings have a phase of 90° , and upward zero crossing have a phase of -90° (Barnes, 2007). Figure 6.5 shows the instantaneous phase attribute which changes from -105° to $+105^\circ$. The interpreted horizons lie over the maximum phase regions indicated by violet color.

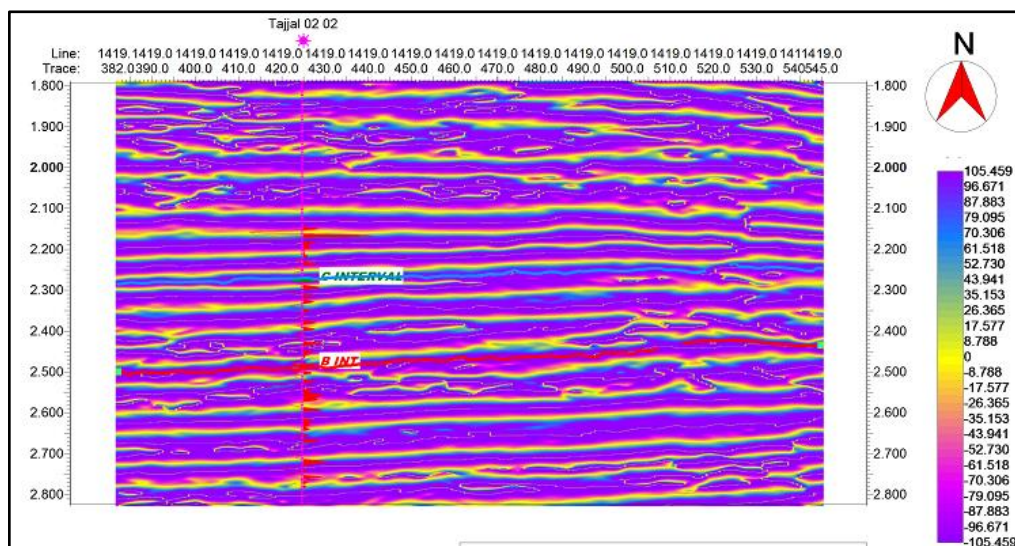


Figure 5.15 instantaneous phase attribute calculated for seismic line 1419.

5.6.3 Trace envelope

The trace envelope attribute is also called reflection strength and instantaneous energy. The trace envelope or reflection strength reveals zones of strong acoustic events (bright) on both positive and negative events, this attribute represents the signals instantaneous energy and is proportional in magnitude to the reflection coefficient (Koson et al., 2014). This attribute is useful when examining amplitude packages. This attribute is extremely beneficial to seismic interpreters since it does not employ original seismic trace values that are dependent on the phase or polarity of seismic data, both of which change the apparent brightness of a reflection (Koson et al., 2014). Because of the acoustic impedance contrast, the bright spot provides information about sandy lithology and channel bodies (Koson et al., 2014). This attribute contains information regarding lithology change, bright spots, and thin bed tuning effects. Instantaneous attributes are calculated at any point in seismic segment and are independent of any interpretation (Radovich and Oliveros, 1998).

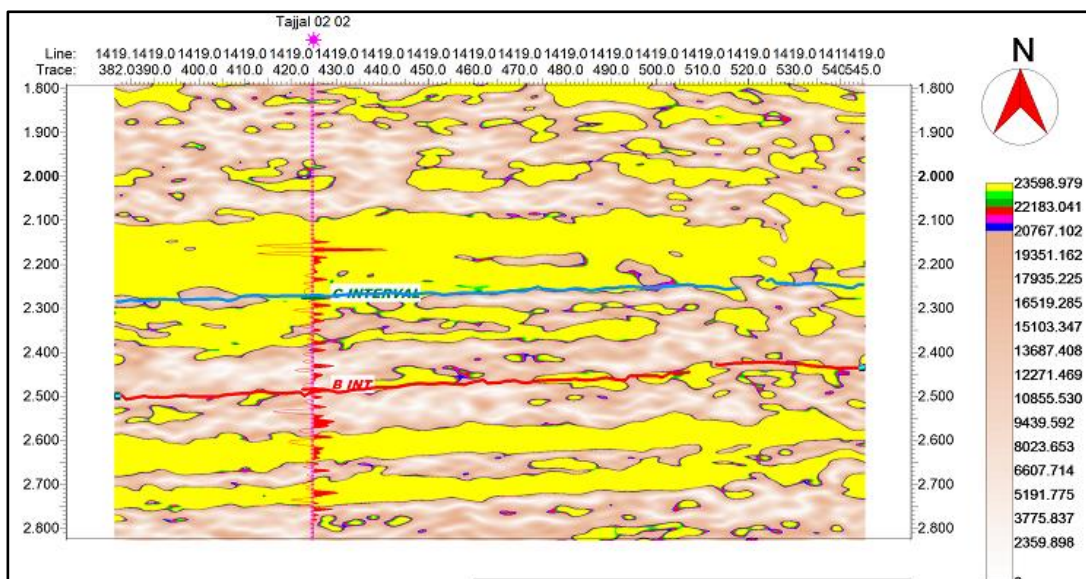


Figure 5.16 Instantaneous Amplitude (Trace envelope) applied on seismic line 1419.

The envelope of a trace, also known as the reflection strength, is a measure of complex trace's total instantaneous energy that is independent of phase. The envelope is directly related to the contrast in acoustic impedance. According to the bandwidth of seismic, it may indicate the individual interface contrast or more commonly the combined response of numerous interfaces (Koson et al., 2014).

This trace envelope attribute is computed for seismic line 1419. The thick (yellow) package indicates maximum reflection strength. This attribute also highlights the presence of sandy bodies (Koson et al., 2014). The results of trace envelope attribute suggests that high energy area i.e., C interval of Lower Goru Formation could be having presence of hydrocarbons. The results of petrophysical analysis also reveal that C interval is hydrocarbon bearing.

Because of the acoustic impedance contrast, bright spots reveal information about channel bodies or sandy lithology, it provides information on lithology variation, thin bed tuning effects, bright spots (gas presence) etc. When playing with direct hydrocarbon indicators, the interpreter should be quite careful because bright spots are not necessarily associated with zones that are hydrocarbon bearing (Brown, 2001).

CHAPTER 06

COMPUTATION AND VALIDATION OF SHEER SONIC USING MACHINE LEARNING AND FACIES ANALYSIS

6.1 Introduction

Significant challenges confronting our society necessitate solutions to geophysical problems such as anticipating the effects of climate change and measuring air pollution, forecasting infrastructure risks by natural calamities such as hurricanes, and forecasting future availability and the use of water food, and mineral resources along with determining the causes of earthquake, landslides, and other natural disasters such as volcanoes and floods. As the influx of big data continues to impact virtually every commercial and scientific field, geosciences have also undergone a fundamental transformation from a data poor to a data rich field (Karpatne et al., 2018).

As a result, there is a significant opportunity for machine learning researchers to work closely with geoscientists and merge ideas across disciplines to advance the frontiers of machine learning as well as geosciences (Karpatne et al., 2018). Machine Learning(ML) has appeared as a revolutionary development in geosciences with the arrival of computer science algorithms because of its ability for highlighting relationships for the purpose of predicting the needed output (Gupta et al., 2021).

The availability of sheer Sonic log(DT) is essential for lithology and fluid discrimination within the reservoirs. However, within the Lower Indus Basin there are only limited wells that have the availability of shear Sonic log. This is where Machine Learning

plays its part. With fewer input data sets, machine learning has lately become a reliable and optimized method for forecasting the exact shear Sonic log(DTS)(Ahmed et al., 2022).

The interpretation of elastic properties' interpretation including Sonic(DTP), DTS, and density(RHOB), is critical because they are significantly related to reservoirs properties which are measured by seismic (Munyithya et al., 2019). DTS can help in identifying litho-fluid types and distinguishing between wet and gas sands when combined with Vp/Vs ratio, the $\lambda\rho$ and $\mu\rho$ relationship is used to enhance fluid and lithology deviation, which also give clue of the gas sand zone and is greatly reliant on accurate shear sonic (Young and Tatham, 2007).

Since Machine Learning has proved to be quite reliable for predicting the shear sonic log this research used the same approach for prediction of the shear sonic log along with confirming reliability of machine learning calculated shear sonic by applying it to pinpoint the AVO anomaly. The procedure is mentioned in the workflow below. Along with machine learning based facies analysis.

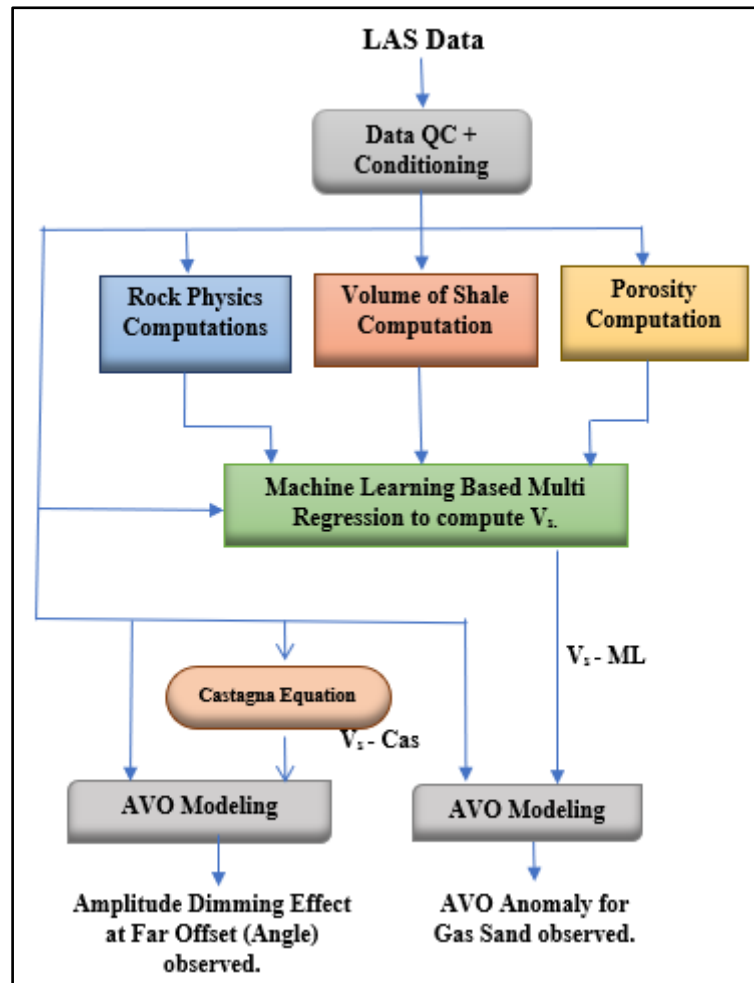


Figure 6.1 Workflow adopted for computation of shear sonic computed by ML and it's validation by mapping AVO anomaly.

Number of steps were adopted during the workflow their detail is as follows:

6.2 Data Review

Initially Las data was loaded and after that it was viewed for quality control and initial conditioning was performed to refine the data which involved deglitching, trimming etc.

The first step consists of reviewing the data as well as editing and conditioning. The well Tajjal-03 was selected, and the depth intervals selected for analysis are 3300 to 3800 m.

Both B and C intervals of Lower Goru Formation are lying within these depth intervals. After conditioning the final logs that would be used for computation purposes are shown in Figure 6.2.

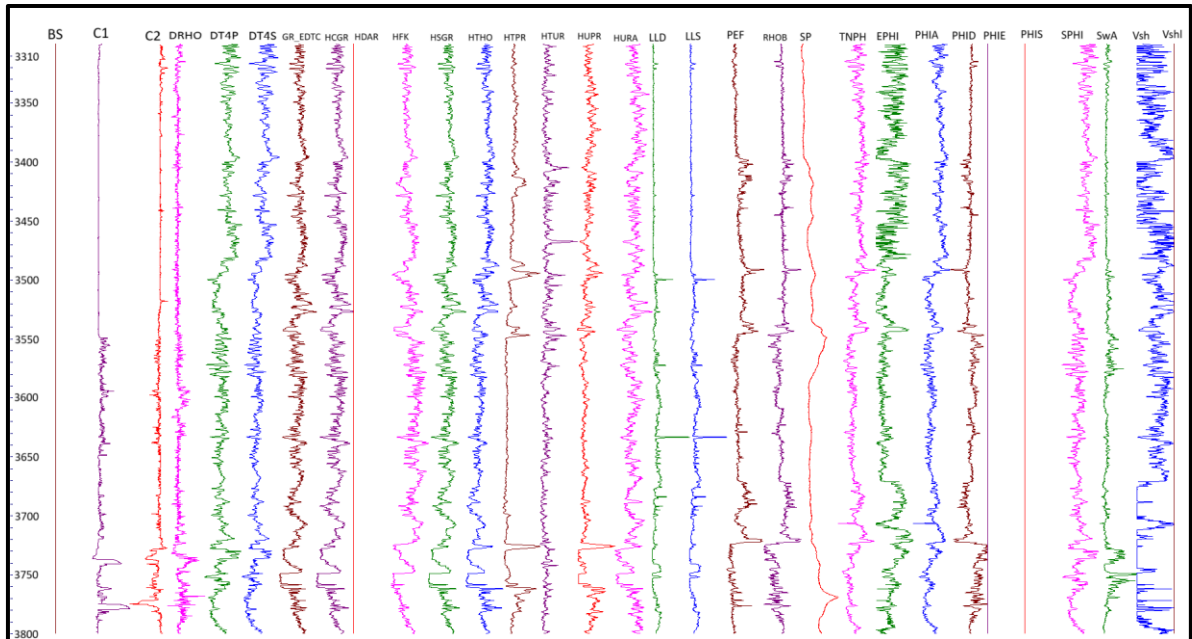


Figure 6.2 Initial Input Data set for C and B interval ranging from 3300-3800 m in Tadjal-03.

After initial conditioning from the refined data three parameters were computed

- Rock Physics computation: Bulk shear modulus etc.
- Volume of shale calculation
- Porosity computation

6.3 Rock Physics Computation

The physical qualities of a reservoir rock, such as porosity, rigidity, and compressibility, are described by rock physics. These properties determine what would be the response of seismic waves while travelling through the rocks. The calculation of various elastic moduli such as bulk, shear etc. falls in the domain of rock physics (Dewar et al., 2001).

In linking elastic parameters such as impedances and velocities to reservoir properties including fluids, porosity, lithologies rock physics plays a vital role (Bosch et al., 2010).

Before using neural network, all rock physics parameters were computed which include various elastic moduli including bulk modulus, shear modulus, young modulus, p wave modulus, Lamé constant etc. as shown in Figure 6.3.

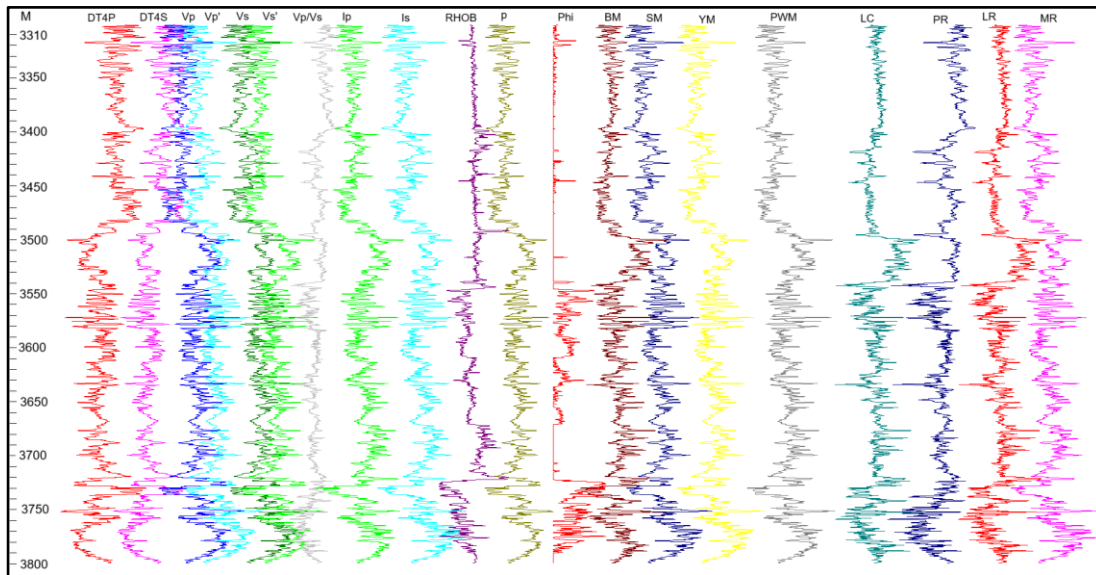


Figure 6.3 Rock Physics Properties computed including various moduli for C and B interval ranging from 3310-3800 m in Tadjal-03.

6.4 Calculation of shale volume

Gamma ray log is used for calculating the volume of shale. This calculated volume of shale was then fed to the machine learning based regression to compute the shear wave.

6.5 Porosity Computation

After calculating the shale volume, the next step was to compute the porosity. The porosity was computed using neutron log and sonic log.

All these (initial logs, rock physics computation, volume of shale calculation, porosity computation) were then fed into machine learning regression-based analysis. After grouping them in different classes it computes different regression for them. Within this neural network sort, the data based on volume of shale, porosity and other parameters and divides them in different classes in my case it divided into three packages/classes:

- Pure clean sand.
- Tight sand.
- Shale.

After grouping them in different classes it computes different regression for them.

6.6 Multi regression

Multi regression is one of the statistical techniques used for studying the link among a single independent variable and various other variables which are independent. The purpose of multiple regression analysis is the usage of known independent variables for predicting the value dependent single variable (Moore et al., 2006).

Neural network sorted the data based on volume of shale, porosity and other parameters divided in different classes i.e., pure clean sand, tight sand, and shale. After grouping them in different classes it computes different regression for them. Wireline log data of 5 to 6 wells in the surrounding of study area were used for training the model.

Since unlike North (Upper Indus Basin) where thick lithology is present my study area lies in Lower Indus Basin where there are thin sand/shale packages so manually it is very difficult to separate these packages and thus machine learning has been used to identify each of these packages and then to sort them out in different classes and lastly to apply regression analysis to compute their respective shear wave equations i.e., V_p to V_s computation equations.

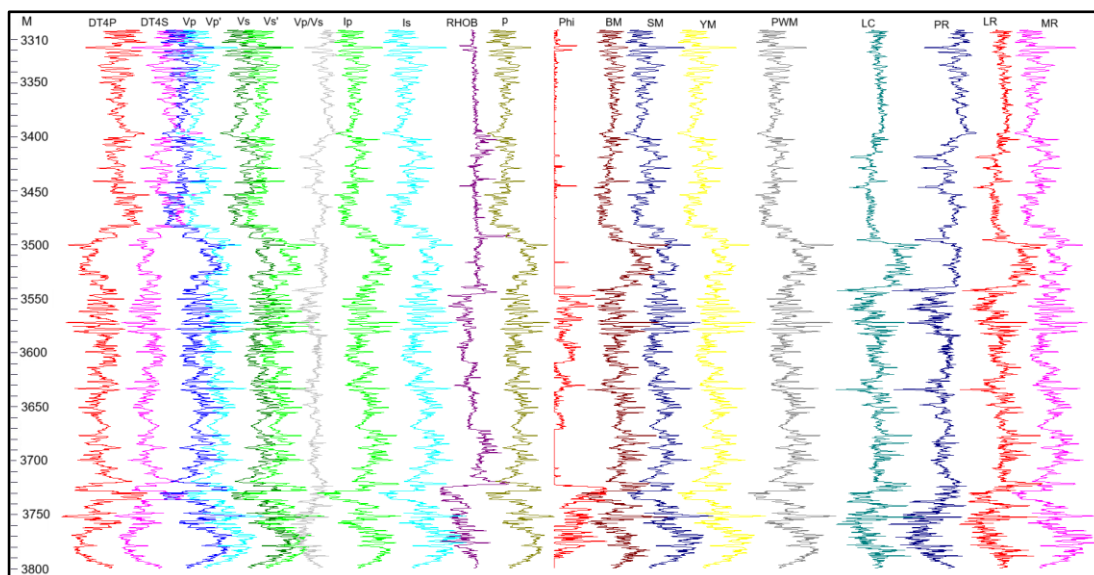


Figure 6.4 Multi Regression-ML applied on depth intervals ranging from 3310-3800 m for C and B intervals of Tajjal-03.

Here, as we can see in Figure 6.4, V_p is displayed by blue color in first track and V_s is displayed in second track by green color. As seen in Figure 6.4 and cross plots machine learning has identified three packages. Sand, shale, and tight sand. Wherever sand is present is has been highlighted by green color, tight sand by pink and shale has been highlighted by yellow color.

ML along with identifying the sand, shale and tight sand has also computed different equations for each lithological package. And the respective equations for each package are also displayed in the Figure 6.4

Table 6.1 Multi regression Equations

Lithology	Respective Equation
Sand	$V_s = -542.838 + 0.71596 V_p$
Tight sand	$V_s = 1118.698 + 0.39619 V_p$
Shale	$V_s = -544.535 + 0.70486 V_p$

This separation based on the classes is behind the scenes done by using input data which includes gamma ray log, porosity, different moduli, and porosity and all these are fed to the neural network and then it is separating the packages. And the packages are divided into three groups/classes including sand, shale, and tight sand.

Later on, if multi regression is applied to a well where the shear sonic is not present then it will automatically apply equation according to the package. For clean sand a different equation would be used, for tight sand another and for shale packages the equation would be different. However, in my case I am applying regression analysis to the well where shear sonic is already present.

6.7 Comparison of Vs computed from Castagna, and Vs computed by ML.

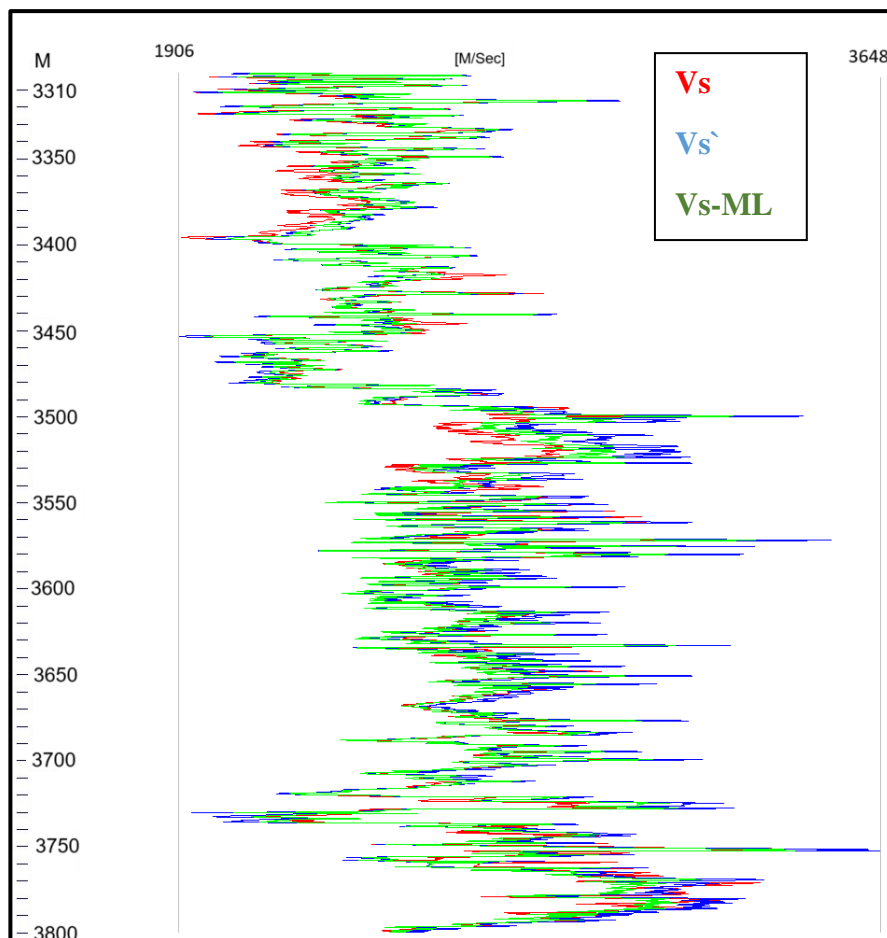


Figure 6.5 Comparison of Vs (Vs provided), Vs' (Vs-Castagna), Vs-ML (Vs computed by ML) for C and B interval.

Figure 6.5 shows the comparison of shear sonic which was already given in well data, shear sonic computed by Castagna, and shear sonic computed by ML.

The legend shows that Vs is displayed by red color, which was already provided, Vs' is computed from Castagna and Vs-ML represented by green color is Vs computed by ML. As it can be seen from the Figure 6.5 that the red and green i.e., Vs already present and Vs computed by ML are overlapping at most of the places however, blue i.e., Vs computed by Castagna is quite outside the range which brings us to the conclusion that that shear sonic computed from Castagna is not reliable and hence cannot be used for advanced purposes such as AVO.

6.8 AVO Modeling

The AVO (amplitude variation with offset) also known as amplitude variation with angle (AVA) technique, evaluates changes in seismic reflection amplitude as the distance between shot location and receiver changes. Geophysicists can use AVO analysis to better estimate the reservoir rock properties such as the content of fluids, porosity, density, and lithology (Feng et al., 2006).

The AVO method is a very effective method for characterization of reservoirs. The success of AVO analysis depends not only on the level of quality of the seismic data that was acquired but it also depends upon data processing and knowledge of physical characteristics of the rock (Li et al., 2003).

During my research work I used two approaches to calculate the shear wave velocity. Wireline log data of 5 to 6 wells in the surrounding of study area were used for training the model. The first approach was to use the Castagna equation to calculate the Vs and the second approach made use of Machine Learning for computing the Vs. After computing the Vs from both approaches their validity was checked by AVA modelling. AVA modelling was performed by using Vs computed from both approaches and it was observed that upon performing AVA by using Castagna equation no AVA anomaly is observed however, gas sands were observed from shear sonic computed by multi regression.

6.8.1 AVO modeling using shear sonic computed by Castagna Equation

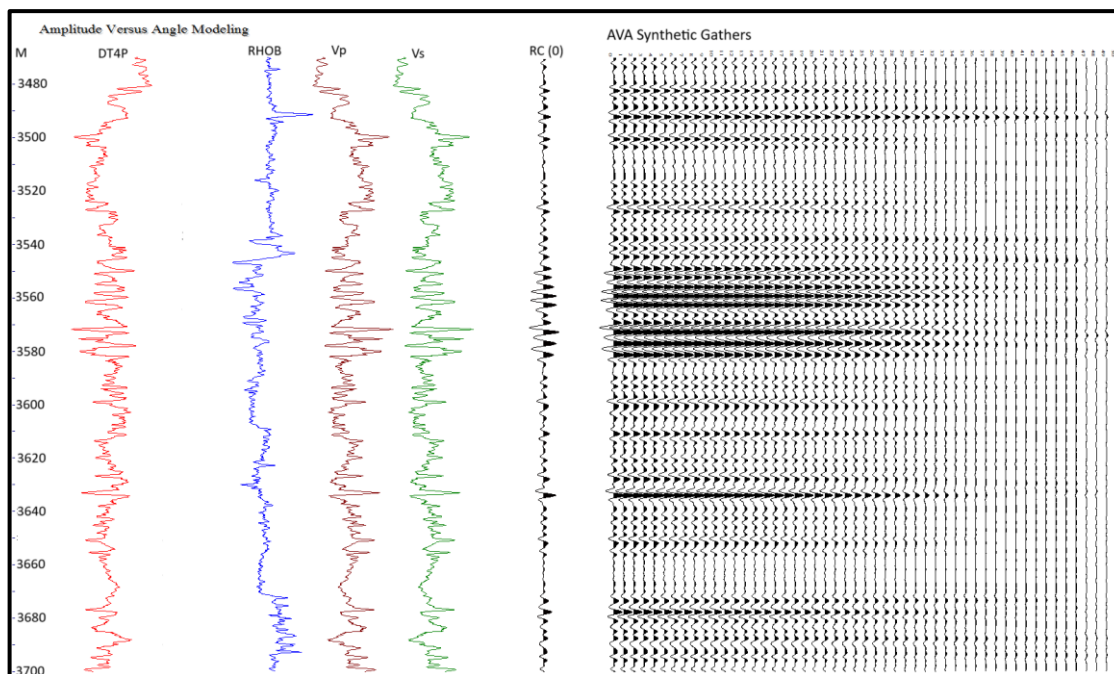


Figure 6.6 AVO modeling using shear sonic computed by Castagna Equation for C and B intervals of Tajjal-03.

Explanation:

On the left most side depth intervals are displayed and in the first track Vp is displayed, Rhob is displayed in second track and although shear sonic is not given here it is automatically built in the software and the software will automatically compute it by Castagna equation.

As we can see in Figure 6.6 if we perform AVA by using Castagna equation then dimming effect is observed. And no AVO anomaly is observed which brings us to the conclusion that if shear sonic is missing and we compute it by Castagna then it is not reliable and no AVO anomaly is observed and there is amplitude dimming effect at far offsets as shown in Figure 6.6.

6.8.2 AVO modeling using shear sonic computed by ML

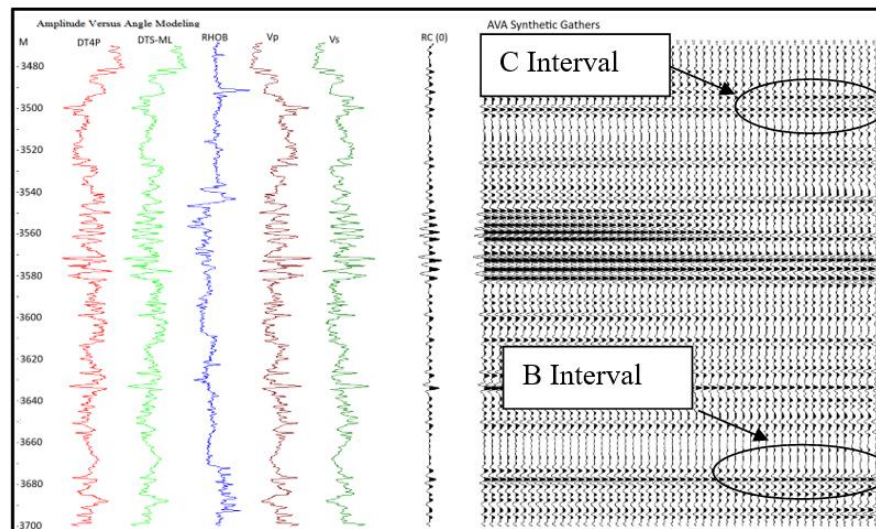


Figure 6.7 AVO modeling using shear sonic computed by ML for C and B intervals of Tajjal-03.

Explanation:

On the left most side depth intervals are displayed and in the first track Vp is displayed, Rhob is displayed in second track and shear sonic computed in this case is computed by Machine Learning. After computing the shear sonic from ML AVO is performed and gas sands are observed in this case as shown in (Figure 6.7).

6.8.3 Validation of shear sonic computed from multi regression

Gas Sands were observed from shear sonic computed by multi regression which brings us to the conclusion that in any well if shear sonic is not available then we can use this technique to compute shear sonic by ML by switching between different equations and then AVO effect would be visible.

Significance of AVO modelling

By using AVO gas sands were observed facilitating in interpretation. AVO modelling proves validity of shear sonic computed from multi regression. And shear sonic computed from Castagna is not useful.

6.9 Facies Analysis

Facies are defined as a formation's part that contrasts in its features regarding lithology from other rock bodies. Facies analysis is a key sedimentological tool for characterizing bodies of rocks that have distinct physical, biological, and lithological properties in comparison to all adjacent deposits (Imamverdiyev et al., 2019). Facies recognition using well log is a useful tool for analyzing an area's depositional setting. Well logs include a wealth of information regarding sediments and sedimentary processes. The gamma ray log is employed in petrophysical analysis for the purpose of identifying shale (Yemets et al., 2021).

Facies modeling is crucial for reducing uncertainty in drilling operation as well as for analyzing hydrocarbon reservoirs (Wang et al., 2017). One of the most crucial pieces of information for reservoir modeling is facies modeling. Well logs can be used for recognizing the number of facies, provide a description of the facies , reservoir lithotypes, and the correlation of facies between wells in facies classification study (Yemets et al., 2021).

The conventional wireline data used in facies modeling includes neutron porosity(NPHI), compression Sonic(DT), density(RHOB), etc. These methods for modeling the reservoir facies have been applied in several investigations. Numeral studies on facies models and the influence of facies determination on reservoir development have been done worldwide (Abdolahi et al., 2022).

6.9.1 Cross plots between Vp and Vs

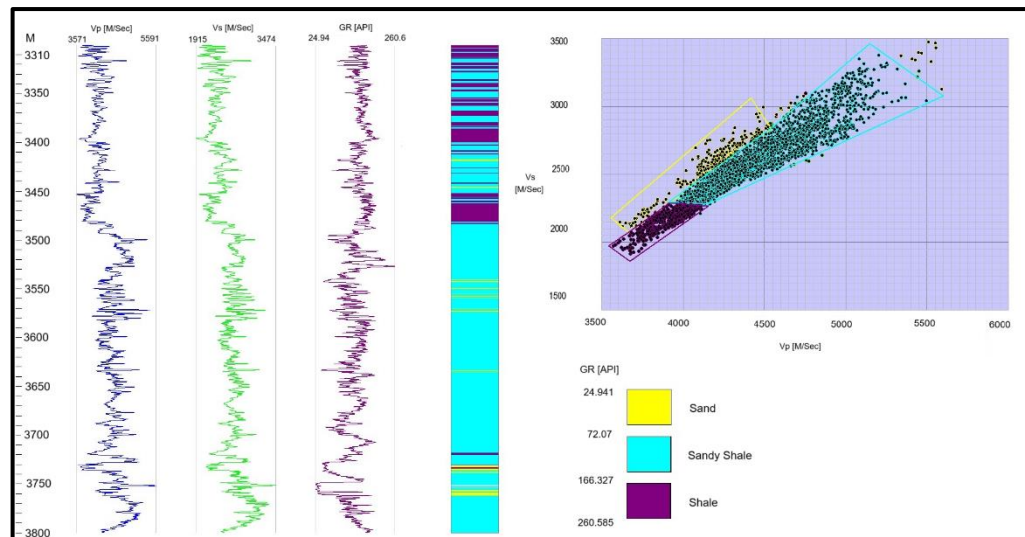


Figure 6.8 Cross plots between V_p and V_s of C and B intervals in depth interval ranging from 3310 to 3800 m of Tajjal-03.

Explanation:

Cross plots between V_p and V_s were computed. Gamma ray is used as a benchmark for color coding between sand and shale. And for color variation between sand and shale. As seen in Figure 6.8, three distinct packages are plotted namely sand, shale, and sandy shale. The gamma ray values for sand lie between 24.941-72.09, sandy shale depicted by cyan color lie between 72.07-166.327, and shale depicted by purple color lie between 166.327-260.585. This separation between three facies on the basis of gamma ray is behind the scenes done by neural networks automatically. The neural network scans the trend of data and then classifies it into distinct facies. Lower values of gamma ray correspond to clean lithology i.e., sand, and higher values of gamma ray are indicative of shale and in between the sand and shale, sandy shale lies at an intermediate gamma ray value.

After the construction of cross plots between V_p and V_s polygons are constructed. Polygons are drawn around clusters of data points as shown in the cross plot which help in marking the boundaries of the three lithologies i.e., sand, sandy shale, and shale. These

polygons are quite useful since they help identify various facies and the transition between them.

6.9.2 Cross plots between Vp and Density

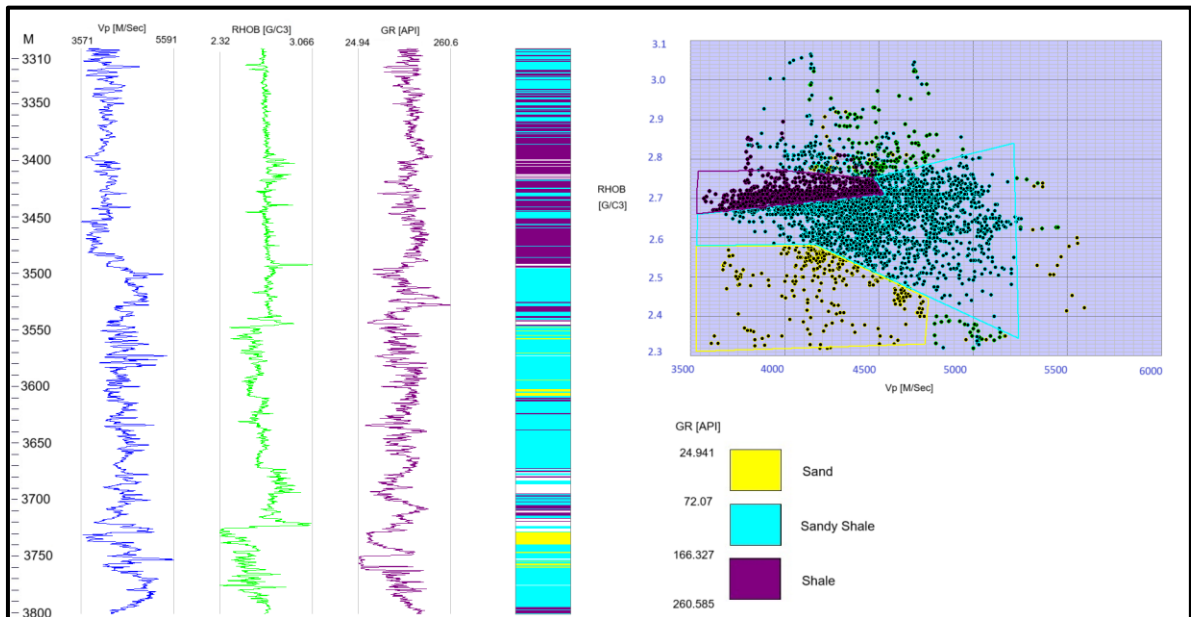


Figure 6.9 Cross plots between Vp and Density of C and B intervals in depth interval ranging from 3310 to 3800 m of Tajjal-03.

Explanation:

Cross plots between Vp and density were computed. Gamma ray is used as a benchmark for color coding between sand and shale. And for color variation between sand and shale. As seen in Figure 6.9, three distinct packages are plotted namely sand, shale, and sandy shale. The gamma ray values for sand lie between 24.941-72.09, sandy shale depicted by cyan color lie between 72.07-166.327, and shale depicted by purple color lie between 166.327-260.585. This separation between three facies on the basis of gamma ray is behind the scenes done by neural networks automatically. The neural network scans the trend of data

and then classifies it into distinct facies. Lower values of gamma ray correspond to clean lithology i.e., sand, and higher values of gamma ray are indicative of shale and in between the sand and shale, sandy shale lies at an intermediate gamma ray value.

After the construction of cross plots between V_p and V_s polygons are constructed. Polygons are drawn around clusters of data points as shown in the cross plot which help in marking the boundaries of the three lithologies i.e., sand, sandy shale, and shale. These polygons are quite useful since they help identify various facies and the transition between them.

6.9.3 Cross plots between V_s and Density

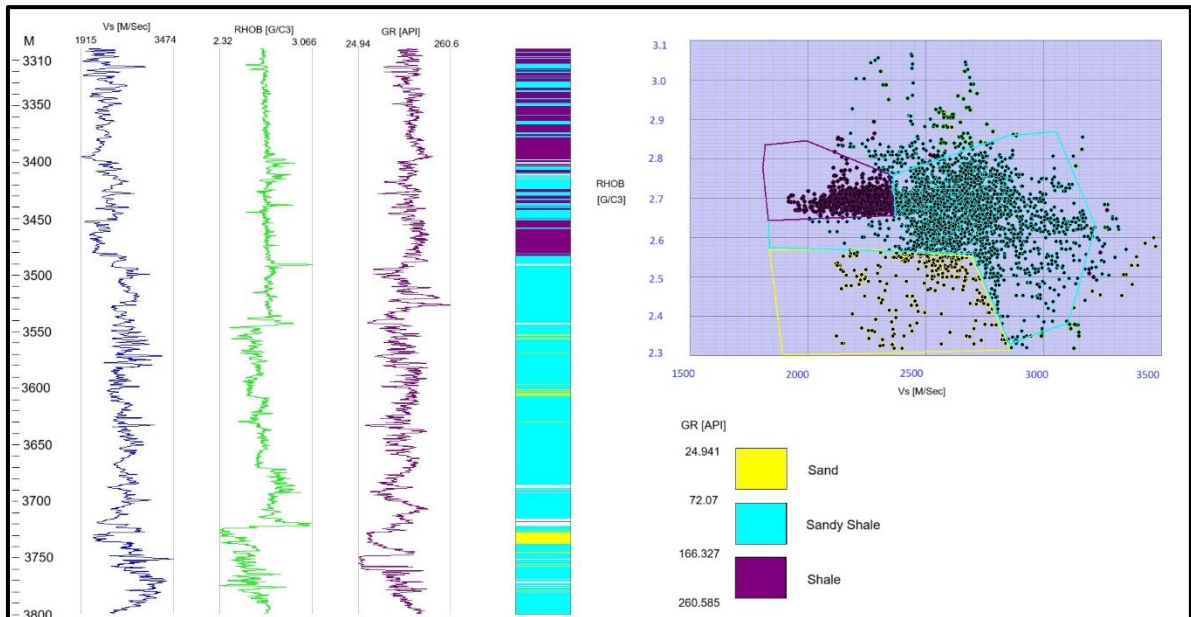


Figure 6.10 Cross plots between V_s and Density of C and B intervals in depth intervals ranging from 3310 to 3800 m of Tadjal-03.

Explanation:

Cross plots between Vs and density were computed. Gamma ray is used as a benchmark for color coding between sand and shale. And for color variation between sand and shale. As seen in Figure 6.10, three distinct packages are plotted namely sand, shale, and sandy shale. The gamma ray values for sand lie between 24.941-72.09, sandy shale depicted by cyan color lie between 72.07-166.327, and shale depicted by purple color lie between 166.327-260.585. This separation between three facies on the basis of gamma ray is behind the scenes done by neural networks automatically. The neural network scans the trend of data and then classifies it into distinct facies. Lower values of gamma ray correspond to clean lithology i.e., sand, and higher values of gamma ray are indicative of shale and in between the sand and shale, sandy shale lies at an intermediate gamma ray value.

After the construction of cross plots between Vp and Vs polygons are constructed. Polygons are drawn around clusters of data points as shown in the cross plot which help in marking the boundaries of the three lithologies i.e., sand, sandy shale, and shale. These polygons are quite useful since they help identify various facies and the transition between them.

Gamma ray logs have been used by a number of researchers for facies analysis. However, those studies used the trend and shape of gamma ray log to predict various sedimentary facies. The same approach was used by (Nazeer et al., 2016) to predict various types of facies and the facies were predicted according to the trend and shape of the gamma ray log. Since gamma ray log serves as an indicator of lithology/ facies classification, five facies namely shale, siltstone, argillaceous limestone, marl, and limestone were identified by (Nazeer et al., 2016) on the basis of shape of gamma ray log motif. However, during my research the facies were not classified according to the shape of the gamma ray log but rather the separation between the facies on the basis of gamma ray is behind the scenes done by neural networks, neural network scans the trend of data and then classifies into different facies. The facies are classified in a manner that low gamma ray values correspond to sand, high indicate shale and the intermediate values of gamma ray log are indicative of sandy shale. In future will employ the usage of 3D cross plots for facies classification.

CHAPTER 07

Machine Learning Based Geomechanics

7.1 Introduction

The study of mechanical behavior of geological materials is known as geomechanics. These studies, engineering components or applied geomechanics, describe how mining activities affect the geological environment (Ostad et al., 2018).

Understanding the stability and integrity of the borehole while drilling is largely dependent on geomechanics. The wellbore's presence and drilling fluids' pressure cause change in the rocks or the stress condition. Young modulus, bulk modulus, shear modulus and poisson's ratio are examples of elastic and inelastic geomechanical properties (fracture gradient and formation strength) (Ostad et al., 2018).

Young modulus is often referred to as the modulus of elasticity. Young modulus is defined as the ability of the material to mechanically withstand compression or elongation relative to its length. When the volume is involved in three-dimensional deformation, the ratio of applied stress to volumetric strain is referred to as the bulk modulus. Shear modulus, which is commonly referred to as the modulus of rigidity, is the measurement of body's rigidity that is determined by the relationship between shear stress and shear strain. The poisson's ratio is the proportion of a material's change in length in width per unit width to its change in length per unit length due to strain (Wang, 2001).

The pore fluid pressure in a reservoir decreases when hydrocarbons are produced from it (unless particular measures are taken to prevent that). Reduced pore pressure indicates that the reservoir is shrinking, and the effective stress is increasing. The stress path, which is

mostly determined by the response of the surrounding reservoir, determines how the reservoirs actually deform (Ostad et al., 2018).

During my research in terms of geomechanics analysis I will be calculating vertical effective stress, overburden gradient, pore pressure and fracture pressure.

- **Overburden pressure:** The weight of the rocks and the earth above the formation exerts a pressure on the rock, which is known as overburden pressure. When the overburden pressure is greater than the fluid pressure in the pore spaces the formation becomes more compacted (Baker et al., 2015).
- **Vertical effective stress:** The pressure acted on the solid rock framework is known as vertical effective stress. The compaction in rocks is controlled by effective stress and reducing the effective stress results in the over pressure exploration (Khan et al., 2017)
- **Pore pressure:** Pore pressure is the pressure that is exerted on fluid in a formation's pore space. Estimates of subsurface pressure regimes are crucial for lowering drilling related risks and uncertainty, and an awareness of pore pressure is helpful throughout the whole exploration and development process. Pore pressure information can help with knowing basin geometry, integrity of trap, the division of pressure regard to structure, and the detection of sealing and leaking of faults during exploration (Khan et al., 2017).
- **Pore pressure gradient:** At any given depth the pore pressure gradient is calculated by dividing the pore pressure by the true vertical depth (Khan et al., 2017).
- **Fracture Gradient:** The formation undergoes tensile failure at the practical pressure. As a result, the predicted fractured gradient represents the maximum possible mud weight without causing mud loss within the formation (Khan et al., 2017).

During the course of this research the following three workflows were adopted to perform geomechanics analysis.

7.2 Description of first workflow

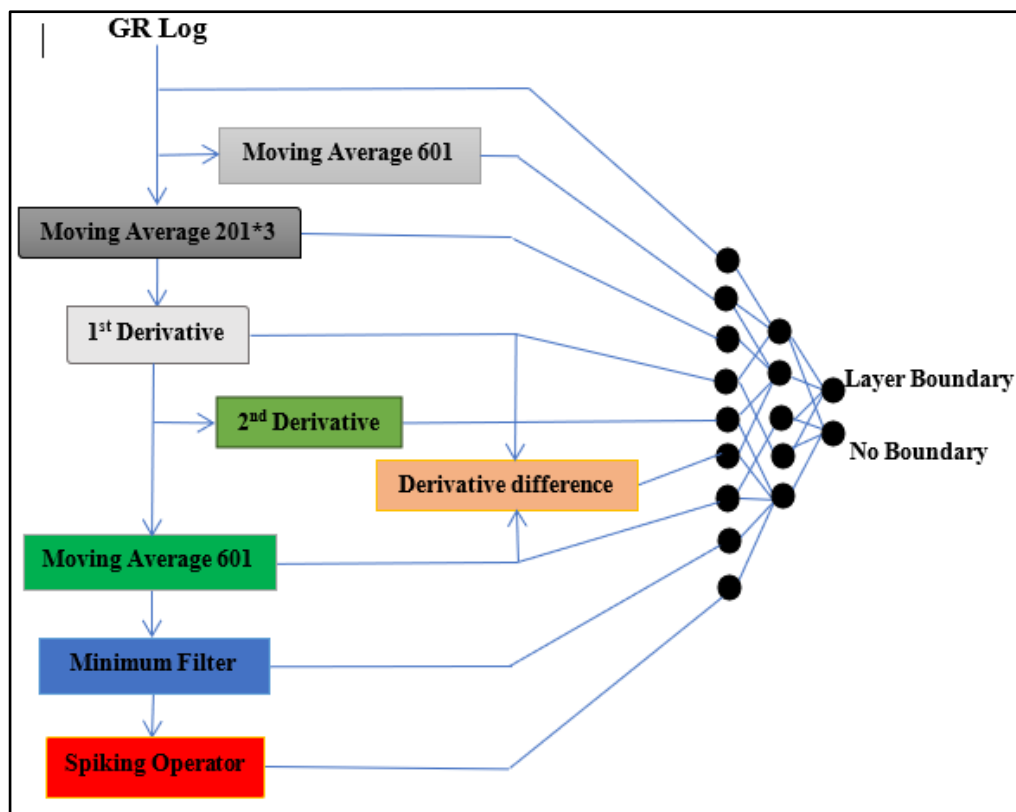


Figure 7.1 First Workflow adopted for delineation of layer boundaries in Tajjal-03.

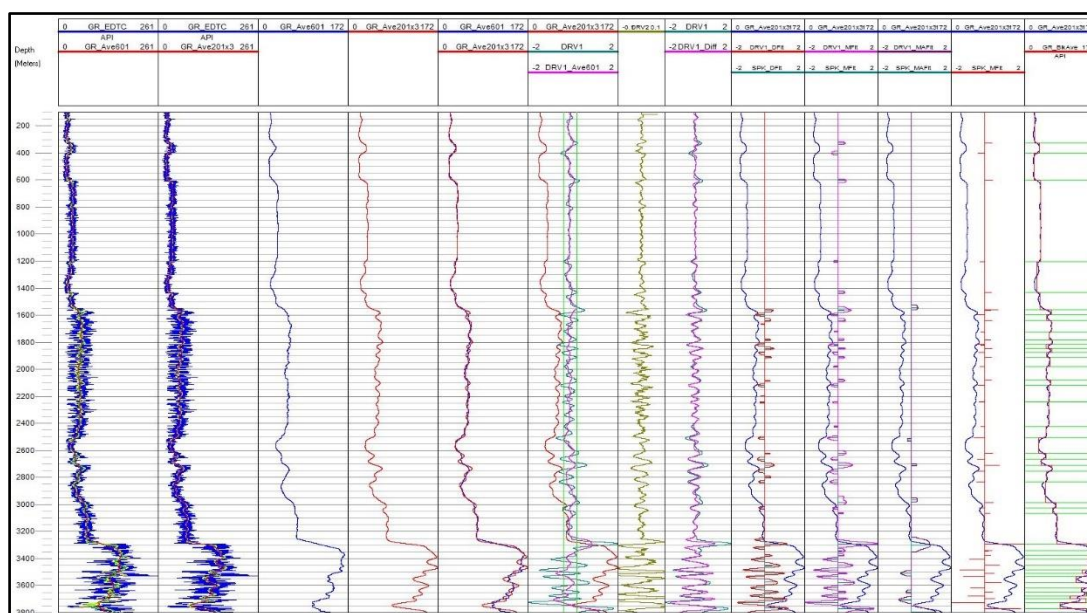


Figure 7.2 Output generated by adapting the first workflow for delineation of layer boundaries in Tajjal-03.

In this first workflow artificial intelligence or neural networks are used to identify and mark boundaries between different layers. Wireline log data of 5 to 6 wells in the surrounding of study area were used for training the model. Curve analytic techniques are used in the machine learning model which include various types of regressions, moving averaging techniques as well as various orders of derivatives. The model selects an optimum level of moving average operator in order to remove localized variations from the data while the derivatives identifies the boundary. In this first workflow a single log is used instead of using combination of logs. Gamma ray is used as an input log and after applying different algorithms on the gamma ray log we derived variants of gamma ray log from this single log. So, among them the very first log is moving average of 601 samples, and it has been superimposed on the first log in the first column and it has been independently shown in the third track in addition to that a moving average of 201 samples is also applied since 201 averages would be doing less moving, so it has been applied thrice so in the second track it has been displayed along with the original log. The 201*3 is independently displayed in the fourth track and in the fifth track both the moving average of 601 and 201*3 are being displayed. The moving average of 601 is represented by blue color and moving average of 201*3 is represented by red color.

After observing my own log, I concluded that the moving average of 201*3 is a better choice to be used as an input fed to the neural networks this is because the moving average of 601 has more ringing that is vibration, and the layer information is also lost. However, in the case of 201*3-layer information is preserved this affect can be clearly seen in Figure 7.2 within depth of 1600 till 2000 m.

After calculating the moving average, the first and second derivative of the smooth version i.e., moving average of 201*3 was computed. The first derivative (DRV1) is shown in track 6 Figure 7.2 represented by green color and the second derivative (DRV2) is shown in track 7 Figure 7.2 represented by green color. As can be seen in Figure 7.2, the second

derivative shows many fluctuations and is quite noisy that's why further only the first derivative would be used. Now further a moving average of 601 is again applied to the first derivative and the output is shown in track 6 (DRV1_Ave601) by pink color.

Now based on minimum and maximum values we have plotted 2 reference lines in track 6 shown by green color which can be 5 to 10% of the maximum values. The basic idea is that any change smaller than this would be neglected and any change greater than these reference lines would be used.

Now in track 8 we are just plotting first derivative(DRV1) along with the difference of the first derivative and its smooth version shown in pink color (DRV1_Diff) so the peaks would get reduced.

And then we applied a difference filter. In track 9 the curve shown by blue color is moving average of 201×3 of gamma ray log (GR_Ave201x3). And the red color shows the output of the difference filter (DRV1_DF1t).. The difference filter was applied on the difference of the first derivative and it's moving average. As seen in Figure 7.2 difference filter is also picking unnecessary information it is also picking small changes and shows unnecessary peaks, so an alternate approach is to use minimum filter.

Now in track 10 the output of the minimum filter is shown by pink color (DRV1_MF1t). The aim of the minimum filter is we specify based on the maximum and minimum value some percentage like 10% of those values we define minimum and maximum reference value(lines). Any value within these maximum and minimum line will be 0 and values greater than these lines would be passed out. And the minimum reference line and maximum reference lines are shown in track 6 by green color.

And now on this filter we have applied a spiking operator. It scans minimum difference trace and whenever the value is nonzero it can be greater than zero for a peak and it can be less than zero in case of trough. So, it scans all the non-zero samples and in case of positive samples it scans them and finds the location of the highest sample. It then marks that sample and assigns the zero value to the rest of the samples and similarly for a negative or trough cycle it again scans all the samples and marks the minimum value and resets the rest of the samples as zero and as a result we get this spiking output shown in track 10.

In track 11 an attempt has also been made to apply spike operator on the moving average but as it can be seen in Figure 7.2, that this curve is quite smooth and shows almost negligible variations thus it is of no significance.

In the 12th track moving average of gamma ray 201*3 is being displayed by blue color(GR_Ave201x3) along with the spike minimum filter output (SPK_MFlt). (Spike has been applied on the minimum filter) is displayed by red color. All the spikes in this log indicate that these are the points which are boundaries where the layer is changing. A positive value indicates that the log value is increasing, and a negative spike indicates that the log value is decreasing. Secondly, if the peak is much higher it indicates that the log value is increasing at a higher rate and vice versa.

Finally, we cancel out either it is a positive peak or negative peak or whatever is the amplitude we just pick the depth points as markers and just draw straight lines. In the last track gamma ray log moving average is being displayed by blue color and all these spikes are now marked as markers which is the interface between layers and finally within these the spikes are used to mark the depth intervals which are the interface between various layers. And within each interval gamma ray intervals block average is also being carried out shown by red color (GR_BlkJAve). The code for this workflow has been taken from fellow research student (Amber Latif, 2023).

7.3 Description of second workflow

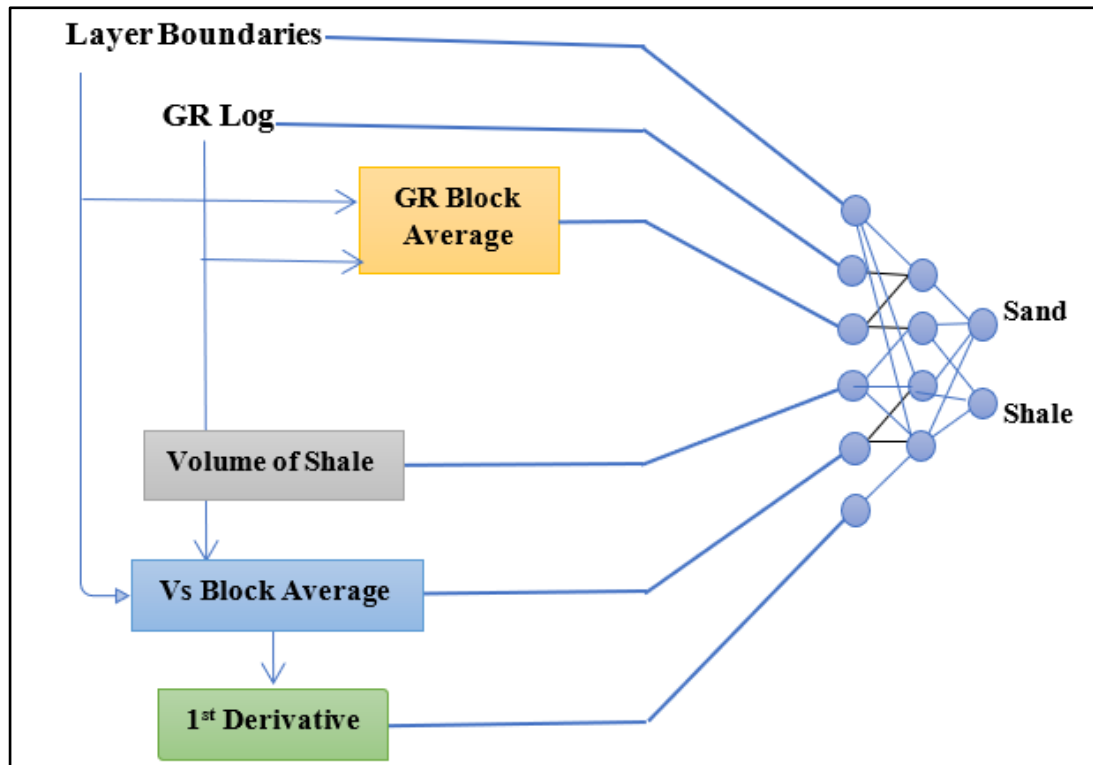


Figure 7.3 Second Workflow for calculating the block averages for shale volume in Tajjal-03.

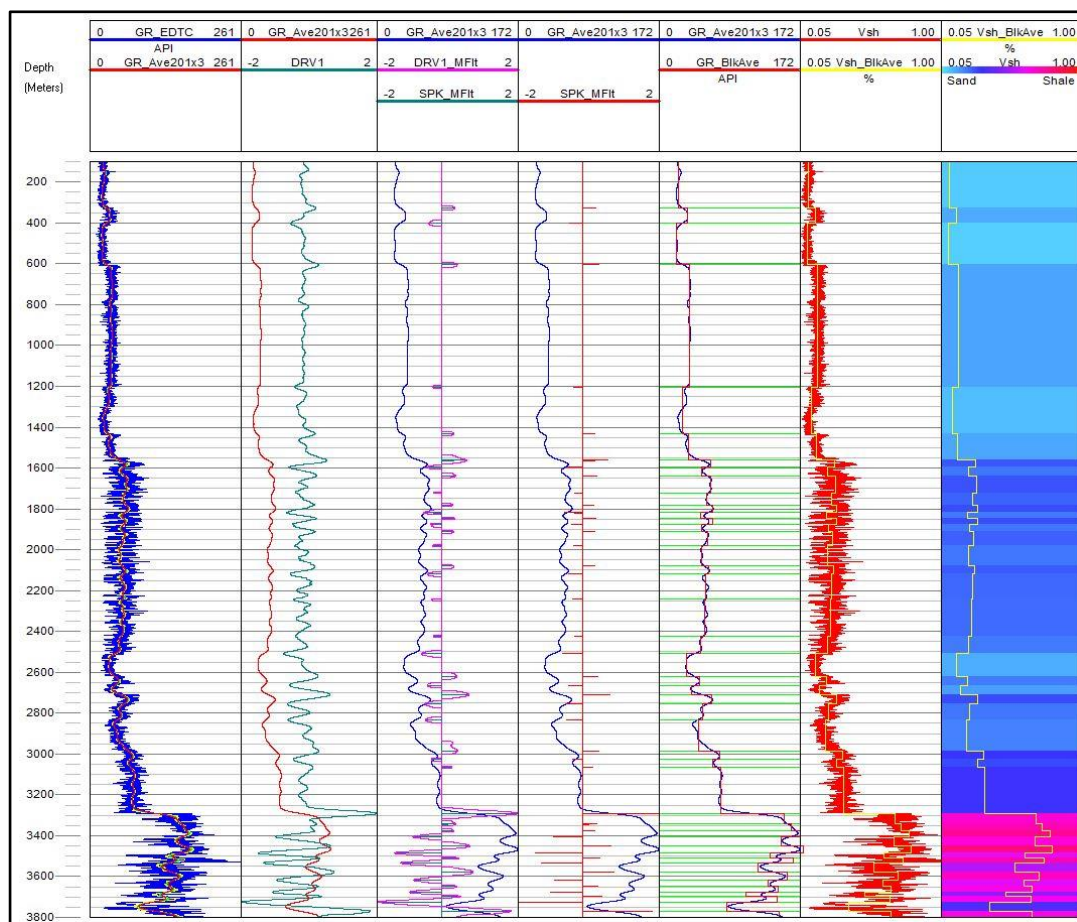


Figure 7.4 Output generated by adapting the second workflow calculating the block averages for shale volume in Tajjal-03.

In the previous workflow using the neural network the interface between layers was identified.

The second workflow utilizes the previous workflow in identifying the layer boundary and then by using these layer boundaries it computes the volume of shale from gamma ray and within these boundaries it applies a block average to the volume of shale.

As seen in Figure 7.4 gamma ray log (GR_EDTC) is displayed by blue color along with its block average 201*3 (GR_Ave201x3) by red color in the first track. In the second track block average 201*3 (GR_Ave201x3) is displayed in red color along with the first derivative (DRV1) by green color. The third tracks show the outputs of block average 201x3

(GR_Ave201x3) by blue color, the output of the minimum filter is shown by pink color (DRV1_MFlt) along with the output of spiking filter applied on moving average shown by green color (SPK_MFlt).

In the fourth track gamma ray block average 201*3 (GR_Ave201x3) is displayed by blue color along with the spike minimum filter output (SPK_MFlt).(spike has been applied on the minimum filter) is displayed by red color.

In the fifth track gamma ray block average 201x3 (GR_Ave201x3) is displayed by blue color along with the gamma ray intervals block average being carried out in each interval is shown by red color (GR_BlkJve).

The second workflow utilizes the previous workflow in identifying the layer boundaries and then by using these layer boundaries it's computes the volume of shale from gamma ray and within these boundaries it applies a block average to the volume of shale as shown in track 6. Afterwards, it applies a color spectrum to it. The light blue color indicates sand and gradually when it becomes darker shale component is being added and finally red means pure shale as shown in track 7. So, from the color spectrum it is automatically classifying which one is clean sand, pure sand shale, intermediate etc. The code for this workflow has been taken from fellow research student (Amber Latif, 2023).

The aim of previous workflow was to mark the boundaries however in this workflow we are taking previous inputs that is the boundaries along with computing the volume of shale and doing the block average and then through the neural network we are automatically classifying between sand, shale and various variants and gradual changes between them through the color.

7.4 Description of third workflow

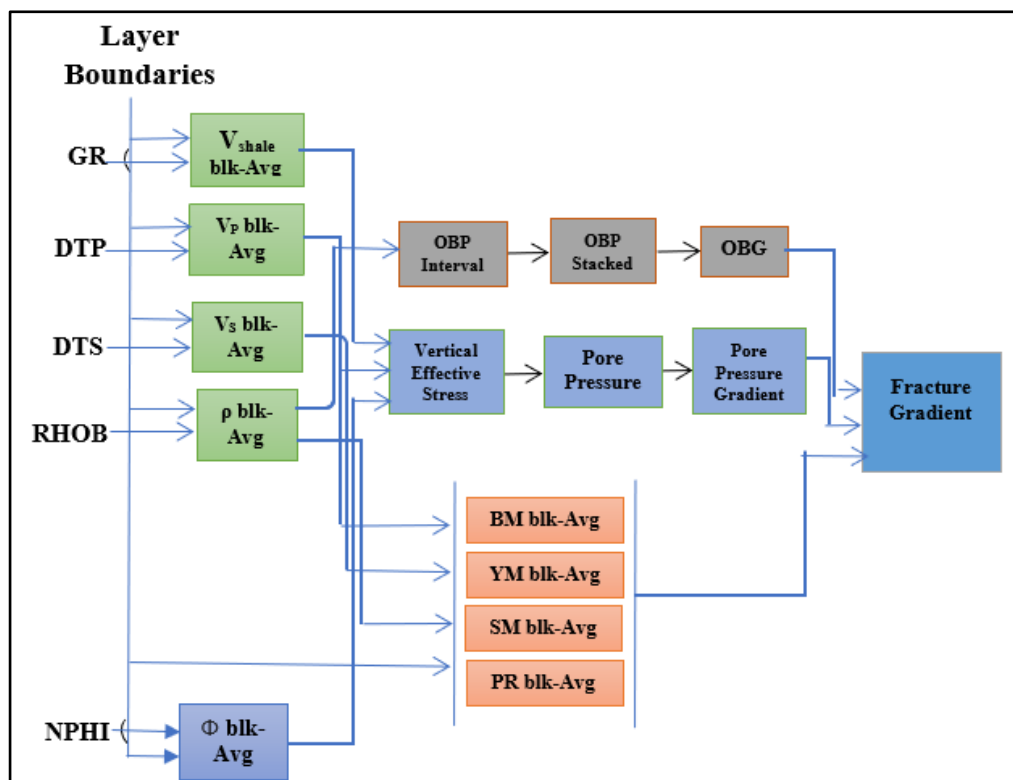


Figure 7.5 Third Workflow for computation of geomechanical parameters for Tajjal-03.

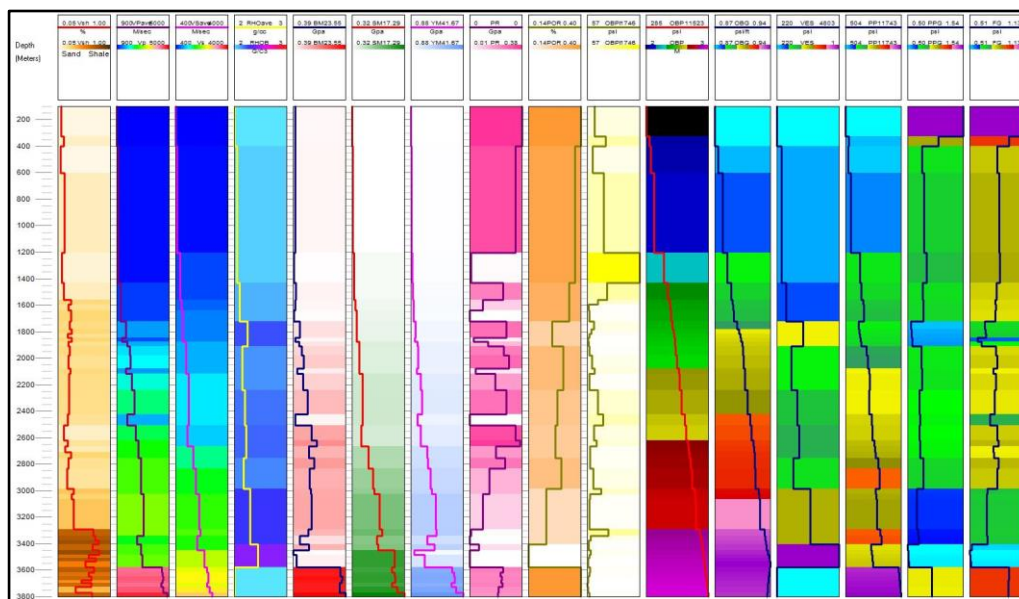


Figure 7.6 Output generated by adapting the third workflow for computation of geomechanical parameters for Tajjal-03.

The third workflow begins from the volume of shale then there is block average of volume of shale. Yellowish is sand and brown is shale.

In the previous work flow the volume has been characterized between sand and shale and now using the same markers VP is computed from DT and again its block average is computed and displayed in second track. Similarly using the shear sonic log, the block average shear velocity is computed and displayed in the third track and finally the RHOB density log is used, and its block average is computed within the interval and displayed in the fourth track.

Now using these three logs all rock physics parameters are computed in the block average form which include:

BM means bulk modulus displayed in track five, shear modulus is displayed in track six, young modulus is displayed in track seven and poisson ratio is displayed in track eight. Track nine shows porosity which can be calculated from the density log.

Now we have all these parameters ready, now using the density log overburden pressure is computed for each interval displayed in track ten. Obpi which means overburden pressure for every interval. The overburden pressure is calculated from the formula given by (Bryant, 1986). Overburden pressure is also called vertical stress and lithostatic pressure.

After that the overburden pressure from top to bottom along with the depth stacked gives the total overburden pressure displayed in track eleven. It can be seen that it is continuously increasing and then from the overburden pressure we are computing overburden gradient which means rate of change it is displayed in track thirteen. Now in addition to overburden gradient there is another parameter which is vertical effective stress which can be computed in two ways. It can be computed from interval velocity using the equation given by (Bowers, 1994).

The pore pressure is also computed shown in track fourteen and it is calculated by calculating the difference between overburden pressure and vertical effective stress (Terzaghi, 1943). The rate of change of pore pressure is called pore pressure gradient. It is

displayed in track fifteen. And finally fracture gradient is calculated by (Eaton, 1969) using pore pressure gradient, overburden gradient and poisson ratio and displayed in last track.

In this final workflow we are calculating geo mechanical properties from the logs, in the first stage artificial intelligence used markers computed the volume of shale and using the same markers we have taken sonic log and computed block average p wave velocity, similarly shear sonic is used to compute block average shear velocity. RHOB log is used to compute density block average and finally using these three parameters all rock physics parameters like bulk modulus, shear modulus, young modulus and poisson ratio are computed in the block average form. Similarly, porosity log is also blocked averaged.

And now using the density we have computed the overburden pressure for each interval and now staking all these individuals overburden pressure for each interval stacking them together we get the total overburden pressure at a given depth show in track 11. And finally using vertical effective stress equation (Bowers, 1994) we have computed vertical effective stress from the interval velocity.

After that the pore pressure is also computed and it is calculated from the equation given by (Terzaghi, 1923). The rate of change of pore pressure is called pore pressure gradient. It is displayed in track fifteen. And finally fracture gradient is calculated by (Eaton, 1969) using pore pressure gradient, overburden gradient, and poisson ratio and displayed in last track. The source code for this workflow is given in annexure A.

7.5 Results and discussions

Identifying and demarking the thin beds plays an important role during the exploration, appraisal and development phases during the oil and gas exploration. Identifying these thin beds is challenging because of resolution problems associated with seismic methods (Lu, 2019). Thin beds could be only a few meters wide or even less and thus the minor effect produced by these beds cannot be distinguished and taken into consideration by using the conventional seismic method (Nizarul et al., 2016). Number of approaches have

been used in the past to resolve the thin beds and thus certain seismic attributes have been applied by various researchers for demarking the thin beds. In order to predict the thin beds (Zhao et al., 2021) developed a frequency-dependent attribute. Several attributes were used by (Hossain, 2019) for identifying the thin beds. However, during the course of my research I did not use the conventional seismic data for demarking the layer boundaries but rather used well data owing to its better resolution as compared to seismic method. Afterwards ML was used to demarking the thin beds by using well data as an input.

The second task was to calculate the geomechanical parameters. Calculating these parameters is essential because understanding the stability and integrity of the borehole while drilling is largely dependent on geomechanics. One of the most crucial variables needed for precise geomechanical analysis to reduce well bore stability issues is pore pressure prediction. Accurate pore pressure prediction and geomechanical analysis is very important for safe well drilling and well planning (Satti, 2018). Though, pore pressure prediction is not simple and easy in over-pressured clastic rocks, it becomes even more complicated in complex geology where clastic (sandstone, shale) and non-clastic (limestone) rocks are inter-bedded (Satti, 2018). The majority of deep sedimentary formations have pore pressures that are over pressured and even higher than the higher static pressures disasters and thus blowouts and mud volcanoes may occur if the anomalous pressures are not adequately forecasted before drilling (Zhang, 2011). Various methods have been applied by previous researchers to compute the pore pressure by using seismic and well log data, but my study mainly focuses on using ML to compute pore pressure, fracture pressure, pore pressure gradient, fracture gradient etc. The pore pressure was calculated by calculating the difference between overburden pressure and vertical effective stress (Terzaghi, 1943). At relatively shallow depths, relatively those less than 2000 m, pore pressure remains hydrostatic (Zhang, 2011). This suggests that a continuous column of pore fluid, extending from the surface to this depth exists. Beyond this depth, usually over pressure starts, and as the depth increases, the pore pressure rises noticeably (Zhang, 2011). The pore pressure reaches a point that is quite near to the overburden stress value at depths greater than 3800 m or more and this is called “hard overpressure” (Zhang, 2011). Similar trend is apparent in my study as shown in Figure 7.6, the pore pressure is increasing at a less rate at shallow depths till 2000 m, but it increases rapidly after 2000 m and at the depth of 3800 m it has begun to increase at a very

higher rate. Pore pressure gradients are more commonly used in drilling engineering because they provide a more convenient way to measure mud weight and mud density (Zhang, 2011). The pore pressure gradient is the rate of change of pore pressure and is shown in track 16 in Figure 7.6. The fracture gradient is calculated by (Eaton, 1969) using pore pressure gradient, overburden gradient, and poisson ratio and displayed in the last track in Figure 7.6.

The pressure gradient at which the formation fractures or breaks is known as fracture gradient. Prior to starting a hydraulic fracturing operation, determining the predicted bottom hole treatment pressure (BHTP) requires an understanding of the fracture gradient (Belyadi et al., 2019). The pore pressure gradient and fracture gradient both follow a similar trend. Both have a smooth, non-fluctuating trend within the depth intervals of 400 m till 1700 m and then their values decrease rapidly at depth of 3000 m as shown in Figure 7.6. At the depth of 3500 m, their values reach the minimum value and beyond the depth of 3500 m an increasing trend is being followed shown in Figure 7.6.

CONCLUSIONS

- 3D seismic interpretation has revealed that the study area is located in an extensional tectonic setting, characterized by the presence of two clearly defined normal faults on the seismic section. Additionally, when examining the time and depth contour maps, it becomes evident that the C interval exhibits a more pronounced behavior in terms of hydrocarbon presence compared to the B interval.
- The petrophysical analysis of both Tajjal 01 and Tajjal 02 wells has identified distinct zones within the Lower Goru B and C Sands levels in both wells. In the C interval, hydrocarbon saturation (Sh) falls within the range of 71% to 86%, while in the B interval, Sh ranges from 30% to 50%. These findings suggest that the C interval possesses a greater potential for hydrocarbon accumulation.
- Seismic inversion analyzed impedance changes in C and B intervals of the Lower Goru Formation. It identified a significant impedance drop at Tajjal 01 and Tajjal 02 along the C sand channel, suggesting possible hydrocarbon accumulation. In contrast, the B sand channel showed lower impedance only at Tajjal 01, indicating higher hydrocarbon potential in the C interval.
- Seismic attributes were utilized to detect thin sand units. The Spectral Decomposition technique highlights distinct zones within the B and C sand Formation. It was observed that thinner sand beds of Lower Goru B and C sand in the Tajjal 02 well became visible as the frequencies increased. The instantaneous phase is a reliable indicator of lateral continuity. When applied, the Instantaneous phase attribute changed from -105° to $+105^{\circ}$. The interpreted horizons lie over the maximum phase

regions indicated by violet color in the instantaneous phase attribute. The results of trace envelope attribute suggest that high energy area i.e., C interval of lower Guru Formation could be having presence of hydrocarbons. The results of petrophysical analysis also reveal that C interval is hydrocarbon bearing.

- Vs (shear velocity) was determined through two methods and validated through AVA (amplitude versus angle) modeling. The first method utilized the Castagna equation, while the second employed Machine Learning for Vs calculation. When AVA modeling was conducted using Vs computed via the Castagna equation, no AVA anomaly was detected, and there was an observed amplitude dimming effect at far offsets. However, the shear sonic data computed through multiple regression, particularly from Machine Learning, revealed the presence of gas sands. This leads to the conclusion that Vs computed through Machine Learning is more reliable and yields better results compared to the Castagna equation method.
- Machine learning facilitated facies analysis, categorizing them into three distinct lithological packages: sand, shale, and tight sand. It additionally computed specific equations for each of these lithological packages.
- Machine learning was applied in three sequential steps to calculate various geomechanical parameters. In the first step, artificial intelligence or neural networks were employed to identify and delineate boundaries between different geological layers using the gamma ray log as input. In the second step, the identified layer boundaries were utilized to compute the volume of shale from the gamma ray log, and a block averaging technique was applied within these boundaries. Finally, in the third step, leveraging input from the previous workflows, essential rock physics parameters such as bulk and young shear modulus were computed, alongside critical geomechanical parameters like vertical effective stress, pore pressure, and fracture gradient.

REFERENCES

- Abdolahi, A., Chehrazi, A., Rahimpour-Bonab, H., Kadkhodaie, A., Seyedali, S., & Rao, Y. (2022). Improving the 3D facies model with the seismic-derived log volumes: a case study from the Asmari Formation in the Hendijan Field, southwest Iran. *Journal of Geophysics and Engineering*, 19(5), 1028-1045
- Abdulaziz, A.M., Mahdi, H.A., Sayyouh, M.H., 2019. Prediction of reservoir quality using well logs and seismic attributes analysis with an artificial neural network: A case study from Farrud Reservoir, Al-Ghani Field, Libya. *Journal of Applied Geophysics* 161, 239-254.
- Abosalama, A. (2022, August 26). Use of Probabilistic Neural Network and Post Stack Inversion to Predict Reservoir Characterization in the Mediterranean Sea, Sapphire Field, Egypt. Longdom. <https://doi.org/10.35248/2381-8719.22.11.1042>
- Adero, Bernard & Masinde, Abiud & Osukuku, Godfred. (2017). Using Seismic Attributes for Reservoir Characterization.
- Afsar, F. (2013). ANALYSIS AND INTERPRETATION OF 2D/3D SEISMIC DATA OVER DHURNAL OIL FIELD, NORTHERN PAKISTAN.
- Ahmed, R., All, S. M., & Ahmad, J. (1994). Review of petroleum occurrence and prospects of Pakistan with special reference to adjoining basins of India, Afghanistan and Iran. *Pakistan Journal of Hydrocarbon Research*, 6(1 & 2), 7-18
- Ahmed, S., Solangi, S. H., Jadoon, M. S. K., & Nazeer, A. (2018). Tectonic evolution of structures in Southern Sindh Monocline, Indus Basin, Pakistan formed in multi-extensional tectonic episodes of Indian Plate. *Geodesy and Geodynamics*, 9(5), 358-366.
- Ahmad, S., Ahmad, F., Ullah, A., Eisa, M., Ullah, F., Kaif, K., & Khan, S. (2019). Integration of the outcrop and subsurface geochemical data: implications for the hydrocarbon source

rock evaluation in the Lower Indus Basin, Pakistan. *Journal of Petroleum Exploration and Production Technology*, 9, 937-951.

Ahmad, N., Khan, S., Noor, E. F., Zou, Z., & Al-Shuhail, A. (2021). Seismic data interpretation and identification of hydrocarbon-bearing zones of Rajian area, Pakistan. *Minerals*, 11(8), 891.

Ahmed, T. (2009). *Working guide to reservoir rock properties and fluid flow*. Gulf Professional Publishing.

Ali, M., Khan, M. J., Ali, M., & Iftikhar, S. (2019). Petrophysical analysis of well logs for reservoir evaluation: A case study of “Kadanwari” gas field, middle Indus basin, Pakistan. *Arabian Journal of Geosciences*, 12, 1-12.

Aly, A., Saleh, W., AbdelHalim, A., & Hamed, M. Pore Pressure and Fracture Gradient Modelling in Northwest Khilala Field, Onshore Nile Delta, Egypt

Ali, A., Alves, T. M., Saad, F. A., Ullah, M., Toqeer, M., & Hussain, M. (2018). Resource potential of gas reservoirs in South Pakistan and adjacent Indian subcontinent revealed by post-stack inversion techniques. *Journal of Natural Gas Science and Engineering*, 49, 41–55. <https://doi.org/10.1016/j.jngse.2017.10.010>

Amber 2023, “Geophysical Characterization and Machine Learning Based Quantitative Interpretation of Lower Goru Formation of Kadanwari Block, Middle Indus Basin Pakistan

Ashley Francis, *A Simple Guide to Seismic Inversion*, Vol. 10, No. 2 – 2014

Asim, S., Zhu, P., Naseer, M. T., Abbasi, S. A., & Rehman, M. (2016). An integrated study to analyze the reservoir potential using stochastic inversion, model-based inversion and petrophysical analysis: A case study from the Southern Indus Basin, Pakistan. *J. Earth Sci.*

Bagheri, M., & Riahi, M. A. (2015). Seismic facies analysis from well logs based on supervised classification scheme with different machine learning techniques. *Arabian Journal of Geosciences*, 8, 7153-7161

- Belyadi, H., Fathi, E., & Belyadi, F. (2019). Fracture pressure analysis and perforation design. In Elsevier eBooks (pp. 121–148). <https://doi.org/10.1016/b978-0-12-817665-8.00009-6>
- Baker, R. O., Yarranton, H. W., & Jensen, J. L. (2015). 7-conventional core analysis–rock properties. *practical reservoir engineering and characterization*, 197-237.
- Barclay, F., Rasmussen, A.B.K.B., Alfaro, J.C., Cooke, A., Salter, D., Godfrey, R., Lowden, B., McHugo, S., Ozdemir, H., Pickering, S., Pineda, F.G., Herwanger, J., Volterrani, S., Murineddii, A., Rasmussen, A., Roberts, R., 2008, *Seismic Inversion: Reading between the lines: Oilfield Review*, Vol. 20(1), pp 42-63..
- Barnes, A. E. (2007). A tutorial on complex seismic trace analysis. *Geophysics*, 72(6), W33–W43. <https://doi.org/10.1190/1.2785048>
- Bisht BS, Sas SK, Chaudhuri PK, Singh RBN, Singh SK (2013) Integration of petrophysics and rock-physics modelling in single workflow reduces uncertainty in seismic reservoir characterization: a case study. *Geohorizons* 44–47
- Bosch, M., Mukerji, T., & Gonzalez, E. F. (2010). Seismic inversion for reservoir properties combining statistical rock physics and geostatistics: A review. *Geophysics*, 75(5), 75A165-75A176.
- Bouvier, J. D., Kaars-Sijpesteijn, C. H., Kluesner, D. F., Onyejekwe, C. C., & Van der Pal, R. C. (1989). Three-dimensional seismic interpretation and fault sealing investigations, Nun River Field, Nigeria. *AAPG bulletin*, 73(11), 1397-1414.
- Bowers, G. L. (1995). Pore pressure estimation from velocity data: Accounting for overpressure mechanisms besides undercompaction. *SPE Drilling & Completion*, 10(02), 89-95.
- Brown, A. (2001). Understanding seismic attributes. *Geophysics* 66 (1), 47–48. [doi:10.1190/1.1444919](https://doi.org/10.1190/1.1444919)
- Bryant, T. (1989). A dual shale pore pressure detection technique. *All Days*. <https://doi.org/10.2118/18714-ms>

- Bryant, W et al. (1986): Geotechnical properties of Intraslope Basin sediments, Gulf of Mexico, Deep Sea Drilling Project Leg 96, Site 619. In: Bouma, AH; Coleman, JM; Meyer, AW; et al. (eds.), Initial Reports of the Deep Sea Drilling Project, Washington (U.S. Govt. Printing Office), 96, 819-824
- Caputo, M., & Postpischl, D. (2010). Contour mapping of seismic areas by numerical filtering and geological implications. *Annals of Geophysics*, 27(3–4). <https://doi.org/10.4401/ag-4939>
- Castagna, J. P., Sun, S., & Siegfried, R. W. (2003). Instantaneous spectral analysis: Detection of low-frequency shadows associated with hydrocarbons. *The leading edge*, 22(2), 120-127.
- Chambers, R. L., & Yarus, J. M. (2002). Quantitative use of seismic attributes for reservoir characterization. *CSEG recorder*, 27(6), 14-25
- Chen, X., Xing, T., Li, L., and Liu, S. (2018). Mistie problem and correction method of single channel seismic data in shallow sea. *IOP Conf. Ser. Earth Environ. Sci* 170 (2), 022062. doi:10.1088/1755-1315/170/2/02206
- Chopra, S and Marfurt, .K.J, Seismic attributes — A historical perspective,
Volume 70
- Cooke, D., & Cant, J. (2010). Model-based seismic inversion: Comparing deterministic and probabilistic approaches. *CSEG Recorder*, 35(4), 29-39.
- Cui, T., & Margrave, G. F. (2014). Seismic wavelet estimation. *CREWES Res Rep*, 26, 1-16.
- Dar, Q. U. Z., Renhai, P., Ghazi, S., Ahmed, S., Ali, R. I., & Mehmood, M. (2021). Depositional facies and reservoir characteristics of the Early Cretaceous Lower Goru Formation, Lower Indus Basin Pakistan: Integration of petrographic and gamma-ray log analysis. *Petroleum*.

- Dewar, J., & Pickford, S. (2001). Rock physics for the rest of us-an informal discussion. *CSEG Recorder*, 26(5), 42-49
- Downton, J. E. (2005). Seismic parameter estimation from AVO inversion (Vol. 10). University of Calgary, Department of Geology and Geophysics.
- Eaton, B. A. (1969). Fracture gradient prediction and its application in oilfield operations. *Journal of petroleum technology*, 21(10), 1353-1360
- Emujakporue, G. O., & Enyenihi, E. E. (2020). Identification of seismic attributes for hydrocarbon prospecting of Akos field, Niger Delta, Nigeria. *SN Applied Sciences*, 2, 1-11.
- Feng, H., & Bancroft, J. C. (2006). AVO principles, processing and inversion. *CREWES Research Report*, 18, 1-19.
- Freeman, B., Yielding, G., & Badley, M. (1990). Fault correlation during seismic interpretation. *First Break*, 8(3).
- Fjær, E. (2006). Geomechanics and geophysics for reservoir management. *Revue européenne de génie civil*, 10(6-7), 703-730.
- Glover, D. P. (1998). *Petrophysics*. University of Aberdeen, 65-150.
- González, A. S., van der Molen, M., Oaubel, M., & Dandapani, R. (2021). Amplitude and attribute analysis for reservoir characterization. In *Applied Techniques to Integrated Oil and Gas Reservoir Characterization* (pp. 119-152). Elsevier.
- Gupta, R., Srivastava, D., Sahu, M., Tiwari, S., Ambasta, R. K., & Kumar, P. (2021). Artificial intelligence to deep learning: machine intelligence approach for drug discovery. *Molecular diversity*, 25, 1315-1360.
- Helmberger, D. V., & Burdick, L. J. (1979). Synthetic seismograms. *Annual Review of Earth and Planetary Sciences*, 7(1), 417-442.

- Hussein, R. A., & Ahmed, M. E. B. (2012). Petrophysical evaluation of shaly sand reservoirs in Palouge-Fal oilfield, Melut Basin, Southeast of Sudan. *Journal of science and technology*, 13(2).
- Hossain, S. (2019). Application of seismic attribute analysis in fluvial seismic geomorphology. *Journal of Petroleum Exploration and Production Technology*, 10(3), 1009–1019. <https://doi.org/10.1007/s13202-019-00809-z>
- Imamverdiyev, Y., & Sukhostat, L. (2019). Lithological facies classification using deep convolutional neural network. *Journal of Petroleum Science and Engineering*, 174, 216-228.
- Jain, C. (2013). Effect of seismic wavelet phase on post stack inversion. In 10th Biennial Int. Conf. & Exposition, Kochi (p. 410).
- Kamel, M. H., & Mabrouk, W. M. (2003). Estimation of shale volume using a combination of the three porosity logs. *Journal of Petroleum Science and Engineering*, 40(3-4), 145-157.
- Karpatne, A., Ebert-Uphoff, I., Ravela, S., Babaie, H. A., & Kumar, V. (2018). Machine learning for the geosciences: Challenges and opportunities. *IEEE Transactions on Knowledge and Data Engineering*, 31(8), 1544-1554.
- Karim, Shefa & Islam, Md. Shofiquil & HOSSAIN, Mohammad & Islam, MD Aminul. (2016). Seismic Reservoir Characterization Using Model Based Post- Stack Seismic Inversion: In Case of Fen chuganj Gas Field, Bangladesh. *Journal of the Japan Petroleum Institute*. 59. 283-292. 10.1627/jbi.59.283
- Kazmi HA and Jan QA (1997). *Geology and Tectonics of Pakistan*.
- Kelly, K. R., Ward, R., Treitel, S., & Alford, R. M. (1976). SYNTHETIC SEISMOGRAMS: a FINITE -DIFFERENCE APPROACH. *Geophysics*, 41(1), 2–27. <https://doi.org/10.1190/1.144060>

- Khan, M., Nawaz, S., Shah, M., & Hasan, M. (2016). Interpreting seismic profiles in terms of structure and stratigraphy, an example from Lower Indus Basin Pakistan. *Universal Journal of Geoscience*, 4(3), 62-71.
- Khan, K. A., & Akhter, G. (2016). Review of instantaneous, wavelet, and weighted seismic attributes along with a computational library. *Arabian Journal of Geosciences*, 9, 1-7.
- Khan, K. A., Bangash, A. A., & Akhter, G. (2017). Raw seismic velocities aid predictions in mud program designs. *Oil & Gas Journal*, 115(11), 30-35.
- Kianoush, P., Mohammadi, G., Hosseini, S. A., Khah, N. K. F., & Afzal, P. (2023). Inversion of seismic data to modeling the Interval Velocity in an Oilfield of SW Iran. *Results in Geophysical Sciences*, 13, 100051.
- Koponen, A., Kataja, M., & Timonen, J. (1997). Permeability and effective porosity of porous media. *Physical Review E*, 56(3), 3319.
- Koson, S., Chenrai, P., & Choowong, M. (2014). Seismic attributes and their applications in seismic geomorphology. *Bulletin of Earth Sciences of Thailand*, 6(1), 1-9
- Krebs, J. R., Anderson, J. E., Hinkley, D., Neelamani, R., Lee, S., Baumstein, A., & Lacasse, M. D. (2009). Fast full-wavefield seismic inversion using encoded sources. *Geophysics*, 74(6), WCC177-WCC188.
- Kumar, R., Das, B., Chatterjee, R., & Sain, K. (2016). A methodology of porosity estimation from inversion of post-stack seismic data. *Journal of Natural Gas Science and Engineering*, 28, 356-364.
- Latimer R., Davison R. and van Riel P. 2000. An interpreter's guide to understanding and working with seismic-derived acoustic impedance. *The Leading Edge* 19, 242–256.
- Li, Y., Downton, J., & Xu, Y. (2003). AVO modeling in seismic processing and interpretation, part 1: Fundamentals. *CSEG Recorder*, 28(10).
- Lu, P. (2019, September 13). *Reservoir Characterizations by Deep-Learning Model: Detection of true sand thickness*. arXiv.org. <https://arxiv.org/abs/1909.06005>

- Mabrouk, W. M., & Kamel, M. H. (2011). Shale volume determination using sonic, density and neutron data. *Exploration Geophysics*, 42(2), 155-158.
- Magoon, L. B., & Dow, W. G. (1991). The petroleum system-from source to trap. *AAPG Bulletin (American Association of Petroleum Geologists);(United States)*, 75(CONF-910403-).
- Misra, A. A., & Mukherjee, S. (2018). Seismic structural analysis. *Atlas of Structural Geological Interpretation from Seismic Images*, 15-26.
- Moore, A. W., Anderson, B., Das, K., & Wong, W. K. (2006). Combining multiple signals for biosurveillance. *Handbook of biosurveillance*, 235.
- Munyithya, J. M., Ehirim, C. N., & Dagogo, T. (2019). Rock physics models and seismic inversion in reservoir characterization, "MUN" onshore Niger delta field. *International Journal of Geosciences*, 10(11), 981-994.
- Narayan, S., Sahoo, S. D., Kar, S., Pal, S. K., & Kangsabanik, S. (2023). Improved reservoir characterization by means of supervised machine learning and model-based seismic impedance inversion in the Penobscot field, Scotian Basin. *Energy Geoscience*, 100180. <https://doi.org/10.1016/j.engeos.2023.100180>
- (N.d.). Retrieved from <https://www.ppl.com.pk/content/tajjal-gas-field-overview>
- Naseer, M. T., & Asim, S. (2017). Continuous wavelet transforms of spectral decomposition analyses for fluvial reservoir characterization of Miano Gas Field, Indus Platform, Pakistan. *Arabian Journal of Geosciences*, 10, 1-20.
- Nazari Ostad, M., Niri, M. E., & Darjani, M. (2018). 3D modeling of geomechanical elastic properties in a carbonate-sandstone reservoir: a comparative study of geostatistical co-simulation methods. *Journal of Geophysics and Engineering*, 15(4), 1419-1431.
- Nazeer, A., Abbasi, S. A., & Solangi, S. H. (2016). Sedimentary facies interpretation of Gamma Ray (GR) log as basic well logs in Central and Lower Indus Basin of Pakistan. *Geodesy and Geodynamics*, 7(6), 432-443. <https://doi.org/10.1016/j.geog.2016.06.006>

- Nizarul, O., Hermana, M., Bashir, Y., & Ghosh, D. P. (2016). Improving Thin Bed Identification in Sarawak Basin Field using Short Time Fourier Transform Half Cepstrum (STFTHC) method. *IOP Conference Series*, 30, 012003. <https://doi.org/10.1088/1755-1315/30/1/012003>
- Onajite, E. (2014). Understanding Seismic Interpretation Methodology. In Elsevier eBooks (pp. 177–211). <https://doi.org/10.1016/b978-0-12-420023-4.00013-7>
- Othman, A. A., Fathy, M., & Maher, A. (2016). Use of spectral decomposition technique for delineation of channels at Solar gas discovery, offshore West Nile Delta, Egypt. *Egyptian Journal of Petroleum*, 25(1), 45-51.
- Pendrel, J. (2001). Seismic inversion—The best tool for reservoir characterization. *CSEG Recorder*, 26(1), 18-24.
- Qadri, S. M., Islam, M. A., & Shalaby, M. R. (2019). Application of well log analysis to estimate the petrophysical parameters and evaluate the reservoir quality of the Lower Goru Formation, Lower Indus Basin, Pakistan. *Geomechanics and Geophysics for Geo-Energy and Geo-Resources*, 5(3), 271-288.
- Qiang, Z., Yasin, Q., Golsanami, N., & Du, Q. (2020). Prediction of reservoir quality from log-core and seismic inversion analysis with an artificial neural network: A case study from the Sawan Gas Field, Pakistan. *Energies*, 13(2), 486.
- Radwan, A.E., 2021. Modeling pore pressure and fracture pressure using integrated well logging, drilling based interpretations and reservoir data in the Giant El Morgan oil Field, Gulf of Suez, Egypt. *Journal of African Earth Sciences* 178, 104165.
- Radovich, B. J., and Oliveros, R. B. J. T. L. E. (1998). 3-D sequence interpretation of seismic instantaneous attributes from the Gorgon Field. *Lead. Edge* 17 (9), 1286–1293. [doi:10.1190/1.1438125](https://doi.org/10.1190/1.1438125)
- Robertson, J. D., & Nogami, H. H. (1984). Complex seismic trace analysis of thin beds. *Geophysics*, 49(4), 344–352. <https://doi.org/10.1190/1.1441670>

- Rider, M. H. (1986). The geological interpretation of well logs.
- Rider M (2002) The geological interpretation of well logs: Sutherland. Rider-French Consulting Ltd, ScotlandReturn to ref 2002 in article
- Russell, B.H., 1988, Introduction to seismic inversion methods: Society of Exploration Geophysicists
- Sams, M., & Carter, D. (2017). Stuck between a rock and a reflection: A tutorial on low-frequency models for seismic inversion. *Interpretation*, 5(2), B17–B27. <https://doi.org/10.1190/int-2016-0150.1>
- Satti, I. A. (2018). Pore pressure prediction and geomechanical modeling in different stress regimes. ResearchGate. https://www.researchgate.net/publication/322930554_Pore_Pressure_Prediction_and_Geomechanical_Modeling_in_Different_Stress_Regimes
- Sills, G. C. (1975). Some conditions under which Biot's equations of consolidation reduce to Terzaghi's equation. *Geotechnique*, 25(1), 129-132.
- Talib, M., Durrani, M. Z. A., Palekar, A. H., Sarosh, B., & Rahman, S. A. (2022). Quantitative characterization of unconventional (tight) hydrocarbon reservoir by integrating rock physics analysis and seismic inversion: a case study from the Lower Indus Basin of Pakistan. *Acta Geophysica*, 70(6), 2715-2731.
- Taner, M. T. (2001). Seismic attributes, rock solid images, Houston, TX, USA. CSEG Recorder, 48-56.
- Taner, M. T., Schuelke, J. S., O'Doherty, R., & Baysal, E. (1994). Seismic attributes revisited. In SEG technical program expanded abstracts 1994 (pp. 1104-1106). Society of Exploration Geophysicists.
- Tayyab, M. N., & Asim, S. (2017). Application of spectral decomposition for the detection of fluvial sand reservoirs, Indus Basin, SW Pakistan. *Geosciences Journal*, 21(4), 595-605.

- Terzaghi, K., "Theoretical soil mechanics," John Wiley and Sons Inc., 1943
- Toqeer, M., Ali, A., Alves, T. M., Khan, A., Zubair, & Hussain, M. (2021). Application of model based post-stack inversion in the characterization of reservoir sands containing porous, tight and mixed facies: A case study from the Central Indus Basin, Pakistan. *Journal of Earth System Science*, 130, 1-21.
- Veeken, P. C. H., & Da Silva, A. M. (2004). Seismic inversion methods and some of their constraints. *First break*, 22(6).
- Wandrey, C. J., Law, B. E., & Shah, H. A. (2004). Sembar Goru/Ghazij composite total petroleum system, Indus and Sulaiman-Kirthar geologic provinces.
- Wang, X., Zhang, B., Zhao, T., Hang, J., Wu, H., & Yong, Z. (2017). Facies analysis by integrating 3D seismic attributes and well logs for prospect identification and evaluation—A case study from Northwest China. *Interpretation*, 5(2), SE61-SE74
- Wang, Z. (2001). Fundamentals of seismic rock physics. *Geophysics*, 66(2), 398–412. <https://doi.org/10.1190/1.1444931>
- Ward, C. R. (1984). *Coal geology and coal technology*
- White, R. S. (1992). The accuracy of estimating Q from seismic data. *Geophysics*, 57(11), 1508–1511. <https://doi.org/10.1190/1.1443218>
- Yemets, V., Antoniuk, V., & Bezrodna, I. (2021, May). Facies interpretation from gamma ray (gr) log as basic well logs applied to Volodymyrska field (Dnipro-Donetsk depression). In *Geoinformatics* (Vol. 2021, No. 1, pp. 1-6). European Association of Geoscientists & Engineers.
- Yilmaz, O. (2001) *Seismic Data Analysis Processing, Inversion, and Interpretation of Seismic Data*. Society of Exploration Geophysicists, Tulsa, OK, 1028 p.

- Young, K. T., & Tatham, R. H. (2007). Fluid discrimination of poststack “bright spots” in the Columbus Basin, offshore Trinidad. *The Leading Edge*.
<https://doi.org/10.1190/1.2821936>
- Zamora, G., Carter, B., & Ferrer, O. (2022). Large transport thrust in the Huallaga sub-Basin (northern Peruvian sub-Andean zone). In *Andean Structural Styles* (pp. 275-284). Elsevier.
- Zhang, J. (2011). Pore pressure prediction from well logs: Methods, modifications, and new approaches. *Earth-Science Reviews*, 108(1–2), 50–63.
<https://doi.org/10.1016/j.earscirev.2011.06.001>
- Zhao, Z., Kumar, D., Foster, D. J., Dralus, D., & Sen, M. K. (2021). Frequency-dependent AVO analysis: A potential seismic attribute for thin-bed identification. *Geophysics*, 86(4), N1–N17. <https://doi.org/10.1190/geo2020-0777.1>

ANNEXURE A

```
picMain.Cls
```

```
picMain.CurrentX = 15
```

```
picMain.CurrentY = 50
```

```
picMain.Print "Depth"
```

```
picMain.CurrentX = 15
```

```
picMain.CurrentY = 70
```

```
picMain.Print "(Meters)"
```

```
DoEvents
```

```
pl.ReadLAS App.Path & "\Tajjal-02.las"
```

```
ds# = pl.GetDepthStart()
```

```
de# = pl.GetDepthStop()
```

```
ss& = pl.GetSampleIndex(ds)
```

```
es& = pl.GetSampleIndex(de)
```

```
ss& = pl.GetSampleIndex(100) 'Forced Depth Start
```

```
es& = pl.GetSampleIndex(3800) 'Forced Depth End
```

```
ds# = pl.GetDepth(ss) 'Forced Depth Start
```

```
de# = pl.GetDepth(es) 'Forced Depth End
```

```
Xo% = 80
```

```
Xw# = 80
```

```
pl.DrawDepthScale picMain, 10, 150, 60, 750, ds, de, 50, 200, QBColor(7), QBColor(8), QBColor(0)
```

```
pl.DrawDepthGrid picMain, Xo, 150, 845, 750, ds, de, 50, 200
```

```
gri% = pl.GetLogIndex("GR_EDTC")
```

```
pl.PutLogUnit gri, "API"
```

```
'-----1. Ave 201x3
```

```
pl.AllocateLogMemory "GRave1"      '1st Ave: gra1/GRave1
```

```
gra1% = pl.GetLogIndex("GRave1")
```

```
pl.PutLogMin gra1, pl.GetLogMin(gri)
```

```
pl.PutLogMax gra1, pl.GetLogMax(gri)
```

```
pl.MovingAverage gri, gra1, ss, es, 201
```

```
pl.AllocateLogMemory "GRave2"      '2nd Ave: gra2/GRave2
```

```
gra2% = pl.GetLogIndex("GRave2")
```

```
pl.PutLogMin gra2, pl.GetLogMin(gri)
```

```
pl.PutLogMax gra2, pl.GetLogMax(gri)
```

```
pl.MovingAverage gra1, gra2, ss, es, 201
```

```
pl.AllocateLogMemory "GRave201x3"  '3rd Ave: gra3/GRave202x3
```

```
gra3% = pl.GetLogIndex("GRave201x3")
```

```
pl.PutLogMin gra3, pl.GetLogMin(gri)
```

```
pl.PutLogMax gra3, pl.GetLogMax(gri)
```

```
pl.MovingAverage gra2, gra3, ss, es, 201
```

```
'-----2. Slope Computation: 1st Derivative: drv1/DRV1
```

```
pl.AllocateLogMemory "DRV1"
```

```
drv1% = pl.GetLogIndex("DRV1")
```

```
pl.Slope gra3, drv1, ss, es
```

```
pl.LogsMinMax
```

```
xs! = pl.GetLogMin(drv1)
```

```
xe! = pl.GetLogMax(drv1)
```

'-----3. 1st Derivative-Minimum Filter: drv1m/DRV1_MFlt

pl.AllocateLogMemory "DRV1_MFlt"

drv1m% = pl.GetLogIndex("DRV1_MFlt")

pl.FilterMinimum drv1, drv1m, ss, es, xs * 0.12, xe * 0.12

pl.PutLogMin drv1m, xs

pl.PutLogMax drv1m, xe

'-----4. 1st Derivative-Minimum Filter-Spike: spk1m/SPK_MFlt

pl.AllocateLogMemory "SPK_MFlt"

spk1m% = pl.GetLogIndex("SPK_MFlt")

pl.Spike drv1m, spk1m, ss, es

pl.PutLogMin spk1m, xs

pl.PutLogMax spk1m, xe

'-----5. Depth Intervals: di()..NI

Dim di&(), NI&

pl.DepthIntervals spk1m, ss, es, di(), NI&

'-----6. Clip Filter & Block Average GR: GRave(), DP()

ReDim GRave!(NI), dp!(NI)

pl.MaxClipFilter gri, ss, es, 220

pl.PutLogMax gri, 220

pl.BlockAverage gri, di(), NI, GRave()

For i& = 1 To NI

 dp(i) = pl.GetDepth(di(i))

Next

'-----7. Compute Volume of Shale

ReDim VSave!(NI)

```

pl.AllocateLogMemory "Vsh"

Vs% = pl.GetLogIndex("Vsh")

pl.SetGR0 pl.GetLogMin(gri)

pl.SetGR100 pl.GetLogMax(gri)

pl.GammaRayIndex gri, Vs, ss, es

pl.LogMinMax "Vsh", ss, es

pl.BlockAverage Vs, di(), NI, VSave()

pl.ReadColorSpectrum "C:\K-tron\Templates\ColorSpectrum\PAL-IP\Brown.pal"

pl.DrawFreeHeader picMain, Xo, 10, Xw, 130, 20, "Vsh", "%", pl.GetLogMin(Vs), pl.GetLogMax(Vs), QBColor(12), 3, , 2, 2.5

pl.DrawHeaderSpectrum picMain, Xo, 10, Xw, 130, 50, "Vsh", 6, , 2, 2.5

pl.DrawFreeHeaderText picMain, Xo, 10, Xw, 130, 1, 65, "Sand", QBColor(0), , 0

pl.DrawFreeHeaderText picMain, Xo, 10, Xw, 130, 85, 65, "Shale", QBColor(0), , 2

pl.SetGraphicsContext picMain, Xo, 150, Xw, 750, pl.GetLogMin(Vs), pl.GetLogMax(Vs), CSng(ds), CSng(de)

pl.DrawBlockFill pl.GetLogMin(Vs), pl.GetLogMax(Vs), VSave(), dp(), NI

pl.DrawBlockGraph VSave(), dp(), NI, QBColor(12), 3

pl.DrawTrackFrame picMain, Xo, 150, Xw, 750, 1

'-----8. Compute Vp

ReDim VPave!(NI)

dtp% = pl.GetLogIndex("DT4P")

pl.AllocateLogMemory "Vp"

Vp% = pl.GetLogIndex("Vp")

pl.DT2Velocity dtp, Vp, ss, es

pl.MinClipFilter Vp, ss, es, 900

'pl.LogMinMax "Vp", ss, es

pl.PutLogMin Vp, 900

pl.PutLogMax Vp, 5000

pl.SetDisplayScale "Vp", 900, 5000

```

```
pl.BlockAverage Vp, di(), NI, VPave()
```

```
PreSetPVals1 VPave()
```

```
Xo% = Xo + Xw + 10
```

```
Xw# = 80
```

```
pl.ReadColorSpectrum "C:\K-tron\Templates\ColorSpectrum\KCS\Color-V-CLR.kcs"
```

```
pl.DrawFreeHeader picMain, Xo, 10, Xw, 130, 20, "VPave", "M/sec", pl.GetLogMin(Vp), pl.GetLogMax(Vp), QBColor(5), 3, , , 2.5
```

```
pl.DrawHeaderSpectrum picMain, Xo, 10, Xw, 130, 50, "Vp", 6, , , 2.5
```

```
pl.SetGraphicsContext picMain, Xo, 150, Xw, 750, pl.GetLogMin(Vp), pl.GetLogMax(Vp), CSng(ds), CSng(de)
```

```
pl.DrawBlockFill pl.GetLogMin(Vp), pl.GetLogMax(Vp), VPave(), dp(), NI
```

```
pl.DrawBlockGraph VPave(), dp(), NI, QBColor(5), 3
```

```
pl.DrawTrackFrame picMain, Xo, 150, Xw, 750, 1
```

```
'-----9. Compute Vs
```

```
ReDim VSave!(NI)
```

```
dts% = pl.GetLogIndex("DT4S")
```

```
pl.AllocateLogMemory "Vs"
```

```
vss% = pl.GetLogIndex("Vs")
```

```
pl.DT2Velocity dts, vss, ss, es
```

```
pl.MinClipFilter vss, ss, es, 400
```

```
pl.LogMinMax "Vs", ss, es
```

```
pl.PutLogMin vss, 400
```

```
pl.PutLogMax vss, 4000
```

```
pl.SetDisplayScale "Vs", 400, 4000
```

```
pl.BlockAverage vss, di(), NI, VSave()
```

```
PreSetSVals1 VSave()
```

```
Xo% = Xo + Xw + 10
```

```
Xw# = 80
```

```
pl.ReadColorSpectrum "C:\K-tron\Templates\ColorSpectrum\KCS\Color-V-CLR.kcs"
```

```

pl.DrawFreeHeader picMain, Xo, 10, Xw, 130, 20, "VSave", "M/sec", pl.GetLogMin(vss), pl.GetLogMax(vss), QBColor(13), 3, , , 2.5
pl.DrawHeaderSpectrum picMain, Xo, 10, Xw, 130, 50, "Vs", 6, , , 2.5
pl.SetGraphicsContext picMain, Xo, 150, Xw, 750, pl.GetLogMin(vss), pl.GetLogMax(vss), CSng(ds), CSng(de)
pl.DrawBlockFill pl.GetLogMin(vss), pl.GetLogMax(vss), VSave(), dp(), NI
pl.DrawBlockGraph VSave(), dp(), NI, QBColor(13), 3
pl.DrawTrackFrame picMain, Xo, 150, Xw, 750, 1

```

'-----10. Density Process

```

ReDim RHOave!(NI)
rh% = pl.GetLogIndex("RHOM")
pl.PutLogCode rh, "RHOB"
pl.MinClipFilter rh, ss, es, 2
'pl.LogMinMax "Vs", ss, es
pl.PutLogMin rh, 2
pl.PutLogMax rh, 3
'pl.SetDisplayScale "Vs", 400, 4000
pl.BlockAverage rh, di(), NI, RHOave()
PreSetRVals1 RHOave()

```

Xo% = Xo + Xw + 10

Xw# = 80

```

pl.ReadColorSpectrum "C:\K-tron\Templates\ColorSpectrum\KCS\BlueRed.kcs"
pl.DrawFreeHeader picMain, Xo, 10, Xw, 130, 20, "RHOave", "g/cc", pl.GetLogMin(rh), pl.GetLogMax(rh), QBColor(14), 3, , , 2.5
pl.DrawHeaderSpectrum picMain, Xo, 10, Xw, 130, 50, "RHOB", 6, , , 2.5
pl.SetGraphicsContext picMain, Xo, 150, Xw, 750, pl.GetLogMin(rh), pl.GetLogMax(rh), CSng(ds), CSng(de)
pl.DrawBlockFill pl.GetLogMin(rh), pl.GetLogMax(rh), RHOave(), dp(), NI
pl.DrawBlockGraph RHOave(), dp(), NI, QBColor(14), 3
pl.DrawTrackFrame picMain, Xo, 150, Xw, 750, 1

```

```

'-----11. Rock Physics

ReDim BMave!(NI), SMave!(NI), YMave!(NI), PRave!(NI), PORave!(NI)

BMmin! = 9999: BMmax! = -9999

SMmin! = 9999: SMmax! = -9999

YMmin! = 9999: YMmax! = -9999

PRmin! = 9999: PRmax! = -9999

POmin! = 9999: POmax! = -9999

For i = 1 To NI - 1

    BulkModulus VPave(i), VSave(i), RHOave(i), BMave(i)

    ShearModulus VSave(i), RHOave(i), SMave(i)

    YoungsModulus BMave(i), SMave(i), YMave(i)

    PoissonsRatio VPave(i), VSave(i), PRave(i)

    Porosity RHOave(i), PORave(i)

    If PRave(i) < 0 Then PRave(i) = 0.01 'Check Filter

    If BMave(i) < BMmin Then BMmin = BMave(i)

    If BMave(i) > BMmax Then BMmax = BMave(i)

    If SMave(i) < SMmin Then SMmin = SMave(i)

    If SMave(i) > SMmax Then SMmax = SMave(i)

    If YMave(i) < YMmin Then YMmin = YMave(i)

    If YMave(i) > YMmax Then YMmax = YMave(i)

    If PRave(i) < PRmin Then PRmin = PRave(i)

    If PRave(i) > PRmax Then PRmax = PRave(i)

    If PORave(i) < POmin Then POmin = PORave(i)

    If PORave(i) > POmax Then POmax = PORave(i)

Next

pl.AllocateLogMemory "BM"

```

```
md% = pl.GetLogIndex("BM")
```

```
Xo% = Xo + Xw + 10
```

```
Xw# = 80
```

```
pl.PutLogMin md, BMmin
```

```
pl.PutLogMax md, BMmax
```

```
pl.ReadColorSpectrum "C:\K-tron\Templates\ColorSpectrum\CLR-Surfer\WhiteRed.clr"
```

```
pl.DrawFreeHeader picMain, Xo, 10, Xw, 130, 20, "BM", "Gpa", BMmin, BMmax, QBColor(1), 3, , 2, 2.5
```

```
pl.DrawHeaderSpectrum picMain, Xo, 10, Xw, 130, 50, "BM", 6, , 2, 2.5
```

```
pl.SetGraphicsContext picMain, Xo, 150, Xw, 750, BMmin, BMmax, CSng(ds), CSng(de)
```

```
pl.DrawBlockFill BMmin, BMmax, BMave(), dp(), NI
```

```
pl.DrawBlockGraph BMave(), dp(), NI, QBColor(1), 3
```

```
pl.DrawTrackFrame picMain, Xo, 150, Xw, 750, 1
```

```
Xo% = Xo + Xw + 10
```

```
Xw# = 80
```

```
pl.PutLogCode md, "SM"
```

```
pl.PutLogMin md, SMmin
```

```
pl.PutLogMax md, SMmax
```

```
pl.ReadColorSpectrum "C:\K-tron\Templates\ColorSpectrum\CLR-Surfer\WhiteGreen.clr"
```

```
pl.DrawFreeHeader picMain, Xo, 10, Xw, 130, 20, "SM", "Gpa", SMmin, SMmax, QBColor(12), 3, , 2, 2.5
```

```
pl.DrawHeaderSpectrum picMain, Xo, 10, Xw, 130, 50, "SM", 6, , 2, 2.5
```

```
pl.SetGraphicsContext picMain, Xo, 150, Xw, 750, SMmin, SMmax, CSng(ds), CSng(de)
```

```
pl.DrawBlockFill SMmin, SMmax, SMave(), dp(), NI
```

```
pl.DrawBlockGraph SMave(), dp(), NI, QBColor(12), 3
```

```
pl.DrawTrackFrame picMain, Xo, 150, Xw, 750, 1
```

```
Xo% = Xo + Xw + 10
```

```
Xw# = 80
```

```
pl.PutLogCode md, "YM"
```



```

pl.PutLogMin md, YMmin

pl.PutLogMax md, YMmax

pl.ReadColorSpectrum "C:\K-tron\Templates\ColorSpectrum\CLR-Surfer\WhiteBlue.clr"

pl.DrawFreeHeader picMain, Xo, 10, Xw, 130, 20, "YM", "Gpa", YMmin, YMmax, QBColor(13), 3, , , 2, 2.5

pl.DrawHeaderSpectrum picMain, Xo, 10, Xw, 130, 50, "YM", 6, , 2, 2.5

pl.SetGraphicsContext picMain, Xo, 150, Xw, 750, YMmin, YMmax, CSng(ds), CSng(de)

pl.DrawBlockFill YMmin, YMmax, YMave(), dp(), NI

pl.DrawBlockGraph YMave(), dp(), NI, QBColor(13), 3

pl.DrawTrackFrame picMain, Xo, 150, Xw, 750, 1

```

$Xo\% = Xo + Xw + 10$

$Xw\# = 80$

```
pl.PutLogCode md, "PR"
```

```
pl.PutLogMin md, PRmin
```

```
pl.PutLogMax md, PRmax
```

```
pl.ReadColorSpectrum "C:\K-tron\Templates\ColorSpectrum\CLR-Surfer\WhitePink.clr"
```

```
pl.DrawFreeHeader picMain, Xo, 10, Xw, 130, 20, "PR", "Gpa", PRmin, PRmax, QBColor(5), 3, , , 2.5
```

```
pl.DrawHeaderSpectrum picMain, Xo, 10, Xw, 130, 50, "PR", 6, , 2, 2.5
```

```
pl.SetGraphicsContext picMain, Xo, 150, Xw, 750, PRmin, PRmax, CSng(ds), CSng(de)
```

```
pl.DrawBlockFill PRmin, PRmax, PRave(), dp(), NI
```

```
pl.DrawBlockGraph PRave(), dp(), NI, QBColor(5), 3
```

```
pl.DrawTrackFrame picMain, Xo, 150, Xw, 750, 1
```

$Xo\% = Xo + Xw + 10$

$Xw\# = 80$

```
pl.PutLogCode md, "POR"
```

```
pl.PutLogMin md, Pomin
```

```
pl.PutLogMax md, POmax
```

```
pl.ReadColorSpectrum "C:\K-tron\Templates\ColorSpectrum\CLR-Surfer\WhiteOrange.clr"
```

```
pl.DrawFreeHeader picMain, Xo, 10, Xw, 130, 20, "POR", "%", Pomin, POmax, QBColor(6), 3, , , 2, 2.5
```

```

pl.DrawHeaderSpectrum picMain, Xo, 10, Xw, 130, 50, "POR", 6, , 2, 2.5

pl.SetGraphicsContext picMain, Xo, 150, Xw, 750, P0min, P0max, CSng(ds), CSng(de)

pl.DrawBlockFill P0min, P0max, PORave(), dp(), NI

pl.DrawBlockGraph PORave(), dp(), NI, QBColor(6), 3

pl.DrawTrackFrame picMain, Xo, 150, Xw, 750, 1

```

```
'-----12. Geomechanics
```

```
ReDim OBPi!(NI), OBPt!(NI), OBG!(NI), VES!(NI), PP!(NI), PPG!(NI), FG!(NI)
```

```
OBPimin! = 9999: OBPimax! = -9999
```

```
OBPtmin! = 9999: OBPtmax! = -9999
```

```
OBGmin! = 9999: OBGmax! = -9999
```

```
VESmin! = 9999: VESmax! = -9999
```

```
PPmin! = 9999: PPmax! = -9999
```

```
PPGmin! = 9999: PPGmax! = -9999
```

```
FGmin! = 9999: FGmax! = -9999
```

```
For i = 1 To NI - 1
```

```
OverburdenPressure_Density RHOave(i), dp(i) - dp(i - 1), OBPi(i)
```

```
OBPt(i) = OBPt(i - 1) + OBPi(i)
```

```
OverburdenGradient dp(i), OBPt(i), OBG(i)
```

```
Vpt! = VPave(i): If Vpt < 1550 Then Vpt = 1550 'Check Filter
```

```
'VerticalEffectiveStress_IntVelocity Vpt, VES(i)
```

```
VerticalEffectiveStress_Porosity PORave(i), VES(i)
```

```
""If VES(i) < 0 Then VES(i) = 200 'Check Filter
```

```
PorePressure OBPt(i), VES(i), PP(i)
```

```
If PP(i) < 0 Then
```

```
PP(i) = Abs(PP(i)) / 2
```

```
End If
```

```
PressureToGradient dp(i), PP(i), PPG(i)
```

FractureGradient PPG(i), OBG(i), PRave(i), FG(i)

If OBPi(i) < OBPimin Then OBPimin = OBPi(i)

If OBPi(i) > OBPimax Then OBPimax = OBPi(i)

If OBPt(i) < OBPtmin Then OBPtmin = OBPt(i)

If OBPt(i) > OBPtmax Then OBPtmax = OBPt(i)

If OBG(i) < OBGmin Then OBGmin = OBG(i)

If OBG(i) > OBGmax Then OBGmax = OBG(i)

If VES(i) < VESmin Then VESmin = VES(i)

If VES(i) > VESmax Then VESmax = VES(i)

If PP(i) < PPmin Then PPmin = PP(i)

If PP(i) > PPmax Then PPmax = PP(i)

If PPG(i) < PPGmin Then PPGmin = PPG(i)

If PPG(i) > PPGmax Then PPGmax = PPG(i)

If FG(i) < FGmin Then FGmin = FG(i)

If FG(i) > FGmax Then FGmax = FG(i)

Next

Xo% = Xo + Xw + 10 'OBP Interval

Xw# = 80

pl.PutLogCode md, "OBPi"

pl.PutLogMin md, OBPimin

pl.PutLogMax md, OBPimax

pl.ReadColorSpectrum "C:\K-tron\Templates\ColorSpectrum\CLR-Surfer\WhiteYellow.clr"

pl.DrawFreeHeader picMain, Xo, 10, Xw, 130, 20, "OBPi", "psi", OBPimin, OBPimax, QBColor(6), 3, , , 2.5

pl.DrawHeaderSpectrum picMain, Xo, 10, Xw, 130, 50, "OBPi", 6, , , 2.5

pl.SetGraphicsContext picMain, Xo, 150, Xw, 750, OBPimin, OBPimax, CSng(ds), CSng(de)

pl.DrawBlockFill OBPimin, OBPimax, OBPi(), dp(), NI

pl.DrawBlockGraph OBPi(), dp(), NI, QBColor(6), 3

pl.DrawTrackFrame picMain, Xo, 150, Xw, 750, 1

```

Xo% = Xo + Xw + 10      'OBP Total

Xw# = 95

pl.PutLogCode md, "OBPt"

pl.PutLogMin md, OBPtmin

pl.PutLogMax md, OBPtmax

pl.ReadColorSpectrum "C:\K-tron\Templates\ColorSpectrum\CLR-Surfer\ChromaDepth.clr"

pl.DrawFreeHeader picMain, Xo, 10, Xw, 130, 20, "OBP", "psi", OBPtmin, OBPtmax, QBColor(12), 3, , , 2.5

pl.DrawHeaderSpectrum picMain, Xo, 10, Xw, 130, 50, "OBP", 6, , , 2.5

pl.SetGraphicsContext picMain, Xo, 150, Xw, 750, OBPtmin, OBPtmax, CSng(ds), CSng(de)

pl.DrawBlockFill OBPtmin, OBPtmax, OBPt(), dp(), NI

pl.DrawBlockGraph OBPt(), dp(), NI, QBColor(12), 3

pl.DrawTrackFrame picMain, Xo, 150, Xw, 750, 1

```

```

Xo% = Xo + Xw + 10      'OBG

Xw# = 85

pl.PutLogCode md, "OBG"

pl.PutLogMin md, OBGmin

pl.PutLogMax md, OBGmax

pl.ReadColorSpectrum "C:\K-tron\Templates\ColorSpectrum\CLR-Surfer\FiveShades.clr"

pl.DrawFreeHeader picMain, Xo, 10, Xw, 130, 20, "OBG", "psi/ft", OBGmin, OBGmax, QBColor(1), 3, , , 2, 2.5

pl.DrawHeaderSpectrum picMain, Xo, 10, Xw, 130, 50, "OBG", 6, , 2, 2.5

pl.SetGraphicsContext picMain, Xo, 150, Xw, 750, OBGmin, OBGmax, CSng(ds), CSng(de)

pl.DrawBlockFill OBGmin, OBGmax, OBG(), dp(), NI

pl.DrawBlockGraph OBG(), dp(), NI, QBColor(1), 3

pl.DrawTrackFrame picMain, Xo, 150, Xw, 750, 1

```

```

Xo% = Xo + Xw + 10      'VES

Xw# = 95

pl.PutLogCode md, "VES"

```

```

pl.PutLogMin md, VESmin

pl.PutLogMin md, Abs(VESmin) 'Check Filter Adjustment: Abs()

pl.ReadColorSpectrum "C:\K-tron\Templates\ColorSpectrum\CLR-Surfer\FiveShades.clr"

pl.DrawFreeHeader picMain, Xo, 10, Xw, 130, 20, "VES", "psi", Abs(VESmin), VESmax, QBColor(1), 3, , , 2.4

pl.DrawHeaderSpectrum picMain, Xo, 10, Xw, 130, 50, "VES", 6, , , 2.4

pl.SetGraphicsContext picMain, Xo, 150, Xw, 750, VESmin, VESmax, CSng(ds), CSng(de)

pl.PutLogMin md, VESmin 'Check Filter Adjustment

pl.DrawBlockFill VESmin, VESmax, VES(), dp(), NI

pl.DrawBlockGraph VES(), dp(), NI, QBColor(1), 3

pl.DrawTrackFrame picMain, Xo, 150, Xw, 750, 1

```

```
Xo% = Xo + Xw + 10      'PP
```

```
Xw# = 85
```

```
pl.PutLogCode md, "PP"
```

```
pl.PutLogMin md, PPmin
```

```
pl.PutLogMax md, PPmax
```

```
pl.ReadColorSpectrum "C:\K-tron\Templates\ColorSpectrum\CLR-Surfer\FiveShades.clr"
```

```
pl.DrawFreeHeader picMain, Xo, 10, Xw, 130, 20, "PP", "psi", PPmin, PPmax, QBColor(1), 3, , , 2.4
```

```
pl.DrawHeaderSpectrum picMain, Xo, 10, Xw, 130, 50, "PP", 6, , , 2.4
```

```
pl.SetGraphicsContext picMain, Xo, 150, Xw, 750, PPmin, PPmax, CSng(ds), CSng(de)
```

```
pl.DrawBlockFill PPmin, PPmax, PP(), dp(), NI
```

```
pl.DrawBlockGraph PP(), dp(), NI, QBColor(1), 3
```

```
pl.DrawTrackFrame picMain, Xo, 150, Xw, 750, 1
```

```
Xo% = Xo + Xw + 10      'PPG
```

```
Xw# = 85
```

```
pl.PutLogCode md, "PPG"
```

```
pl.PutLogMin md, PPGmin
```

```
pl.PutLogMax md, PPGmax
```

```
pl.ReadColorSpectrum "C:\K-tron\Templates\ColorSpectrum\CLR-Surfer\FiveShades.clr"
```

```

pl.DrawFreeHeader picMain, Xo, 10, Xw, 130, 20, "PPG", "psi", PPGmin, PPGmax, QBColor(1), 3, , 2, 2.4
pl.DrawHeaderSpectrum picMain, Xo, 10, Xw, 130, 50, "PPG", 6, , 2, 2.4
pl.SetGraphicsContext picMain, Xo, 150, Xw, 750, PPGmin, PPGmax, CSng(ds), CSng(de)
pl.DrawBlockFill PPGmin, PPGmax, PPG(), dp(), NI
pl.DrawBlockGraph PPG(), dp(), NI, QBColor(1), 3
pl.DrawTrackFrame picMain, Xo, 150, Xw, 750, 1

```

```
Xo% = Xo + Xw + 10      'FG
```

```
Xw# = 85
```

```
pl.PutLogCode md, "FG"
```

```
pl.PutLogMin md, FGmin
```

```
pl.PutLogMax md, FGmax
```

```
pl.ReadColorSpectrum "C:\K-tron\Templates\ColorSpectrum\CLR-Surfer\FiveShades.clr"
```

```
pl.DrawFreeHeader picMain, Xo, 10, Xw, 130, 20, "FG", "psi", FGmin, FGmax, QBColor(1), 3, , 2, 2.4
```

```
pl.DrawHeaderSpectrum picMain, Xo, 10, Xw, 130, 50, "FG", 6, , 2, 2.4
```

```
pl.SetGraphicsContext picMain, Xo, 150, Xw, 750, FGmin, FGmax, CSng(ds), CSng(de)
```

```
pl.DrawBlockFill FGmin, FGmax, FG(), dp(), NI
```

```
pl.DrawBlockGraph FG(), dp(), NI, QBColor(1), 3
```

```
pl.DrawTrackFrame picMain, Xo, 150, Xw, 750, 1
```